uOttawa

L'Université canadienne
Canada's university

FACULTÉ DES ÉTUDES SUPÉRIEURES ET POSTOCTORALES

uOttawa

L'Université canadienne
Canada's university

FACULTY OF GRADUATE AND POSDOCTORAL STUDIES

Steven Wickson
AUTEUR DE LA THÈSE / AUTHOR OF THESIS

M.Sc. (Earth Sciences)
GRADE / DEGREE

Department of Earth Sciences
FACULTÉ, ÉCOLE, DÉPARTEMENT / FACULTY, SCHOOL, DEPARTMENT

High-Resolution Carbon Isotope Stratigraphy of the Ordovician-Silurian Boundary on Anticosti Island, Quebec: Regional and Global Implications

TITRE DE LA THÈSE / TITLE OF THESIS

A. Desrochers
DIRECTEUR (DIRECTRICE) DE LA THÈSE / THESIS SUPERVISOR

J. Veizer
CO-DIRECTEUR (CO-DIRECTRICE) DE LA THÈSE / THESIS CO-SUPERVISOR

I. Clark

G. Dix

Gary W. Slater
Le Doyen de la Faculté des études supérieures et postdoctorales / Dean of the Faculty of Graduate and Postdoctoral Studies

High-Resolution Carbon Isotope Stratigraphy of the Ordovician-Silurian Boundary on Anticosti Island, Quebec: Regional and Global Implications

Steven Wickson

Thesis submitted to the
Faculty of Graduate and Postdoctoral Studies
University of Ottawa
In partial fulfillment of the requirements for the
M.Sc. degree in the Earth Sciences

Ottawa-Carleton Geoscience Center
and
University of Ottawa
Ottawa, Canada

Your file Votre référence
ISBN: 978-0-494-79701-3
Our file Notre référence
ISBN: 978-0-494-79701-3

Abstract

The end-Ordovician was a critical time in Earth history and marked the occurrence of a mass extinction and a period of continental glaciation. The Ellis Bay Formation on Anticosti Island in Quebec represents up to 100 meters of relatively undisturbed, continuous, low latitude, shallow water carbonate ramp deposits that span the Hirnantian Stage and terminate close to the Ordovician-Silurian (O-S) boundary. In this study, approximately 400 samples of micritic limestones were collected from six Ellis Bay sections ranging from the basin margin to more distal basin center of the Anticosti Basin. $\delta^{13}C$ and $\delta^{18}O$ isotopic ratios were measured from these samples and integrated within a recently proposed framework of sequence stratigraphy and biostratigraphy for the Ellis Bay Formation. The measured $\delta^{13}C$ values in most sections show a positive excursion (~2‰) in the lower Ellis Bay Formation followed by a larger excursion (~4‰) in the upper Ellis Bay Formation. The $\delta^{13}C$ profile of the Ellis Bay Formation on Anticosti Island exhibits a pattern similar to those of other profiles in graptolite-rich Hirnantian basinal successions from the rest of the world. The $\delta^{13}C$ record on Anticosti Island is not consistent with predictions and observations based on current models that describe the state and evolution of the global carbon cycle during the Late Ordovician.

Résumé

La fin de l'Ordovicien est une période critique de l'histoire de la Terre marquée par les extinctions massives et la glaciation. La Formation d'Ellis Bay, sur l'île d'Anticosti (Québec), fait partie de la plate-forme carbonatée d'une ancienne mer tropicale peu profonde. Elle présente plus de 100 mètres de dépôts ininterrompus et quasi intacts couvrant l'étage de l'Hirnantien jusqu'à la limite Ordovicien-Silurien. Dans le cadre de la présente étude, environ 400 échantillons de calcaire micritique ont été prélevés dans six sections différentes du Bassin d'Anticosti, de la marge proximale au basin plus distal. Les rapports isotopiques $\delta^{13}C$ et $\delta^{18}O$ ont été mesurés à partir de ces échantillons et intégrés à un cadre de stratigraphie séquentielle et de biostratigraphie de la Formation d'Ellis Bay récemment proposé. Les mesures du $\delta^{13}C$ dans la majorité des sections montrent une excursion positive (~2 ‰) dans l'Ellis Bay inférieur, suivie d'une excursion plus importante (~4 ‰) dans l'Ellis Bay supérieur. La tendance qui se dégage du profil $\delta^{13}C$ de la Formation d'Ellis Bay de l'île d'Anticosti est semblable à celle d'autres séries riches en graptolites des bassins d'âge Hirnantien ailleurs dans le monde. L'analyse stratigraphique du $\delta^{13}C$ sur l'île d'Anticosti montre un écart entre les observations et ce que prédisent les modèles actuels décrivant l'état et l'évolution du cycle global du carbone à l'Ordovicien Supérieur.

Acknowledgments

This project could not have taken place without the support of two Discovery grants for André Desrochers and Jan Veizer from the Natural Sciences and Engineering Research Council (NSERC). SEPAQ Anticosti and the Ministère des Resources Naturelles, de la Faune et des Parcs du Quebec (MRNFP) provided logistical support for this study. This project is also indebted to Claude Farley for his assistance with fieldwork on Anticosti Island. Many thanks as well to staff of the G.G. Hatch Stable Isotope Laboratory at the University of Ottawa, George Mrazek for his help with sample preparation and Pierre Bertrand for drafting many of the figures in this thesis.

Table of Contents

List of Figures

Introduction

This research project concerns the development of a high-resolution carbon isotope stratigraphic framework for the Ellis Bay Succession on Anticosti Island. The Ellis Bay Succession contains the entire Ellis Bay Formation along with the uppermost part of the Vaureal Formation and the basal part of the Becscie Formation. This succession is important because it comprises strata spanning the Ordovician-Silurian (O-S) boundary, a critical time interval in the history of life on our planet, which involved a mass extinction event at a time that large ice sheets developed on Gondwana [1,2]. The Ellis Bay Succession is one of the most complete, undeformed and diagenetically unaltered sections at the O-S boundary in the world, making it an ideal location for using geochemical proxies to decipher Earth system changes at the end of the Ordovician.

Recent research conducted on the Ellis Bay Formation includes studies of sequence stratigraphy by Desrochers et al. [3] and high-resolution chitinozoan biostratigraphy by Achab et al. [4]. While carbon isotope profiles for the O-S boundary have been produced in other studies [5,6,7,8], the present study aims to produce a new set of data with increased resolution and better constraints on timing. This project may be useful for interpreting some of the key events that occurred near the O-S boundary, and establishing a timeline of events for the end Ordovician interval by integrating chemostratigraphic isotope data within a framework of well-constrained sequence stratigraphy and biostratigraphy.

For this study, earlier sedimentological and geochemical work on Anticosti Island was complimented by the resampling of six sections in August of 2009. Together, these sections comprise sediments that accumulated on a storm-dominated carbonate-siliciclastic ramp within the Anticosti Basin ranging from proximal inner ramp (east) to more distal outer ramp (west). Each of these sections spans the O-S boundary and maps the carbon isotope evolution of the basin in space and time. More attention was given to the sediments on the western side of the island as they contain more complete successions.

The series of events that occurred at the end of the Ordovician period are often assumed to have been synchronous and causative [9,10]. For instance, it is proposed that glaciation induced a sea level drop, and the sea level drop and global cooling induced a mass extinction. Atmospheric pCO_2 is sometimes invoked to complete the story by providing an explanation for the cause of the Hirnantian glaciation [9,10,11]. Although there is nothing fundamentally wrong with this reasoning for the series of events at the O-S boundary, this study will test if increased resolution of geochemical proxies and improved constraints on timing can support these basic assumptions.

Timeline of Events

In this section, we review information regarding Ordovician palaeogeography and the timing of events in the Hirnantian leading up to the O-S boundary. The Hirnantian was the final stage of the Ordovician period, and the majority of the sediments studied in this project were deposited within this timeframe. The duration of the Hirnantian is estimated to be approximately 1.9 million years [4]. It was preceded by the Katian stage and the Katian-Hirnantian boundary lies close to the Vaureal-Ellis Bay boundary on Anticosti Island. The Hirnantian stage is named after the succession exposed at Cwm

Hirnant in northern Wales and has been defined by a distinct brachiopod fauna that includes the species *Hirnantia*, *Hindella* and *Eospirigerina* [12]. The Hirnantian stands out amongst other stages in the Ordovician and Silurian for a few reasons. Firstly it is thought to represent one of only three times in the Phanerozoic Eon when large continental ice sheets existed on our planet. This is based on direct evidence of glacial sediments in Gondwana and indirectly by evidence for a eustatic drop close to 100 meters [13] during the early Hirnantian. Another thing that makes the Hirnantian interesting is that it was a period of significant faunal turnover. In particular it included a mass extinction event that altered marine faunas on a worldwide scale, and is regarded as the second largest extinction event of the Phanerozoic eon in terms of biodiversity loss [14]. Finally, the Hirnantian has attracted interest more recently as it is marked by a dramatic increase of the $^{13}C/^{12}C$ ratio in ocean environments, which is the main subject of this thesis. An overview of the timing of events in the Hirnantian is provided in Figure 1. Here we see that a major glaciation, marine regression, faunal extinction and carbon isotope excursion occurred within the same biostratigraphic timeframe.

Paleogeographical and paleoclimatic evidence suggests that high sea levels [15] and moderate global temperatures [16] characterized the pre-Hirnantian Ordovician world. Ordovician life was mainly restricted to shallow marine environments, although primitive plants such as bryophytes are believed to have emerged by the end of the period [17]. Biodiversity of marine organisms increased dramatically during the Ordovician period in what is known as the Great Ordovician Biodiversification Event [18]. At this time, the Gondwana supercontinent existed in high southern latitudes (Figure 2), while three more modest paleocontinents existed in the tropics: Laurentia,

Figure 1. An overview of the events at the O-S Boundary. Modified from Brenchley et al. [19].

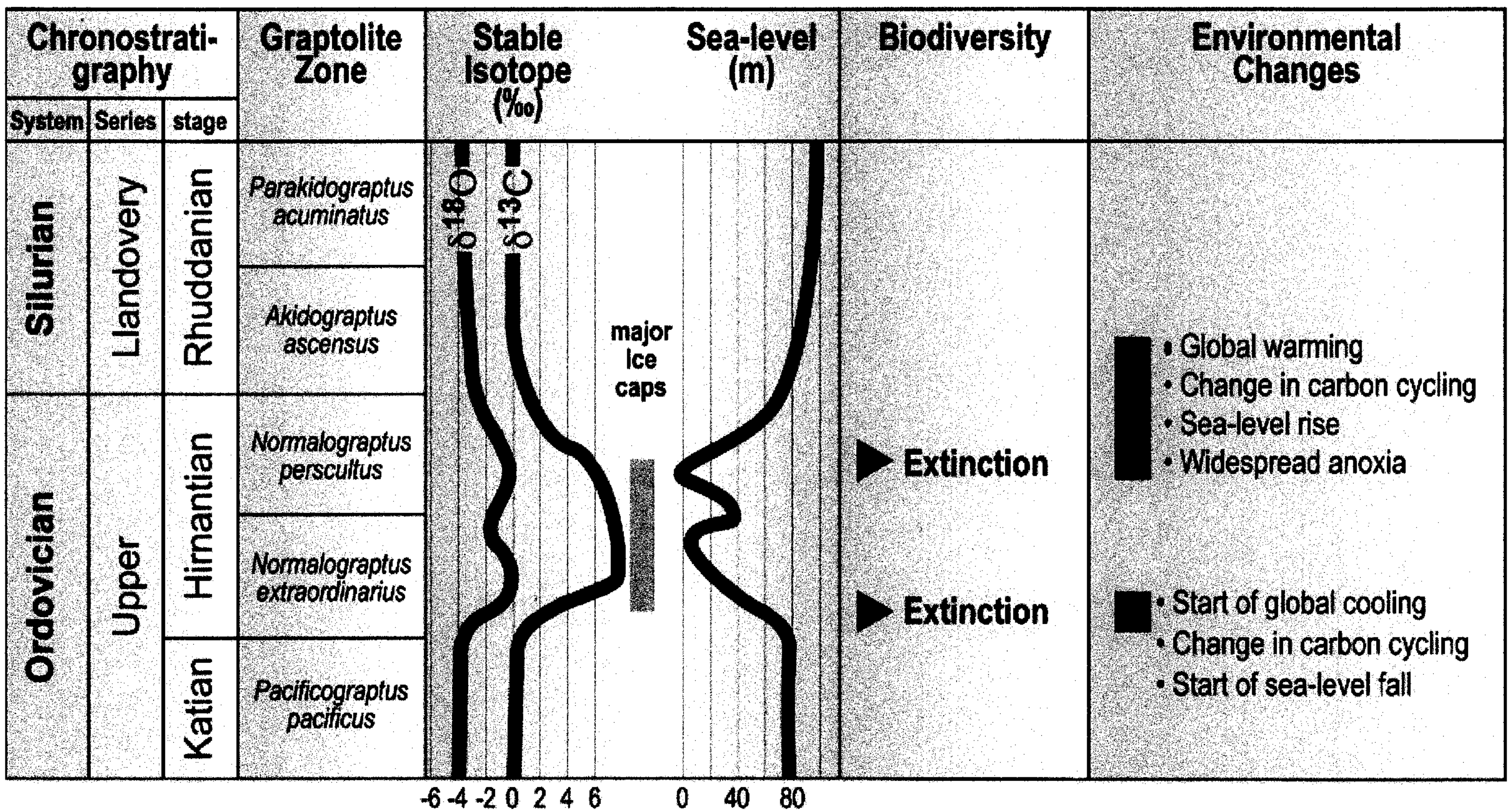

Chronostratigraphy
System
Series
stage
Graptolite Zone
Stable Isotope (‰)
Sea-level (m)
Biodiversity
Environmental Changes
Silurian
Llandovery
Rhuddanian
Ordovician
Upper
Hirnantian
Katian
Parakidograptus acuminatus
Akidograptus ascensus
Normalograptus persculptus
Normalograptus extraordinarius
Pacificograptus pacificus
δ18O
δ13C
major Ice caps
-6 -4 -2 0 2 4 6
0 40 80
Extinction
Extinction
• Global warming
• Change in carbon cycling
• Sea-level rise
• Widespread anoxia
• Start of global cooling
• Change in carbon cycling
• Start of sea-level fall

Figure 2. Late Ordovician Paleogeography. Modified from Achab & Paris, 2007 [20] and McLaughlin & Brett, 2007 [21]. Anticosti Island is marked in red on the eastern side of Laurentia.

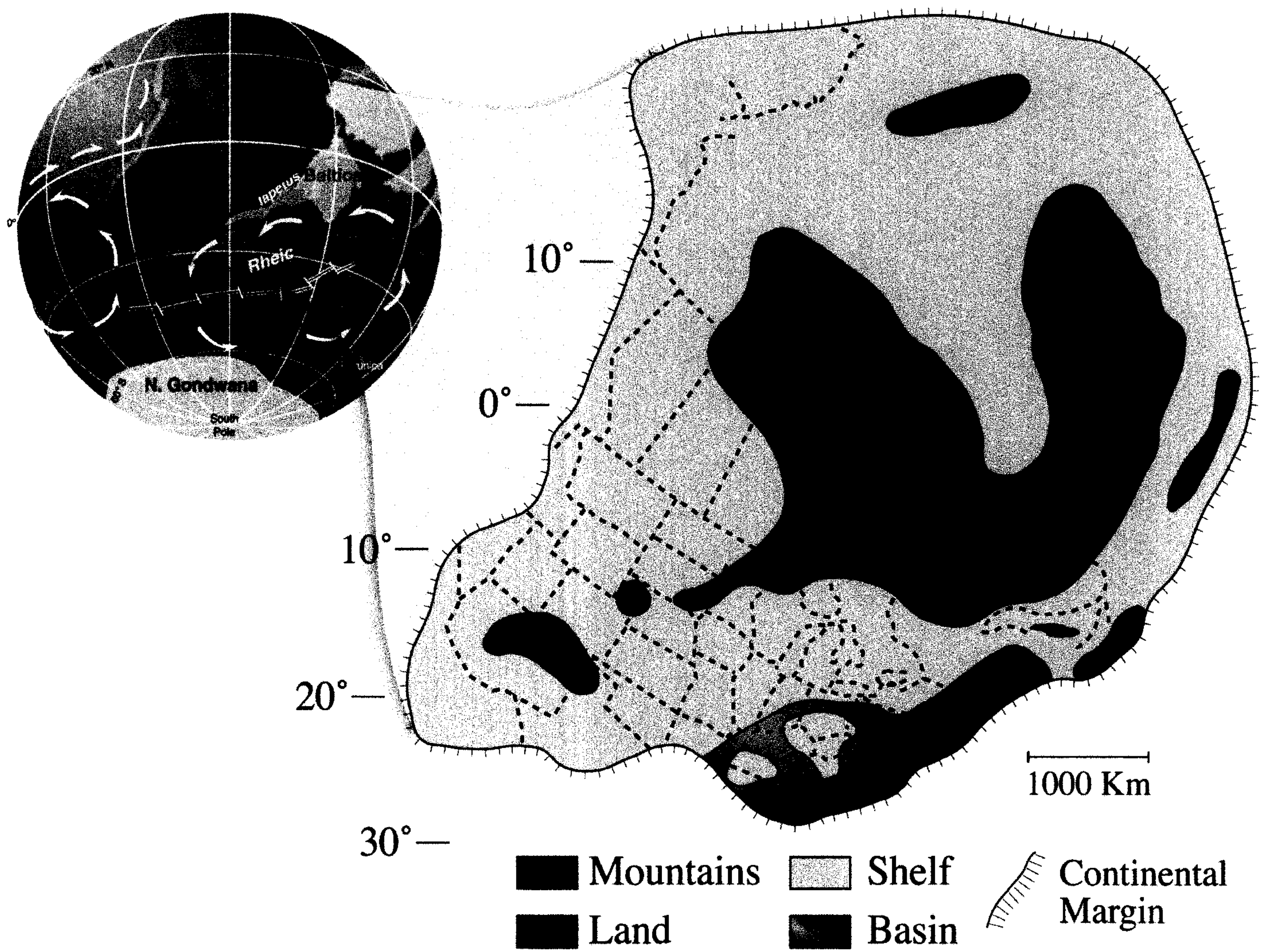
Iapetus
Baltica
Rheic
N. Gondwana
South
Pole
10°
0°
10°
20°
30°
1000 Km
Mountains
Land
Shelf
Basin
Continental
Margin

Baltica and Siberia, which were separated from Gondwana by the Rheic Ocean. The Late Ordovician sea level highstand meant that most of the paleocontinents were flooded with epeiric seas. The interior of eastern North America was submerged from Texas to southern Quebec, and only a fraction of the continent remained above sea level. Beginning in the mid-Ordovician, Laurentia collided with the edge of an ocean plate, initiating the Taconic Orogeny [22]. This led to tectonic subsidence on what is now the eastern seaboard of the United States and Canada, creating an active foreland basin. This foreland basin, in which Anticosti Island existed, was a southerly dipping tropical shallow water carbonate ramp [4]. Near the end of the Ordovician, at approximately the onset of the Hirnantian, a large continental glaciation developed on southern Gondwana [23]. This glaciation, in turn, precipitated a major worldwide regression that lowered sea level worldwide and caused the vast majority of epeiric seas to be drained. The intensity of the Hirnantian continental glaciation was brief in geological terms as by the start of the Silurian, the former epeiric seas were restored [24].

Hirnantian Glaciation

Glacial deposits such as tillite have been observed in Upper Ordovician and Lower Silurian strata of Africa and South America since the 1950s [25]. Tillite has also been found in Hirnantian formations in Arabia and elsewhere, as illustrated in Figure 3. The Ordovician glaciation is believed to have commenced on parts of Gondwana as early as the Caradoc and lasted at least until the late Llandovery in the Silurian period, a total duration of approximately 35 million years [26]. While during most of this time the Gondwana glaciation was relatively minor, it covered a much larger area during the

Figure 3. Maximum extent of the end Ordovician Glaciation [2].

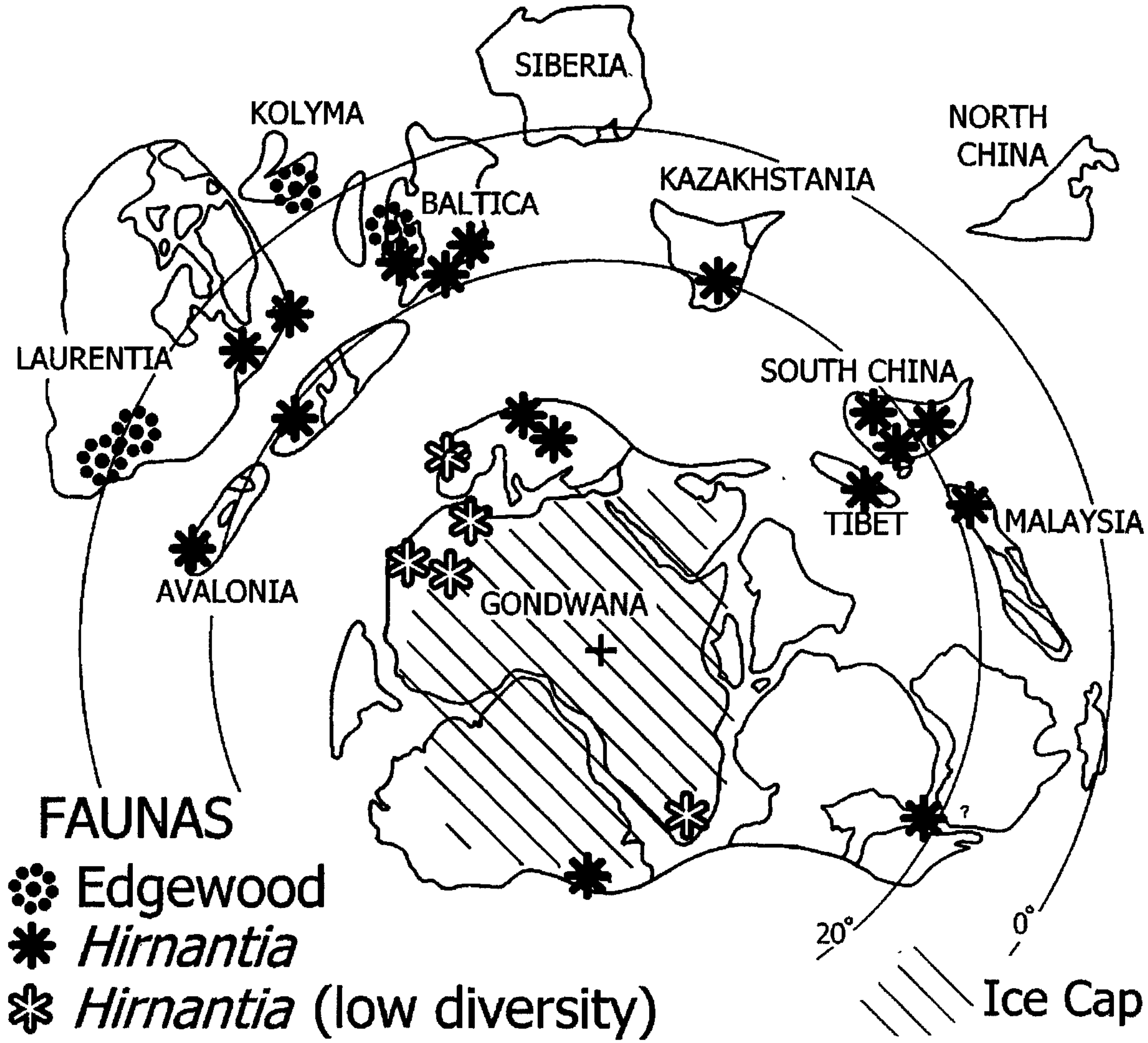
SIBERIA
KOLYMA
NORTH
CHINA
BALTICA
KAZAKHSTANIA
LAURENTIA
SOUTH CHINA
TIBET
MALAYSIA
AVALONIA
GONDWANA
FAUNAS
Edgewood
Hirnantia
Hirnantia (low diversity)
20°
0°
Ice Cap

Hirnantian. The Gondwana ice sheet at its peak in the Hirnantian is believed to have been comparable to the ice volume locked up in North American ice sheets during the most recent Wisconsin Glaciation [3,27]. The Ordovician glaciation is also thought to have been responsible for the migration of the Hirnantian cool water fauna northward, where it established a biozone in equatorial regions. Another fossil group, known as the Edgewood fauna, represents an assortment of corals that survived in a band of warmer water around the tropics at the peak of the Hirnantian glaciation [2]. The Hirnantian ended with a phase of rapid warming that led to the demise of the major continental ice sheets, and of the Hirnantian fauna. Small remnants of the Gondwana ice sheet however, lasted well into the Silurian period [26].

Sea Level Change

Evidence for past sea level change is derived from the analysis of sedimentary facies from different locations around the world. Although eustatic changes are defined as being global in extent, local changes in sea level can be distinguished from examination of localized facies. A number of different factors can affect sea level on a regional scale including tectonic uplift and the development of glaciers. For an overview of the sea level history of the Late Ordovician period, a recently published sea level curve for the early Palaeozoic is provided in Figure 4. Global sea level was high for most of the Ordovician. This global highstand in sea level was followed in the final stages of the Ordovician by a eustatic drop of approximately 100 meters [2]. This regression began in the early Hirnantian and terminated in the later Hirnantian, and occurred in two pulses of glacially induced sea level lowstands. The second pulse appears to have been more

Figure 4. Sea Level Curve for the early Palaeozoic Era [13].

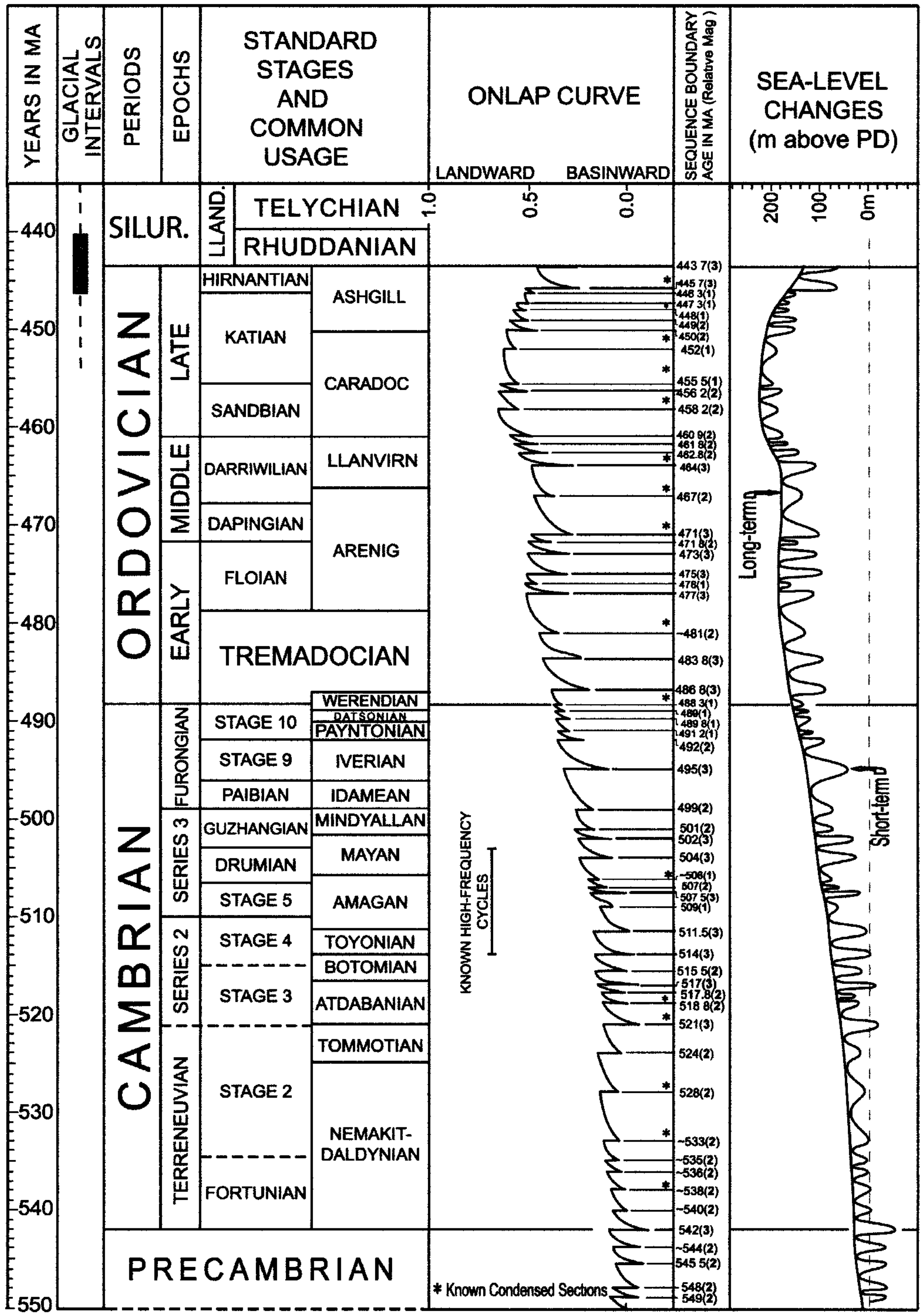
YEARS IN MA
GLACIAL INTERVALS
PERIODS
EPOCHS
STANDARD STAGES AND COMMON USAGE
ONLAP CURVE
LANDWARD
BASINWARD
SEQUENCE BOUNDARY AGE IN MA (Relative Mag.)
SEA-LEVEL CHANGES (m above PD)
SILUR.
LLAND.
TELYCHIAN
RHUDDANIAN
ORDOVICIAN
LATE
MIDDLE
EARLY
HIRNANTIAN
KATIAN
SANDBIAN
DARRIWILIAN
DAPINGIAN
FLOIAN
TREMADOCIAN
ASHGILL
CARADOC
LLANVIRN
ARENIG
CAMBRIAN
FURONGIAN
SERIES 3
SERIES 2
TERRENEUVIAN
STAGE 10
STAGE 9
PAIBIAN
GUZHANGIAN
DRUMIAN
STAGE 5
STAGE 4
STAGE 3
STAGE 2
FORTUNIAN
WERENDIAN
DATSONIAN
PAYNTONIAN
IVERIAN
IDAMEAN
MINDYALLAN
MAYAN
AMAGAN
TOYONIAN
BOTOMIAN
ATDABANIAN
TOMMOTIAN
NEMAKIT-DALDYNIAN
PRECAMBRIAN
KNOWN HIGH-FREQUENCY CYCLES
* Known Condensed Sections
Long-term
Short-term
1.0
0.5
0.0
200
100
0m
440
450
460
470
480
490
500
510
520
530
540
550
443.7(3)
445.7(3)
446.3(1)
447.3(1)
448(1)
449(2)
450(2)
452(1)
455.5(1)
456.2(2)
458.2(2)
460.9(2)
461.8(2)
462.8(2)
464(3)
467(2)
471(3)
471.8(2)
473(3)
475(3)
476(1)
477(3)
~481(2)
483.8(3)
486.8(3)
488.3(1)
489(1)
489.8(1)
491.2(1)
492(2)
495(3)
499(2)
501(2)
502(3)
504(3)
~506(1)
507(2)
507.5(3)
509(1)
511.5(3)
514(3)
515.5(2)
517(3)
517.8(2)
518.8(2)
521(3)
524(2)
528(2)
~533(2)
~535(2)
~536(2)
~538(2)
~540(2)
542(3)
~544(2)
545.5(2)
548(2)
549(2)

extensive according to analysis of facies for the periglacial sediments of Morocco [28]. The two lowstands were separated by a brief mid-Hirnantian highstand where sea level rose substantially and was restored to approximately 40 meters above the minimum achieved during the regression (Figure 1). A post-glacial transgression, initiated in the later part of the Hirnantian, returned the sea level to its pre-Hirnantian state by the start of the Silurian period. The end-Ordovician regression is observed on a global scale, and it has been directly linked with the development of a continental ice sheet on Gondwana [29].

End Ordovician Extinction

Two pulses of significant faunal turnover among marine communities were associated with the Hirnantian (Figure 1). Associated with the first pulse, appears to have been a reduction in marine diversity, particularly among graptolites and other pelagic organisms at the termination of the Katian stage. Some faunal groups recovered in the early Hirnantian, and some such as the cool water Hirnantia fauna flourished [2]. This brief recovery was followed later in the Hirnantian by a second faunal turnover. The terminal Ordovician extinction, as it is often called, affected all marine groups and it is estimated that approximately 85% of marine animal species perished around the O-S boundary [14]. The mass extinction was concentrated amongst fauna residing in epicontinental seas [2]. These extinctions are often linked to the Hirnantian glaciation and its associated regression and drainage of epeiric seas, with the first extinction resulting from the glaciation and sea level fall, and the second extinction being the result of subsequent deglaciation and abrupt climate change.

$\delta^{13}C$ and $\delta^{18}O$ changes

Isotopic proxies are relatively new to studies of the O-S boundary. One of the first studies that focused on the O-S boundary was produced in 1993 by Long [30]. In 2001, Brenchley et al. [5] performed a study of carbon and oxygen isotopes on some 400 brachiopod and bulk carbonate samples and produced a curve similar to that shown in Figure 1. Here, $\delta^{13}C$ exhibits a peak around a value of 7 ‰ midway though the *Normalograptus extraordinarius* graptolite biozone, followed by a slow return to the pre-Hirnantian background of approximately 0 ‰. On the other hand, $\delta^{18}O$ measurements exhibit a double crested shape that mirrors the changes in sea level during the Hirnantian. $\delta^{18}O$ peaks in the middle of the *N. extraordinarius* zone, as well as in the middle of the *N. persculptus* zone at a value of 0 ‰. The two peaks are separated by a trough that is coincident with the mid-Hirnantian highstand. Of particular note in this diagram is that the initial increase and final decrease of $\delta^{18}O$ and $\delta^{13}C$ coincide. Brenchley et al. suggested that $\delta^{18}O$ rose in response to the Hirnantian glaciation and $\delta^{13}C$ rose as a result of increased organic carbon burial and that the two records are more or less synchronous [5]. Many more recent isotope studies for the O-S boundary, however, do not display this apparent synchronicity between $\delta^{13}C$ and $\delta^{18}O$ records [6,10,11,31].

Review of Biostratigraphy

The following pages will present an overview of the biostratigraphy for the O-S boundary. It will review the present framework for the O-S boundary concerning the key index fossil groups: brachiopods, conodonts, graptolites, chitinozoans and acritarchs.

Refer to Figure 5 for a summary of the biostratigraphy for the Vaureal, Ellis Bay and lower Becscie formations on Anticosti Island.

Brachiopods

The Hirnantian stage is defined loosely by the occurrence of an assortment of brachiopods known as the Hirnantian fauna [32]. This group of fossils is found in Hirnantian strata of Laurentia, but is apparently absent in underlying Katian strata as well as Early Silurian strata in low paleolatitude sections, making it a good macrofossil for recognizing the Hirnantian stage. However, this fauna is now believed to have been diachronous, due to its apparent migration into lower latitudes during the Hirnantian glaciation, and hence may not be an ideal tool for biostratigraphy [33]. Brachiopods are also very dependent on facies, making it difficult to distinguish between global biozone changes and changes in the local marine environment. Some key elements of the Hirnantian fauna including *Hindella* and *Eospirigerina* are present in the lowermost Ellis Bay Formation at the west end of Anticosti Island [12,34], but their biostratigraphic use has been challenged [35].

On Anticosti Island, the Becscie Formation overlies the Ellis Bay Formation and represents a significant portion of the Rhuddanian, the earliest stage of the Silurian. In contrast to the Hirnantian, the basal Becscie contains a distinct assortment of dwarf brachiopods [36]. This *Lilliput* effect on brachiopods is interpreted to represent a recovery fauna immediately following the end Ordovician mass extinction.

Figure 5. Chitinozoan, graptolite and conodont biozonations of the upper Vaureal, Ellis Bay and lower Becscie formations [4].

		Units Petryk 1979, 1981	Chitinozoans Soufiane & Achab, 2000		Graptolites Riva, 1988 & Achab, 2010	Graptolites Melchin, 2008	Conodonts McCracken & Barnes, 1981
Rhud.	Rhud.	Becscie Fm.		*P. nodifera* *A. ellisbayensis*	*N. angustus*	*N. acceptus*	*I. deflecta*
Hirnantian	Gamachian	Ellis Bay Formation 7	***B. gamachiana***		*N. angustus* *R. abbreviatus*	*N. cf. parvulus* *N. abbreviatus*	*O. ? nathani*
		6		*S. taugourdeaui* *B. micracantha*			
		5			*N. angustus*	*N. minor*	*(G. ensifer)* = Fauna 13
		4					
		3					
		2		*A. longispina*			
		1					
Katian	Richmondian	Vauréal Formation 5	***H. crickmayi***	*B. concava*			
		4					
		3		*H. normalis*	*A. prominens* *(D. anceps)*		*(A. ordovicicus)* = Fauna 12
		2		*T. anticostiensis* *C. vaurealensis*	*D. complanatus*		

Conodonts

Conodonts are commonly used for Palaeozoic biostratigraphy, and have been studied and catalogued for the Upper Ordovician and Lower Silurian on Anticosti Island [37]. Unfortunately, they have limited use for the current study as they are generally long-ranging taxa and have significant intercontinental speciation. This limits their effectiveness as correlative tools on a global scale. On Anticosti Island, conodont fauna 13 is assigned to mark the Ellis Bay Formation (Figure 5). It is sandwiched between conodont fauna 12, which lies below, and the *Oulodus nathani* zone, which lies above. However, the *O. nathani* zone occurs in the uppermost Ellis Bay Formation. The stratigraphic transition between conodont fauna 13 and *O. nathani* therefore also lies below the upper boundary of the Ellis Bay Formation, and does not coincide with its boundaries defined by the graptolites and chitinozoans.

Graptolites

Traditionally, the most favourable index fossils for Ordovician strata are the graptolites. They were mostly planktonic and global in extent, common in deep water facies, and exhibited rapid evolution and morphological differentiation in the Ordovician. The Hirnantian stage is more or less equated with the *Normalograptus* biozone [4]. It is then split into two smaller subzones: *N. extraordinarius* for the early Hirnantian, and *N. persculptus* for the late Hirnantian (Figure 5). Graptolite biostratigraphy for the Hirnantian was initially based on the Global Boundary Stratotype Section and Point (GSSP) for the Ordovician-Silurian boundary, Dob's Linn, but later formalized in a Chinese section in 2006 [38]. Graptolites are not common in our study area as it represents a shallow water carbonate ramp and the vast majority of fossils are benthic. Rare graptolites have been discovered in the upper Ellis Bay Formation, but are difficult to identify due to their poor preservation [4,39]. There are no graptolites found in the lowermost section of the Ellis Bay Formation, making it impossible to determine accurately where the base of the Hirnantian is and where the division between the *N. extraordinarius* and *N. persculptus* biozones lies. These limitations seriously compromise the effectiveness of graptolite biostratigraphy on Anticosti Island.

Chitinozoans

Another group that has been used recently in Ordovician biostratigraphy are the chitinozoans. Unlike graptolites, chitinozoans are found in the shallow water facies of Anticosti Island as well as many other paleotropical O-S boundary sections in Scotland, China, Nevada, Estonia and the periglacial sections in Morocco. Chitinozoans are more abundant in the Anticosti succession sediments and provide a finer biostratigraphic resolution, especially when graptolites are rare or absent [4]. On Anticosti Island, the Ellis Bay Formation is broadly coincident with the species *Belonechitina gamachiana*, and divided into three subgroups defined by the species *Ancyrochitina longispina*, *Belonechitina micracantha* and *Spinachitina taugourdeaui* (Figure 5). *B. gamachiana* is a distinct biozone found in the upper part of the *N. extraordinarius* graptolite zone at the Vinini creek site in Nevada [40], which allows correlation between the two sites. There is a key marker unit at the top of the Ellis Bay succession called the Laframboise Member, where chitinozoans are completely absent. Above the Ellis Bay, in the lower Becscie Formation, a new chitinozoan zone, *Ancyrochitina ellisbayensis*, is present.

A. ellisbayensis is first observed approximately one meter above the base of the Becscie on the western side of Anticosti Island and approximately seven meters above the basal Becscie strata on the eastern side. *A. ellisbayensis* is also present at the GSSP for the base of the Silurian at Dob's Linn, coincident with the O-S boundary. Due to their pelagic nature, cosmopolitan distribution and their presence in both shallow water carbonate and deep water shale facies, chitinozoans are quite useful in establishing high-resolution global and regional stratigraphic correlations between different sites around the world. Most of the recent research aimed at improving the temporal resolution of the O-S boundary on Anticosti Island uses chitinozoan biostratigraphy [4].

Acritarchs

Acritarchs are organic remains of ancient phytoplankton, and are being utilized in some new biostratigraphic studies of Ordovician and Silurian strata [41]. They have great potential to be extremely useful due to the large amount of material available and the rapid speciation and morphological changes observed in their fossil record. Acritarchs are observed to have undergone at least two major turnovers in the Hirnantian strata on Anticosti Island. With the arrival of the first glacial pulse at the beginning of the Hirnantian stage, a turnover defined by a number of extinctions, speciations and morphological changes is exhibited amongst the phytoplankton. Acritarchs are rare in the later Hirnantian strata and undergo a major taxonomic decrease in the upper part of the Ellis Bay Formation. In fact, very few acritarchs are observed in the Laframboise Member, and are of extremely low diversity. Acritarch abundance and diversity increases slightly above the base of the Becscie Formation. Across this boundary a major morphological change toward larger size is observed in one of the dominant species, *Evittia remota.* Although acritarch biostratigraphy has only recently been developed on Anticosti Island, it is expected to be extremely useful for Ordovician and Silurian biostratigraphy in the future.

The Anticosti Basin

Anticosti Island is 222 kilometers long and is located in the Gulf of St. Lawrence (Figure 6). It contains some of the most complete and unaltered strata in the world for the time interval ranging from the Upper Ordovician to the Lower Silurian. There are seven distinct formations on Anticosti Island (Figure 6). The older strata are located at the northern side of the island and the strata become increasingly younger as one moves south. The eastern side of Anticosti contains sediments indicative of a proximal nearshore environment that existed on the edge of a foreland basin. As one moves toward the western side, the sediments indicate an environment of progressively increasing water depth, terminating with more distal basinal facies at the west end of the island [3].

The Ellis Bay Formation is denoted as the grey unit in Figure 6. The formation comprises five members (*sensu* Copper [12]) altogether representing about 90 meters of strata on the western side [4]. It is composed of an alternating sequence of resistant calcarenite beds and more recessive argillaceous layers, forming a series of five transgressive-regressive packages (Figure 7). The uppermost Ellis Bay Formation on the west end is made up of the Laframboise Member (TR-5 in Figure 7), which contains shallow water facies and an assortment of corals and microbialites. The Laframboise

Figure 6. A Geological Map of Anticosti Island and locations studied [42].

Section 1A – Baie St. Claire – Laframboise (West End) coastal section

Section 1B – Ellis Bay coastal section

Section 2 – NACP Drillcore

Section 3 – Vaureal River and Canyon river section

Section 4 – Natiscotec River section

Section 5 – Salmon River section

Section 6 – Lousy Cove (East End) coastal section

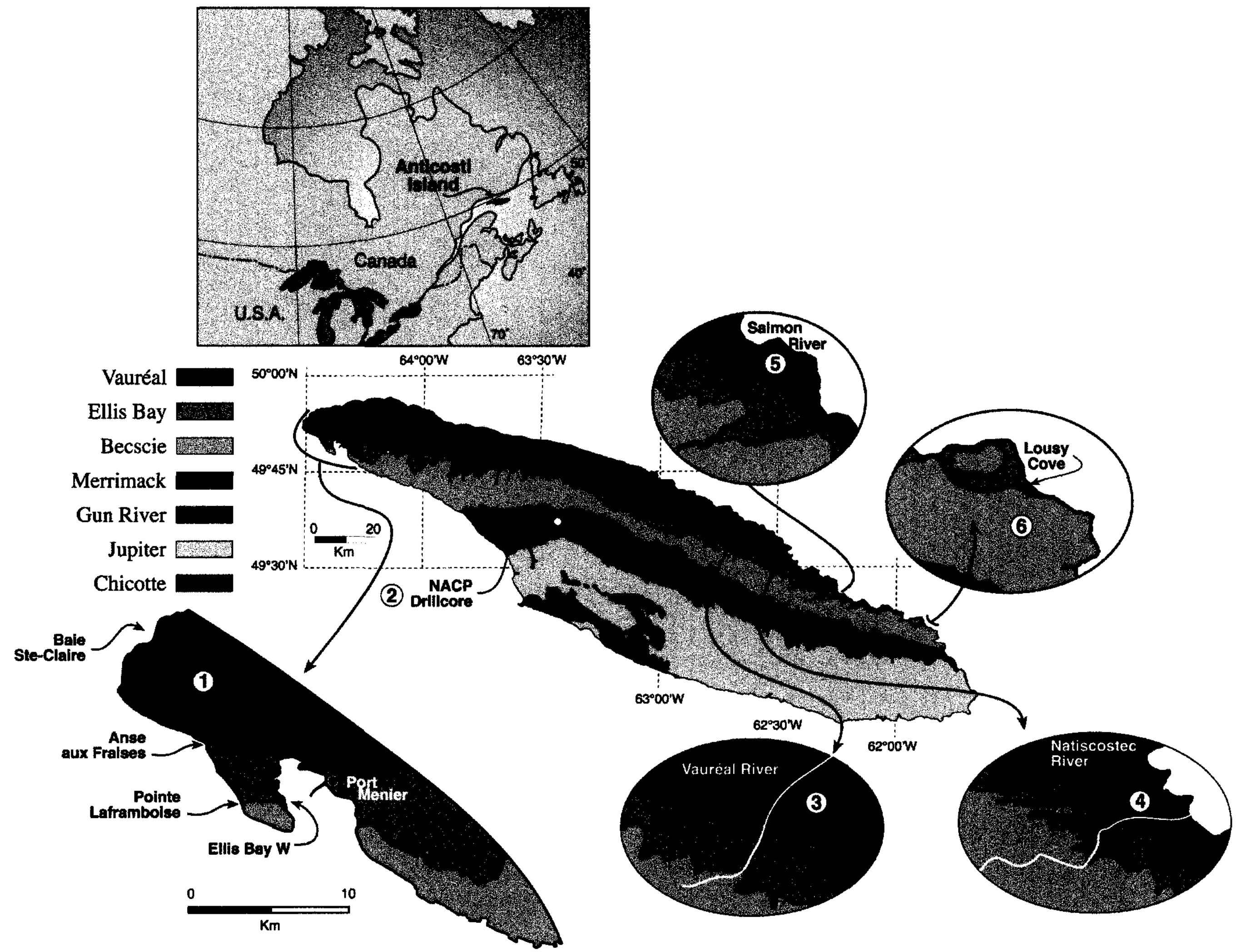

Anticosti Island
Canada
U.S.A.
50°
45°
70°
Vauréal
Ellis Bay
Becscie
Merrimack
Gun River
Jupiter
Chicotte
50°00'N
49°45'N
49°30'N
64°00'W
63°30'W
63°00'W
62°30'W
62°00'W
0
20
Km
NACP Drillcore
Salmon River
Lousy Cove
Vauréal River
Natiscostec River
Baie Ste-Claire
Anse aux Fraises
Pointe Laframboise
Ellis Bay W
Port Menier
0
10
Km

Figure 7. Stratigraphic correlation from the west end to the east end of Anticosti Island [3]. Five transgressive-regressive packages are identified, the uppermost of which represents the Laframboise Member (TR-5). Note the two unconformities near the top of the succession on the west end and the five unconformities in the east end succession. For a detailed legend of sedimentary features refer to Figure 10.

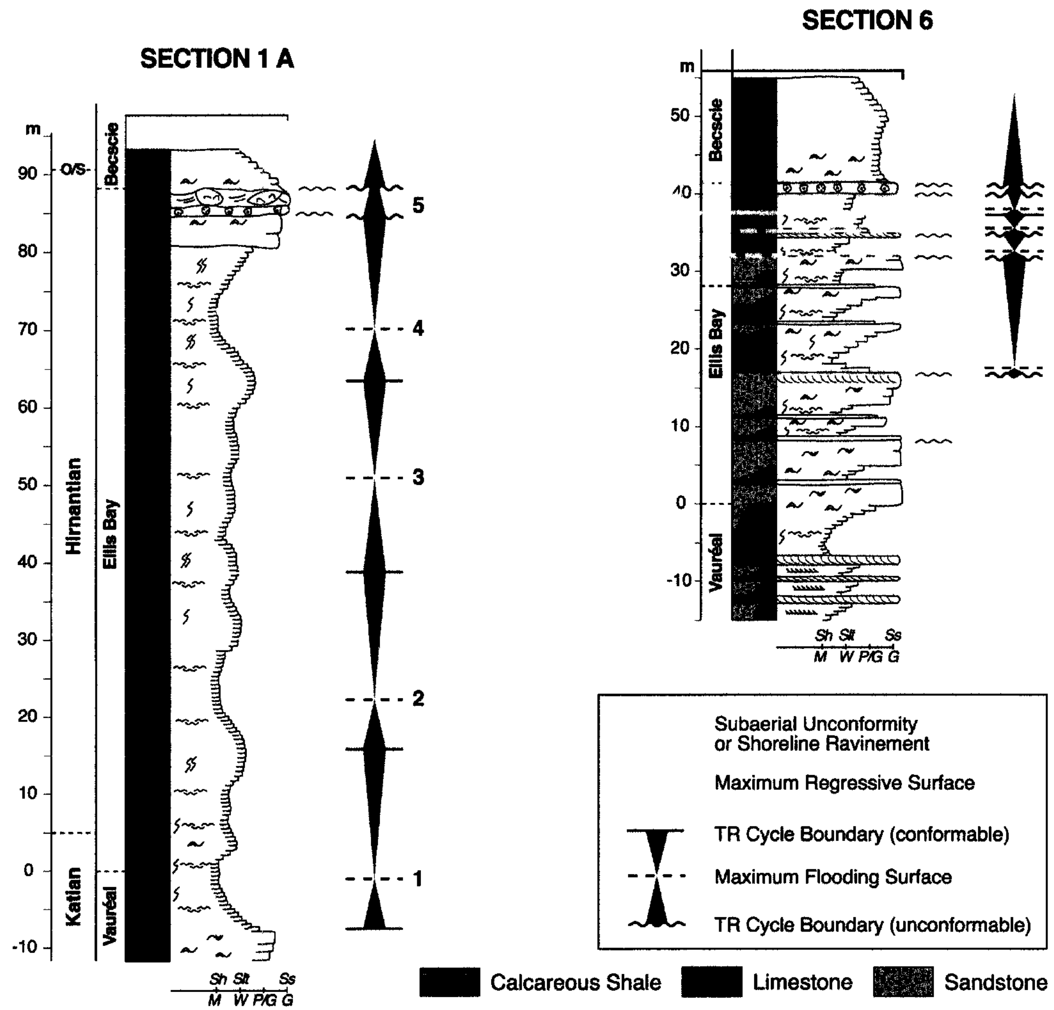

SECTION 1 A
SECTION 6
m
O/S
Becscie
Ellis Bay
Vauréal
Hirnantian
Katian
Sh Slt Ss
M W P/G G
Subaerial Unconformity or Shoreline Ravinement
Maximum Regressive Surface
TR Cycle Boundary (conformable)
Maximum Flooding Surface
TR Cycle Boundary (unconformable)
Calcareous Shale
Limestone
Sandstone

Member is bounded by two unconformities, which are presumed to represent the two periods of subaerial exposure during the Hirnantian glacial maximum.

Due to its nearshore depositional environment, the Ellis Bay Formation at the eastern end of Anticosti island shows a more incomplete and thinner record than the western end, typically only about 40 meters of strata. The eastern end also contains more unconformities. Nonetheless, strata can be correlated from the western side to the eastern side with the help of sequence stratigraphy and the support of biostratigraphy (Figure 7). The thickness and continuity of sediments within the Anticosti Basin increases as one moves progressively westward.

Four field photos are included to help illustrate the geology of the Ellis Bay Formation. A photo from the west end is shown (Figure 8A) in contrast with a photo from the east end of the island (Figure 8B). The Laframboise member at the west end (Figure 8C) terminates with a sharp erosive surface at the Ellis Bay-Becscie contact. In one location along Salmon River it is possible to observe both the Laframboise Member and the Vaureal-Ellis Bay contact (Figure 8D).

Methods

Samples were collected from six O-S boundary sections across the island (Figure 6), and integrated with existing stratigraphic frameworks [3,4]. The longest and most complete section sampled was the Baie St. Claire-Laframboise section (Section 1A) along the coastal exposure at the west end of Anticosti Island. Altogether this section stretches for approximately 4 kilometers in length and contains about 200 meters of upper Vaureal, Ellis Bay and lower Becscie strata. Another section at the west end, from the

Figure 8. Field photographs of the Ellis Bay Formation.

A) A typical cliff exposure at the west end of Anticosti Island, characterized by a shallowing-upwards regressive sequence that gradually shifts from recessive, argillaceous calcarenite at the bottom to increasingly well-bedded proximal storm deposits near the top.

B) The Ellis Bay Formation at east end of Anticosti Island. Thinner regressive packages occur than found at the west end of the island. Several individual regressive packages are capped with erosive surfaces. TR-5 represents the Laframboise Member, a bed of oncolitic limestone.

C) The Laframboise Member (TR-5) on the west end of Anticosti Island. A large bioherm is resting on oncolitic limestone. The bioherm is capped by an erosive surface and is progressively onlapped by the storm deposits of the Becscie Formation. The O-S boundary is located approximately five meters above this erosive surface [3].

D) A location along Salmon River (Section 5), where both the Laframboise Member (TR 5) and the Vaureal-Ellis Bay contacts (TR-1) are visible. In this locality, the Ellis Bay Formation is restricted to approximately 25 meters of strata.

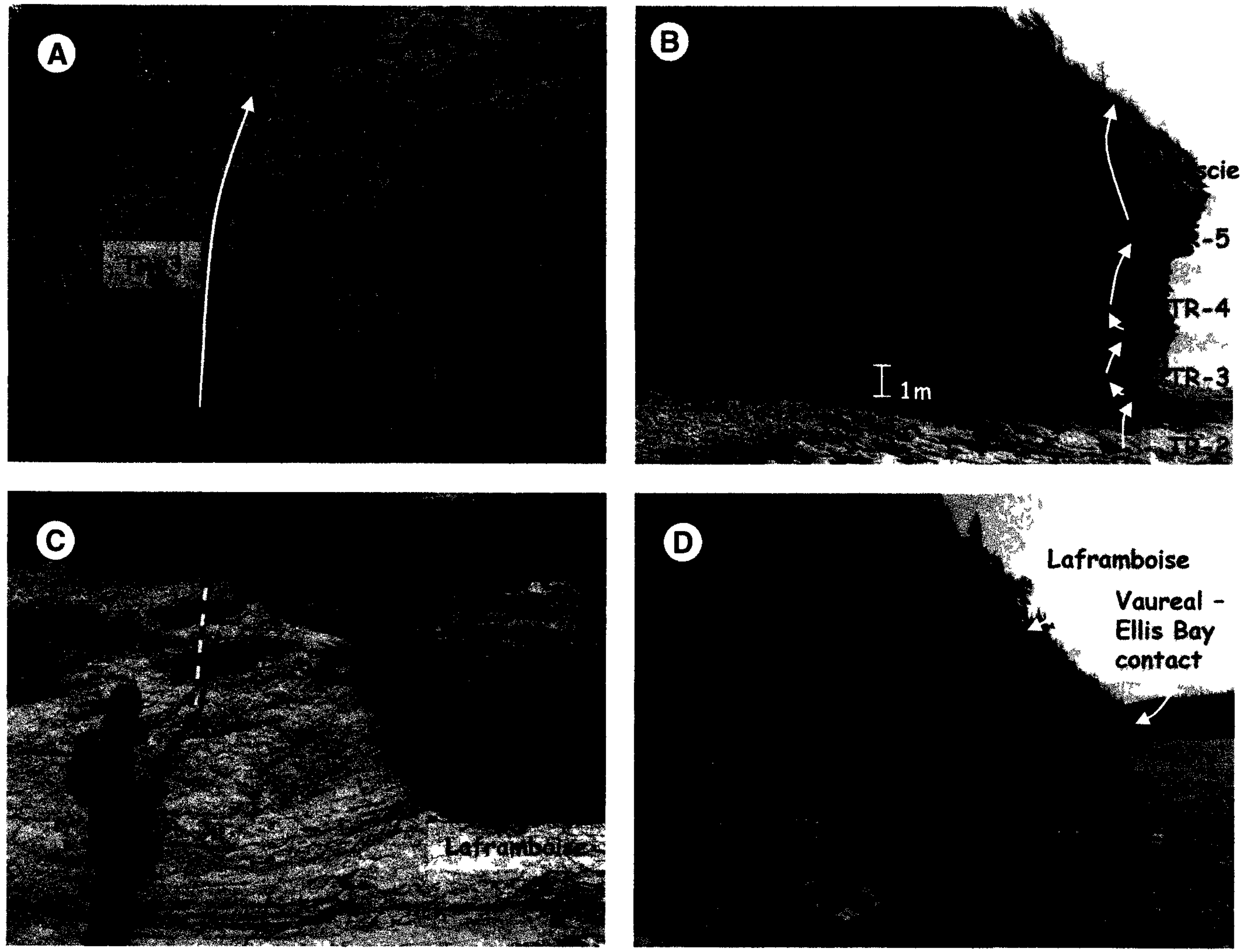
A
B
-5
TR-4
TR-3
1m
C
D
Laframboise
Vaureal -
Ellis Bay
contact

west side of Ellis Bay (Secton 1B), was sampled but only represented a portion of the upper Ellis Bay and the lower Becscie. Subsurface data from the NACP drill core (Section 2) at N49° 62.073', W063° 43.791' is also included in this thesis. This site is useful as it helps bridge the large gap between western sections and our more easterly sections. Further to the east, samples were collected from a river section (Section 3) adjacent to Vaureal Falls in the National Park of Anticosti. Two more river valley sections along the Natiscotec and Salmon rivers (Section 4 and 5, respectively) were sampled further to the east, each covering about 100 meters of strata. The easternmost exposure of the Ellis Bay Formation was sampled at the coastal locality of Lousy Cove (Section 6).

Sections were sampled at varying densities, but on average approximately one sample for every one or two meters of strata was collected. Sampling density increased at or near the Ellis Bay-Becscie contact. Sampling sites were routinely marked by GPS. The sediments in the Ellis Bay Formation range from pure micrite (Figure 9A) to peloidal grainstone (Figure 9D). The majority of samples are from the micritic matrix within wackestones (Figure 9B) and packstones (Figure 9C). The sediments contain a diverse and well-preserved fossil assemblage of brachiopods, crinoids, corals, bryozoans, stromatoporoids and mollusks.

After collection, samples were cut and drilled and $CaCO_3$ powder was extracted from material containing high proportions of micrite and lacking shelly fossils. Samples of $CaCO_3$ powder between approximately 0.4 to 0.8 mg were then weighed into exetainers, and 0.1 mL of H_3PO_4 was added. The exetainers were then flushed with Helium while horizontal before reaction. Samples were reacted at 25.0°C and placed into

Figure 9. Photographs of thin sections of Ellis Bay Formation sediments [43], showing a range of different compositions. The slides have been stained with Alizarin Red and Potassium Ferrocyanide.

A) Well-preserved bioturbated mudstone, with rare skeletal fragments and peloids.

B) Bioturbated crinoid wackestone, with rare peloids in a matrix of fine-grained micrite.

C) Brachiopod-rich packstone, with rare trilobite fragments in a matrix of fine-grained micrite.

D) Fine-grained laminated peloid grainstone.

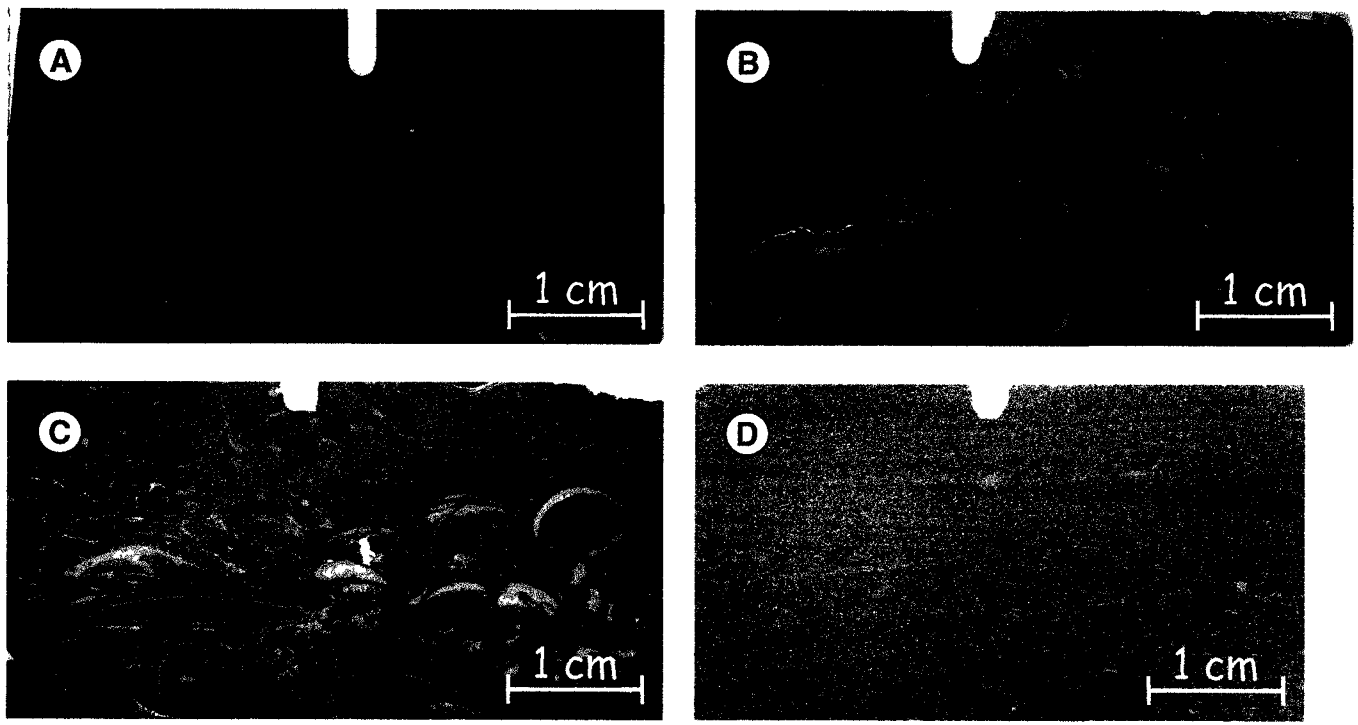
A
1 cm
B
1 cm
C
1 cm
D
1 cm

a Thermo Finnigan Delta XP mass spectrometer at the G.G. Hatch Isotope Laboratory at the University of Ottawa, which measured $\delta^{13}C$ and $\delta^{18}O$ ratios of the CO_2 in the exetainers to a precision of $\pm$ 0.1‰. The results of these isotopic measurements are compiled in Appendix B.

Six samples from section 1B exhibited minor dolomitization. These partially dolomitized samples were later reanalyzed at the G.G. Hatch Laboratory using a longer reaction time prior to extraction. The $\delta^{13}C$ values obtained using this new method were not significantly different from the original measurements (Appendix C).

Geochemical Proxies

$\delta^{13}C$ and $\delta^{18}O$ act as proxies for estimating certain properties of ancient oceans, climates and biospheres. These isotope proxies measured in Ordovician sediments and fossils are a reflection of the isotopic concentration in the ocean at the times of their original deposition [44].

$\delta^{18}O$ is a favoured temperature proxy for palaoeclimatic studies over a range of different timescales [44,45,46,47]. The ratio of heavy oxygen (^{18}O) to light oxygen (^{16}O) in water is known to vary naturally in response to Rayleigh fractionation during the meteoric cycle, where light oxygen is preferentially evaporated and then preferentially stored in ice. Thus periods of significant continental glaciation are marked by an increase in $\delta^{18}O$ values of the oceans [48]. Over longer timescales, oceanic $\delta^{18}O$ is influenced by circulation of seawater through oceanic crust, where oxygen from water and silicates is exchanged [49]. The temperature of seawater affects the oxygen isotope composition of carbonate fossils and sediments, where a change of 1 ‰ in the $\delta^{18}O$ of carbonate is equivalent to approximately 4°C change in temperature [50].

$\delta^{13}C$ can be used as a proxy for the global carbon cycle [51]. Changes in $\delta^{13}C$ values in the ocean reflect changing distributions of heavy (^{13}C) and light (^{12}C) carbon in the different global reservoirs of carbon: the oceans, the atmosphere, the biosphere and the lithosphere. The largest fractionation process for carbon isotopes is photosynthesis [52], as plants and algae preferentially utilize the lighter ^{12}C isotope. $\delta^{13}C$ in organic matter is typically 25 to 30 ‰ lighter relative to dissolved inorganic carbon [53]. Episodes of increased primary productivity are suggested to be responsible for some instances of increased oceanic $\delta^{13}C$ in the geological past [9]. $\delta^{13}C$ ratios in carbonate fossils are also influenced by the pH of seawater, due to varying proportions of the dissolved inorganic carbon species CO_2, H_2CO_3, HCO_3^- and CO_3^{2-}, and their different isotopic fractionation factors [54]. Another often cited reason for increases in oceanic $\delta^{13}C$ is sequestration and burial of organic carbon in sediments [55], including the deposition of black shale and fossil fuels. Apart from biological fractionation, it has also been suggested that differing rates of the weathering of carbonates can affect the $\delta^{13}C$ composition of the oceans [10].

Diagenesis can affect the original isotopic composition of carbonate sediments through dissolution of $CaCO_3$ and subsequent reprecipitation. The most important diagenetic pathway that affects the isotope composition of marine carbonates is replacement by meteoric water, which carries lighter values of $\delta^{13}C$ and $\delta^{18}O$. Oxygen isotopes are much more sensitive to replacement because pore fluids contain large amounts of oxygen in water molecules. The process of $\delta^{13}C$ and $\delta^{18}O$ replacement is achieved through neomorphism during burial or exposure, where the micrite matrix is modified to a microspar/pseudospar fabric as well as unstable aragonite and high-Mg calcite grains and cement are stabilized to a more stable calcitic mineralogy. Diagenesis also tends to decrease the overall Sr^{2+} and Mg^{2+} content in the rock, and increase concentrations of the reduced ions Fe^{2+} and Mn^{2+} after burial. On Anticosti Island, the sediments were deposited during a time of calcite seas [56], where calcite was the dominant polymorph of precipitated inorganic $CaCO_3$. Therefore the amount of neomorphic replacement is generally less than in Cretaceous and Cenozoic limestones, and the fabrics tend to be much better preserved [57].

Occasionally discussed is the notion of whether $\delta^{13}C$ and $\delta^{18}O$ measurements from micrite samples should be used for paleoenvironmental reconstruction [58], as they are often altered by diagenesis. Shells of brachiopods and some other low-Mg calcite fossils are recognized as more reliable proxies as their calcite is a more stable polymorph that is less susceptible to exchanges with the surrounding medium. In brachiopod shells, the incorporation of oxygen isotopes occurred at the time of deposition, preserving the isotopic composition of the ancient ocean [44,59,60,61]. The present study considers bulk carbonates on Anticosti Island to also preserve the original isotopic signature, as the micrite has been cemented early at a time when pore waters were essentially similar to occluded seawater. Thin sections revealed that micrite samples from the Ellis Bay Formation are very poor in iron and other trace elements. They are also non-luminescent under cathodoluminescence microscopy [43], suggesting that diagenetic stabilization occurred very early. Evidence for other processes that may affect isotopic values like dolomitization and microspar/pseudospar neomorphism are rare in the Ellis Bay

Formation. In addition, maturation studies indicate that the Ellis Bay micrites did not reach burial temperature greater that 80°C [62] and burial depth greater than two kilometers [63]. In our study a set of seven brachiopod samples was analyzed, and were determined to be similar to the $\delta^{13}C$ and $\delta^{18}O$ signatures of micrites from the same layers (Appendix D). Separate carbon isotope studies performed on a Silurian section in Gotland, Sweden using micrites [64] and brachiopod shells [65] yielded essentially identical results, as described in Cramer and Saltzmann [55]. In 2003, Brenchley et al. [5], analyzed $\delta^{13}C$ from whole rock carbonates alongside $\delta^{13}C$ in brachiopods, which while not identical, parallel each other (see Figure 24). All of these studies together with our observations suggest that the Ellis Bay micrites on Anticosti Island are as reliable as brachiopod shells for retaining near-original trends in carbon isotope signature, particularly if interpretation is restricted to signals in excess of the largest observed deviation of 0.87 ‰ (Appendix D).

Results

Presented in this section are the results of the isotope study on the micrites of the Ellis Bay Formation. Six sections were sampled in this study (Figure 6), and they will be presented from west to east, as they are listed in Appendix B. The main focus of this study is the $\delta^{13}C$ results, which will be interpreted in detail in a later section and compared with other O-S boundary sections around the world. $\delta^{18}O$ results are also briefly reported.

The data obtained from section 1A at the west end of Anticosti Island was the most extensive and complete of all the studied sections (Figure 10). 135 samples were

Figure 10. $\delta^{13}C$ and $\delta^{18}O$ isotope data for section 1A, the Baie St Claire-Laframboise composite section on the west end of Anticosti Island. Height above the base of the section in meters and stratigraphy defined in Petryk [66] and Copper [12] is displayed on the left. Nine regressive-transgressive cycles have been identified for this section, four in the Katian and five in the Hirnantian (TR-1 to TR-5 in Figure 7). Two unconformities near the top of the section are indicated. Maximum flooding surfaces are marked with horizontal dashed lines and maximum regressive surfaces are marked with solid lines. The mean for the pre-Hirnantian background is indicated with a vertical dashed line and its 95 % confidence interval is represented by the yellow shaded region.

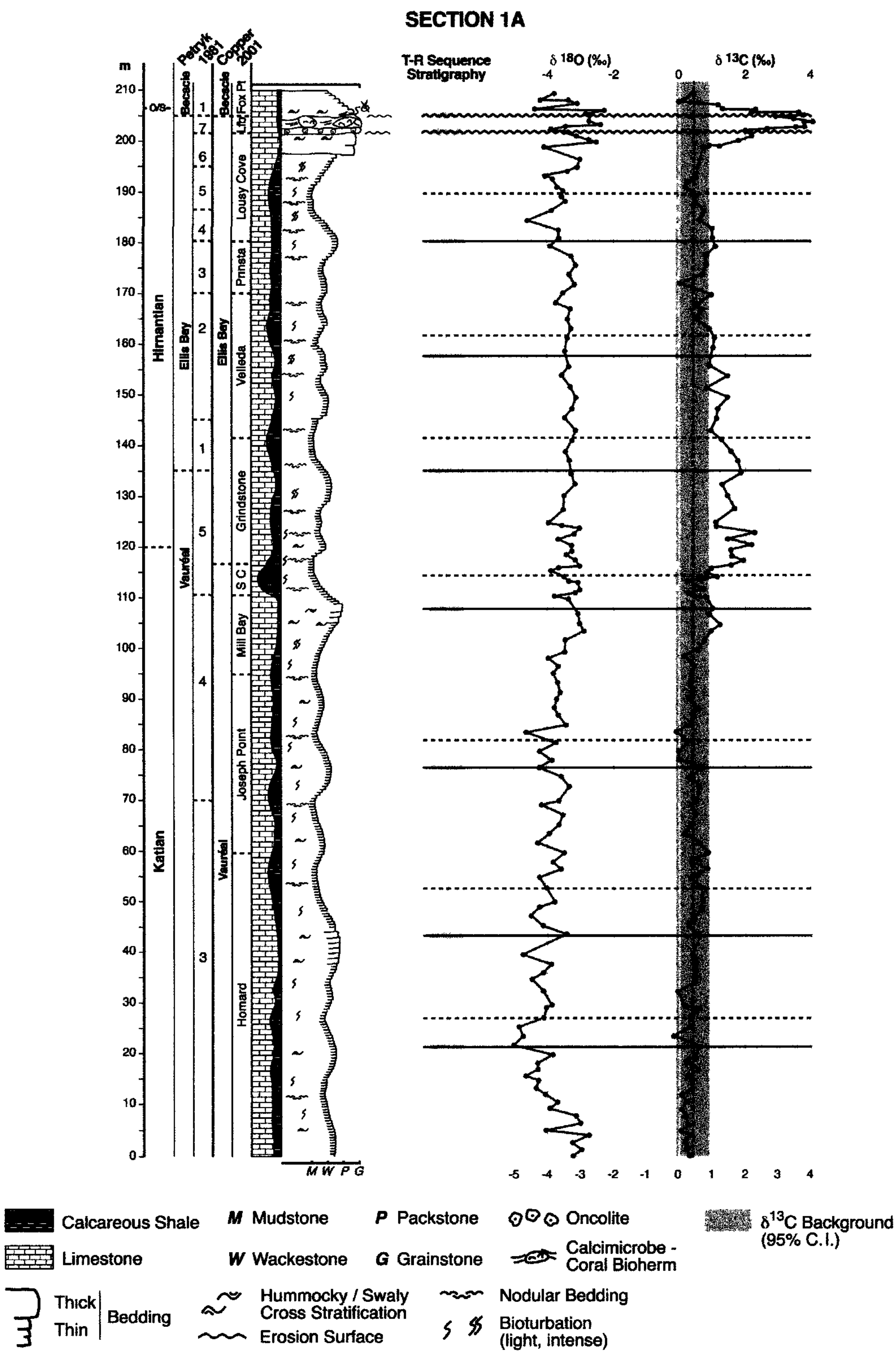

SECTION 1A
m
Petryk 1981
Copper 2001
Becscie
Ellis Bay
Vauréal
Himantian
Katian
Fox Pt
Lousy Cove
Prinsta
Velleda
Grindstone
S C
Mill Bay
Joseph Point
Homard
M W P G
T-R Sequence Stratigraphy
δ 18O (‰)
δ 13C (‰)
Calcareous Shale
Limestone
M Mudstone
W Wackestone
P Packstone
G Grainstone
Oncolite
Calcimicrobe - Coral Bioherm
δ13C Background (95% C.I.)
Thick
Thin
Bedding
Hummocky / Swaly Cross Stratification
Erosion Surface
Nodular Bedding
Bioturbation (light, intense)

collected from a coastal exposure that represents just over 210 meters of strata starting at the upper Vaureal Formation and extending into the base of the Becscie Formation. This data shows that in the Vaureal, the first 105 meters of the section, $\delta^{13}C$ values are relatively stable and contained between values of approximately 0 and 1 ‰, with a mean of 0.4 ‰ and a standard deviation of 0.25 ‰. These represent the background values for $\delta^{13}C$ before the Hirnantian. Approximately at the Vaureal-Ellis Bay boundary, there is a $\delta^{13}C$ excursion, where $\delta^{13}C$ values rise and peak at approximately 2 ‰. $\delta^{13}C$ values in the 50 metres of strata between approximately 105 meters and 155 meters are consistently above 1 ‰. The values in this interval have a mean of 1.23 ‰, which is significantly above the pre-Hirnantian background ($p = 2.4$ %). Toward the middle of the Ellis Bay, between 155 and 195 meters $\delta^{13}C$ returns to values similar to the background. $\delta^{13}C$ values in this interval have a mean of 0.7 ‰, which is not significantly above the background ($p = 6.5$ %) . A second much larger excursion in $\delta^{13}C$ values occurs in the later part of the Ellis Bay, peaking at values of approximately 4 ‰. This main $\delta^{13}C$ excursion occurs in the Laframboise Member at the top of the Ellis Bay Formation, which is bounded by two unconformities. $\delta^{13}C$ values increase to a value of approximately 2 ‰ leading up to the lower Laframboise unconformity. There is an offset in $\delta^{13}C$ values where the unconformity lies, and the peak of the excursion can be observed in the middle part of the Laframboise Member. The excursion wanes sharply following the upper Laframboise unconformity, where another slight offset in $\delta^{13}C$ values can be seen. In this section, the second $\delta^{13}C$ excursion occurs between approximately 195 and 205 meters, where the mean of 2.5 ‰ is significantly above the background ($p = 0.9$ %). In the lower part of the Becscie Formation above 205 meters, the mean in $\delta^{13}C$ values is 0.65 ‰, signifying a restoration of background values above the upper Laframboise unconformity (p = 7.8 %). The second $\delta^{13}C$ excursion is approximately concurrent with the uppermost transgressive-regressive sequence defined in Figure 7 (TR-5) and the estimated duration for the excursion lies between 100,000 and 500,000 years [3].

$\delta^{18}O$ data from this locality displays a different pattern. The values are bounded between -2.5 and -5 ‰. There is a decrease in $\delta^{18}O$ values near the base of the section, from 0 to 20 meters. After this, values oscillate and converge at a value of approximately -3 ‰. There is considerable variation near the end of the section in the Laframboise Member, approximately parallel with the main $\delta^{13}C$ excursion. Over this entire section $\delta^{18}O$ values have a mean of approximately -3.6 ‰ and a standard deviation of 0.5 ‰.

Another section at the west end of the island was also sampled. 46 samples were collected from section 1B at the west side of Ellis Bay (Figure 11), spanning 28 meters of the upper Ellis Bay and basal Becscie formations. This corresponds with the strata above 190 meters in section 1A. The data displays only the second $\delta^{13}C$ excursion of 4 ‰, followed by a sharp return to background values. As in section 1A, the excursion is offset by the two unconformities that bound the Laframboise Member on the west end of the island. The $\delta^{13}C$ values increase from the base of the section in the upper Ellis Bay Formation, up to the first unconformity at the base of the Laframboise. Below the excursion, in the basal 6 meters of the section, $\delta^{13}C$ values have a mean of approximately 0.5 ‰ and a standard deviation of 0.25 ‰. The excursion is present in the interval between 197 and 206 meters, $\delta^{13}C$ values peak at approximately 3.4 ‰, have a mean of 1.89 ‰ and a standard deviation of 0.92 ‰. There is a sharp decrease in $\delta^{13}C$ values following the second unconformity at the top of the Laframboise Member, and the data

Figure 11. $\delta^{13}C$ and $\delta^{18}O$ isotope data for section 1B, on the west side of Ellis Bay at the west end of Anticosti Island. The shaded area represents the Laframboise Member at the top of the Ellis Bay Formation, which is bounded by two unconformities. The mean for the post-Hirnantian background is indicated with a vertical dashed line and its 95 % confidence interval is represented by the yellow shaded region. For a detailed legend refer to Figure 10.

SECTION 1B

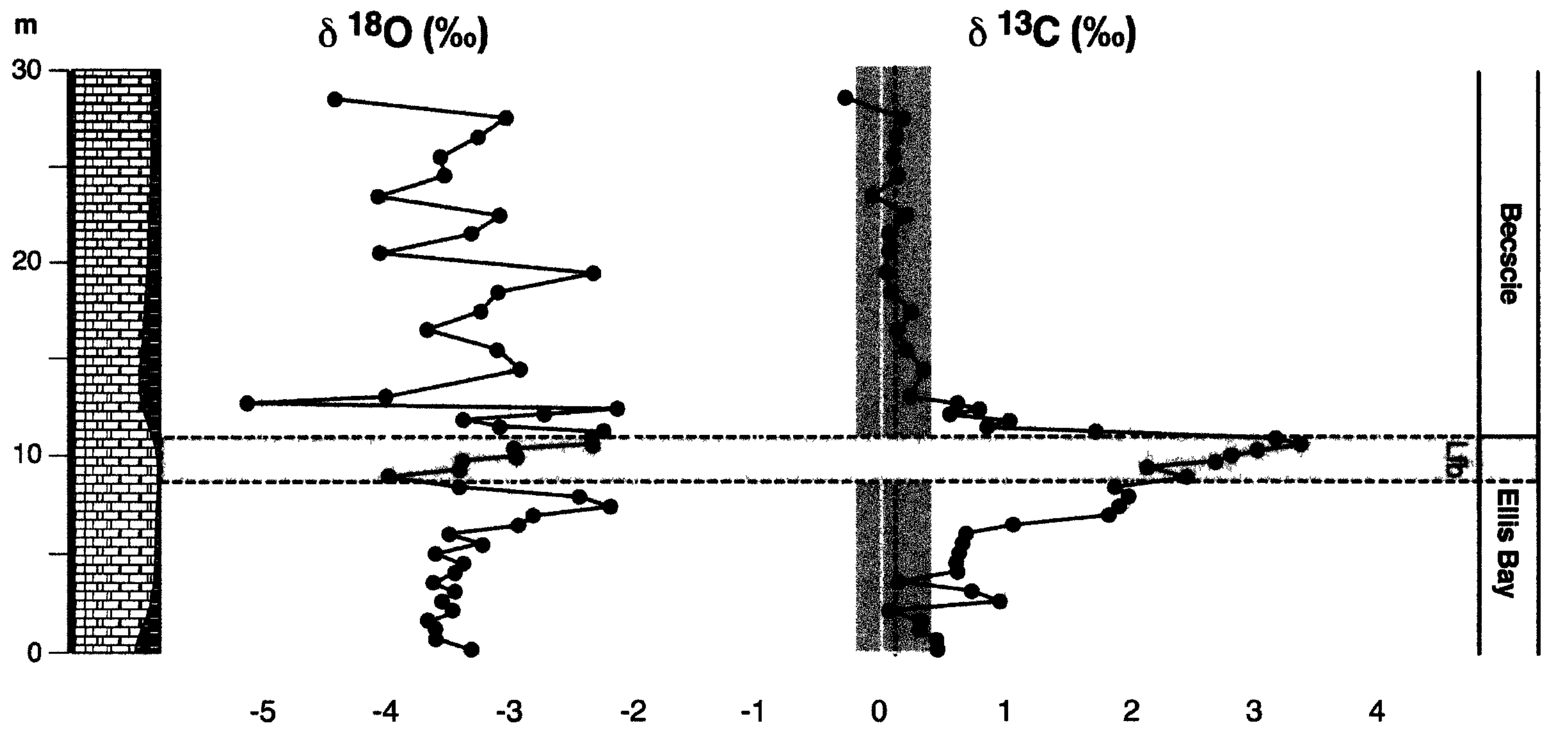

from the Becscie Formation above the excursion is noticeably uniform, converging around a value of approximately 0 ‰. The uppermost 8 meters in this section has a $\delta^{13}C$ mean of 0.27 ‰ and a standard deviation of 0.32 ‰. If one defines this uppermost interval as the post-Hirnantian background, the excursion is quite significant with a p-value of 1.3 %.

$\delta^{18}O$ data from Ellis Bay is somewhat sporadic and oscillates between values of approximately -2 and -5 ‰ following the main $\delta^{13}C$ excursion, although it appears more uniform prior to the $\delta^{13}C$ excursion. Overall, at this locality $\delta^{18}O$ measurements have a mean of -3.3 ‰ and a standard deviation of 0.6 ‰.

Data obtained from section 2, the NACP drill core located in the interior of the island (Figure 12), was used in this study to help bridge the gap between the west end section and the central and eastern sections. 43 samples were taken from a core spanning about 95 meters from the uppermost Vaureal to the basal Becscie formations. A $\delta^{13}C$ excursion of 2 ‰ is present near the base of the Ellis Bay followed by a slow return to background values of between 0 and 1 ‰. This is followed by a second larger $\delta^{13}C$ excursion of 4 ‰ near the Ellis Bay-Becscie contact. The NACP drill core was useful in this study for establishing biostratigraphic and sequence stratigraphic correlations across the island, as shown in Figure 12.

Further to the east, 60 samples were collected from section 3, a 120-meter section on the Vaureal River (Figure 13). This section comprises most of the Vaureal and Ellis Bay formations, but does not include the Laframboise Member. The results display similar trends in $\delta^{13}C$ as at the west end, although the second excursion is not completely visible. $\delta^{13}C$ values of between 0 and 1 ‰ are observed within the Vaureal. This is

Figure 12. Correlations of biostratigraphy, sequence stratigraphy and $\delta^{13}C$ isotope stratigraphy between the east and west end of Anticosti Island. Section 1 is shown on the left and section 6 is shown on the right. $\delta^{13}C$ isotope data for section 2, an NACP drillcore, is shown in the middle. For a detailed legend refer to Figure 10.

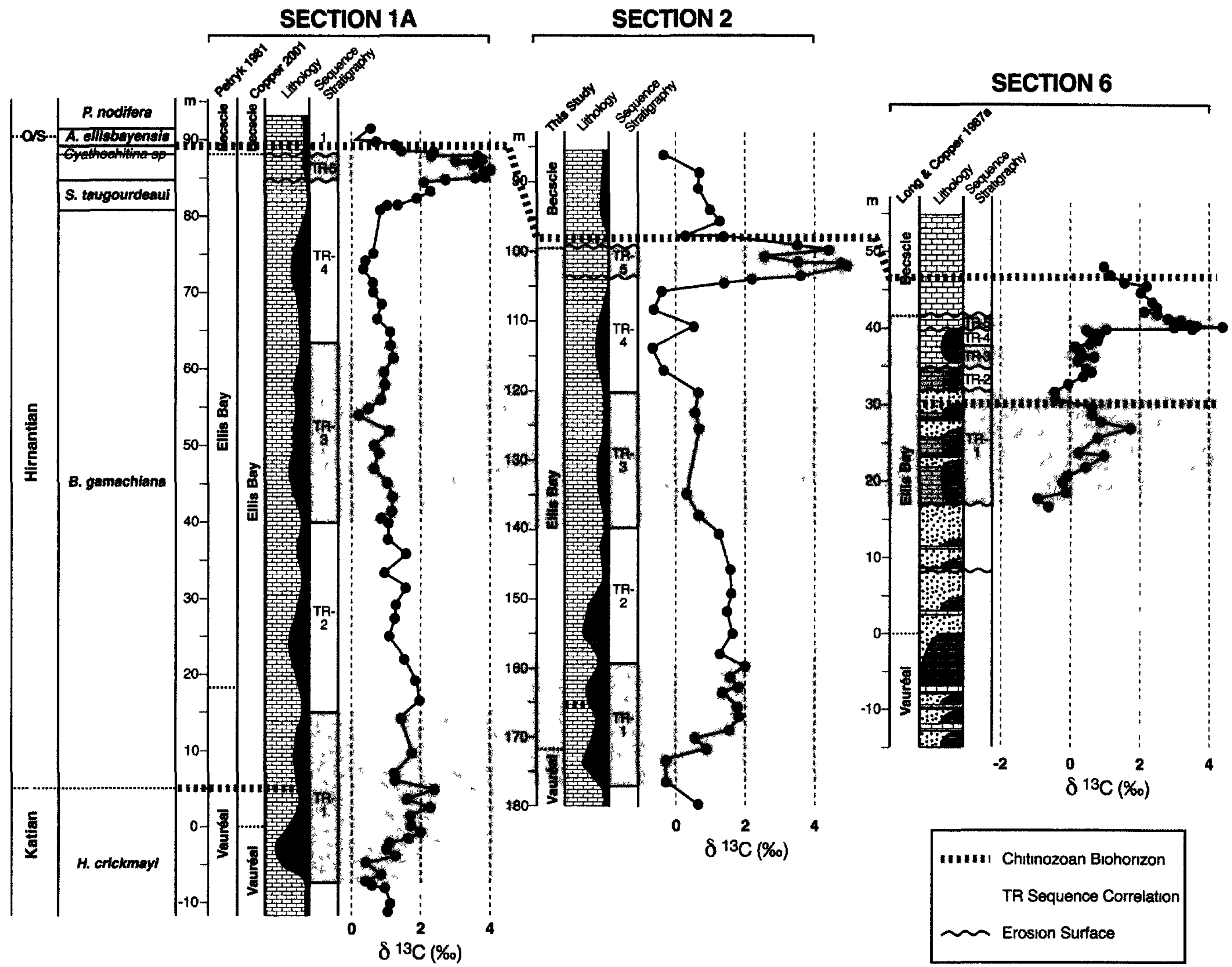

SECTION 1A
SECTION 2
SECTION 6
Petryk 1981
Copper 2001
Lithology
Sequence Stratigraphy
This Study
Long & Copper 1987a
O/S
P. nodifera
A. ellisbayensis
Cyathochitina sp.
S. taugourdeaui
B. gamachiana
H. crickmayi
Hirnantian
Katian
Becscie
Ellis Bay
Vauréal
TR-1
TR-2
TR-3
TR-4
TR-5
δ 13C (‰)
Chitinozoan Biohorizon
TR Sequence Correlation
Erosion Surface

Figure 13. $\delta^{13}C$ and $\delta^{18}O$ isotope data for section 3, at Vaureal River. Note that the Vaureal-Ellis Bay contact of previous studies lies at approximately 50 meters. For a detailed legend refer to Figure 10.

SECTION 3

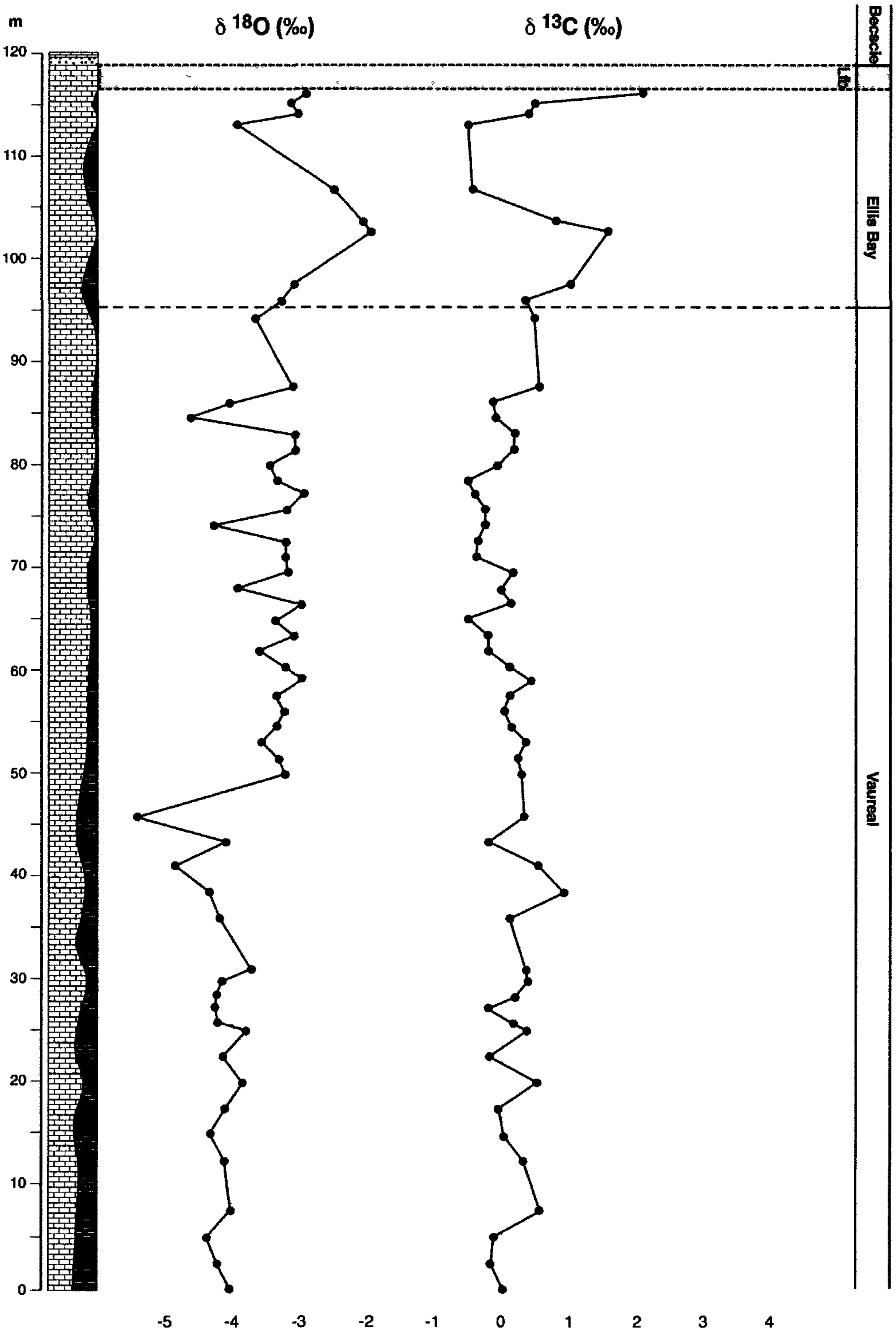

m
δ 18O (‰)
δ 13C (‰)
Becscie
Lfb
Ellis Bay
Vaureal
120
110
100
90
80
70
60
50
40
30
20
10
0
-5
-4
-3
-2
-1
0
1
2
3
4

followed by a 2 ‰ excursion in $\delta^{13}C$ near the Vaureal-Ellis Bay contact and a return to background values. The rising limb of the main $\delta^{13}C$ excursion seen in other sections is apparent at the top of the section.

Most of the $\delta^{18}O$ measurements from section 3 have values between -3 and -5 ‰, although one value less than -5 ‰ and some values higher than -3 ‰ were recorded. $\delta^{18}O$ values in the upper 65 meters seem to be slightly more enriched than the values in the lower 50 meters of this section, although this is mostly within the variation of the measurements as a whole. Altogether the $\delta^{18}O$ measurements from this section have a mean of -3.6 ‰ and a standard deviation of 0.7 ‰. There are two measurements near the top of the section, at 103 and 104 meters that are significantly above this mean.

75 samples were collected from section 4, another exposure at Natiscotec River (Figure 14). This section involved a span of approximately 120 meters of strata from the Vaureal to the lower Becscie. The lower part of this section displays a relatively stable background, with values mostly between 0 and 1 ‰. Near the top of the section, beginning right below the Laframboise Member, a $\delta^{13}C$ excursion is present, with a peak value of approximately 3.5 ‰. On top of the Laframboise member, $\delta^{13}C$ values exhibit a marked return to background values. The first $\delta^{13}C$ excursion that was typically observed near the Vaureal-Ellis Bay contact is not evident in Section 4. This could be explained by the fact that sampling was less dense in the middle part of this section due to logistical problems and time constraints.

The $\delta^{18}O$ measurements from this location are bounded between values of -3 and -5 ‰, and oscillate around values of approximately 4 ‰. $\delta^{18}O$ has a mean of -3.8 ‰ and a standard deviation of 0.5 ‰. Section 4 contains a single low $\delta^{18}O$ measurement of

Figure 14. $\delta^{13}C$ and $\delta^{18}O$ isotope data for section 4, at Natiscotec River. For a detailed legend refer to Figure 10.

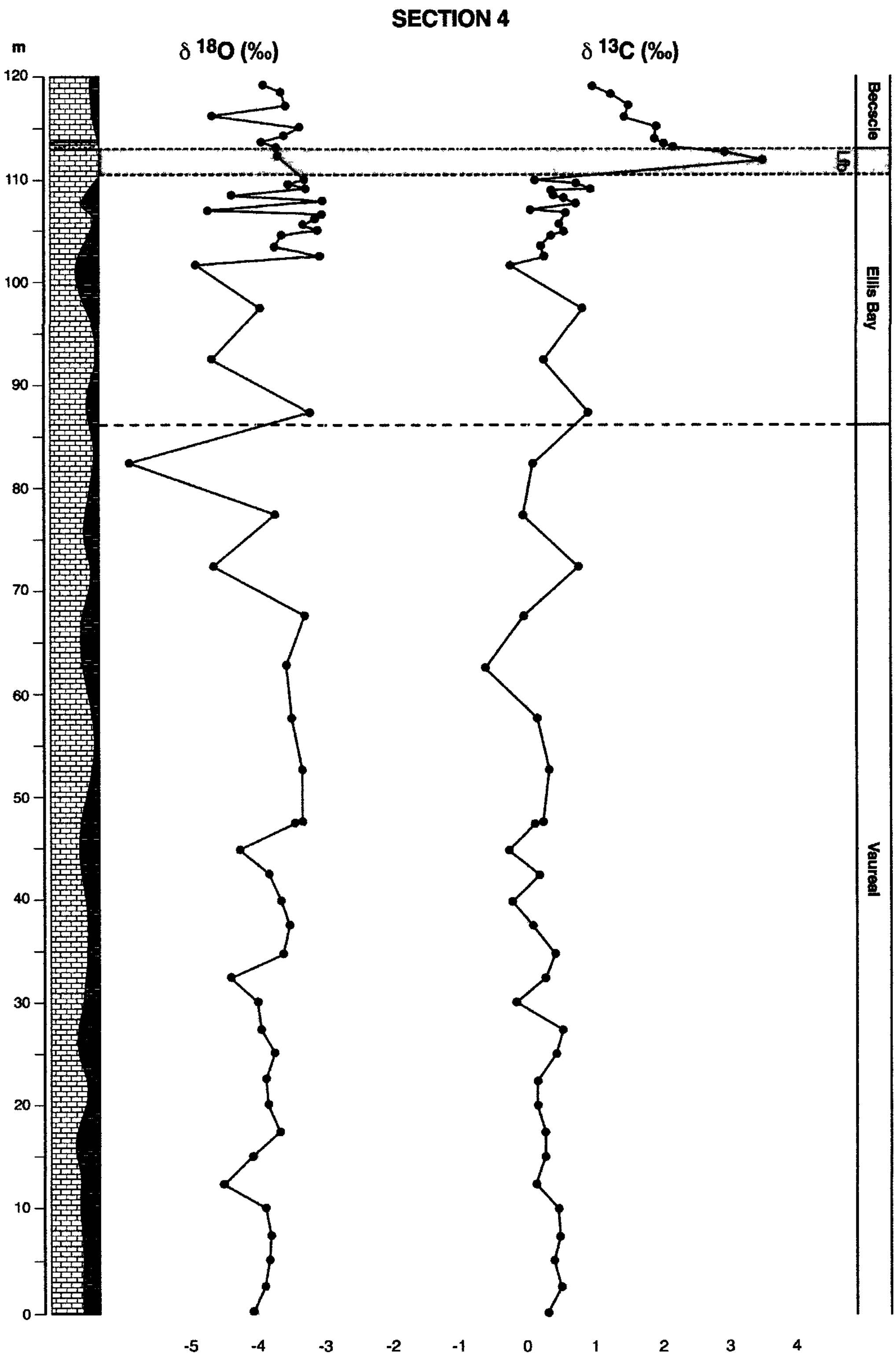

SECTION 4
m
δ 18O (‰)
δ 13C (‰)
120
110
100
90
80
70
60
50
40
30
20
10
0
-5
-4
-3
-2
-1
0
1
2
3
4
Becscie
Lfb
Ellis Bay
Vaureal

approximately -6 ‰, between 80 and 85 meters.

76 samples were collected from section 5 at Salmon River over a stratigraphic span of 35 meters ranging from the uppermost Vaureal to the basal Becscie formations (Figure 15). The $\delta^{13}C$ data displays values of approximately 0 to 1 ‰ in the Vaureal. Near the Vaureal-Ellis Bay contact a $\delta^{13}C$ excursion of approximately 2 ‰ and a slow return to background values up to the upper Ellis Bay Formation is observed. A larger $\delta^{13}C$ excursion peaking at approximately 4 ‰ is present right above the base of the Laframboise Member. Background values are once again restored above the Laframboise Member in a steady decline. There are significant offsets between $\delta^{13}C$ values on either side of the upper Laframboise unconformity.

$\delta^{18}O$ measurements from Salmon River were mostly contained within a band between -3 and -5 ‰, with a mean of approximately -3.6 ‰ and a standard deviation of 0.8 ‰. There is one exceptional value around 35 meters where $\delta^{18}O$ is approximately -6 ‰.

The easternmost locality sampled was section 6, a coastal section at Lousy Cove (Figure 16). 53 samples were collected from section 6 over a span of about 30 meters ranging from the middle Ellis Bay to the lower Becscie. At Lousy Cove, the Ellis Bay Formation is slightly more than 40 meters thick and contains several unconformities. The east end of Anticosti Island also contains more siliciclastic components as a result of its proximity to a nearshore environment. Despite this, the basic trends in the $\delta^{13}C$ values are very similar to those seen in the more westerly sections. $\delta^{13}C$ values are lowest near the middle of the Ellis Bay Formation, at approximately -1 ‰, and reach a peak at a value of 2 ‰ about 10 meters above the base of this section. Following this, there is a

Figure 15. $\delta^{13}C$ and $\delta^{18}O$ isotope data for section 5, at Salmon River. For a detailed legend refer to Figure 10.

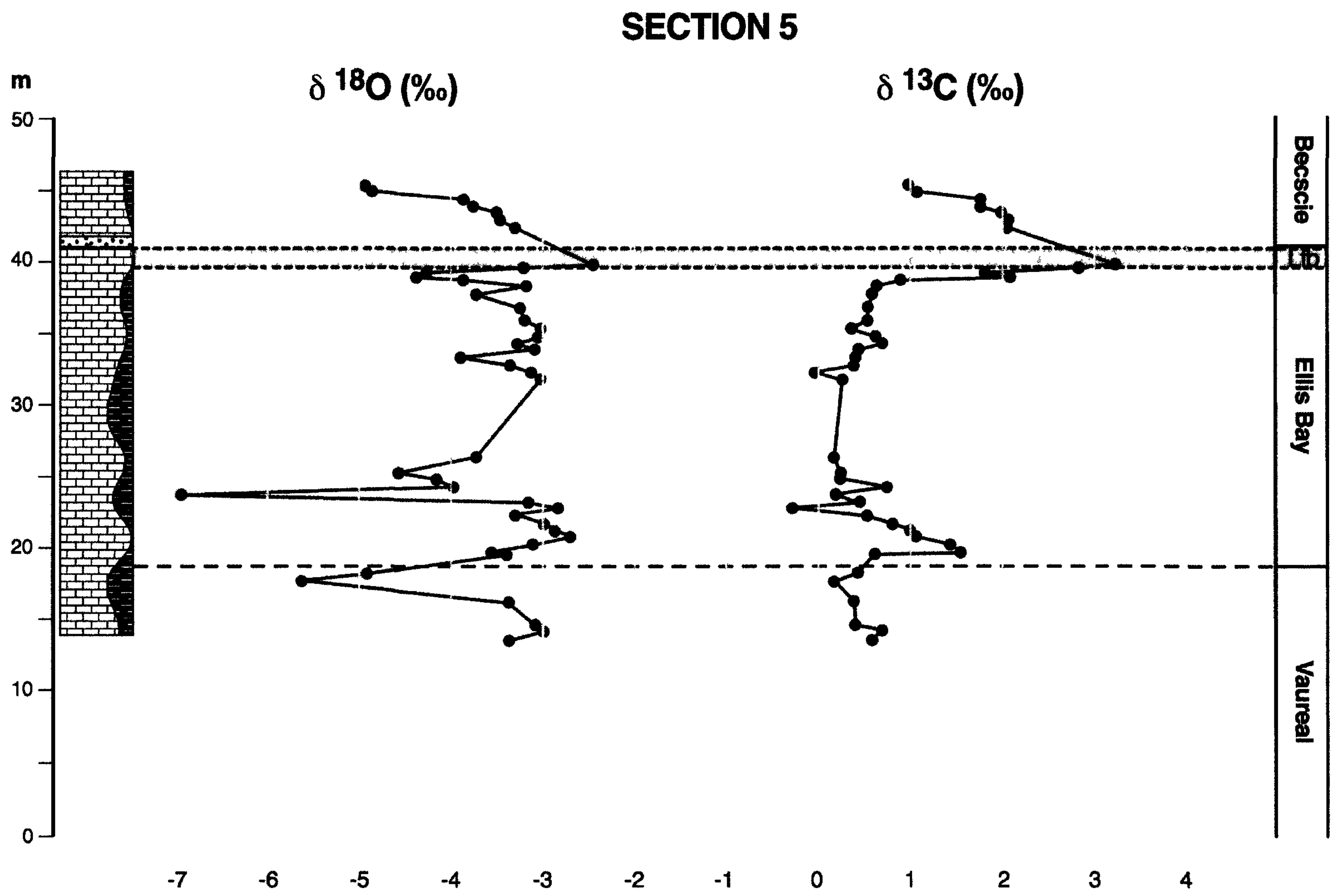
SECTION 5
m
δ 18O (‰)
δ 13C (‰)
50
40
30
20
10
0
-7
-6
-5
-4
-3
-2
-1
0
1
2
3
4
Becscie
Lb
Ellis Bay
Vaureal

Figure 16. $\delta^{13}C$ and $\delta^{18}O$ isotope data for section 6, at Lousy Cove on the east end of Anticosti Island, along with T-R sequence stratigraphy [3]. Maximum flooding surfaces are marked with dashed lines and maximum regressive surfaces are marked with solid lines. Note the different lithostratigraphic schemes from Copper 2001 [12] on the left and for this study on the right.

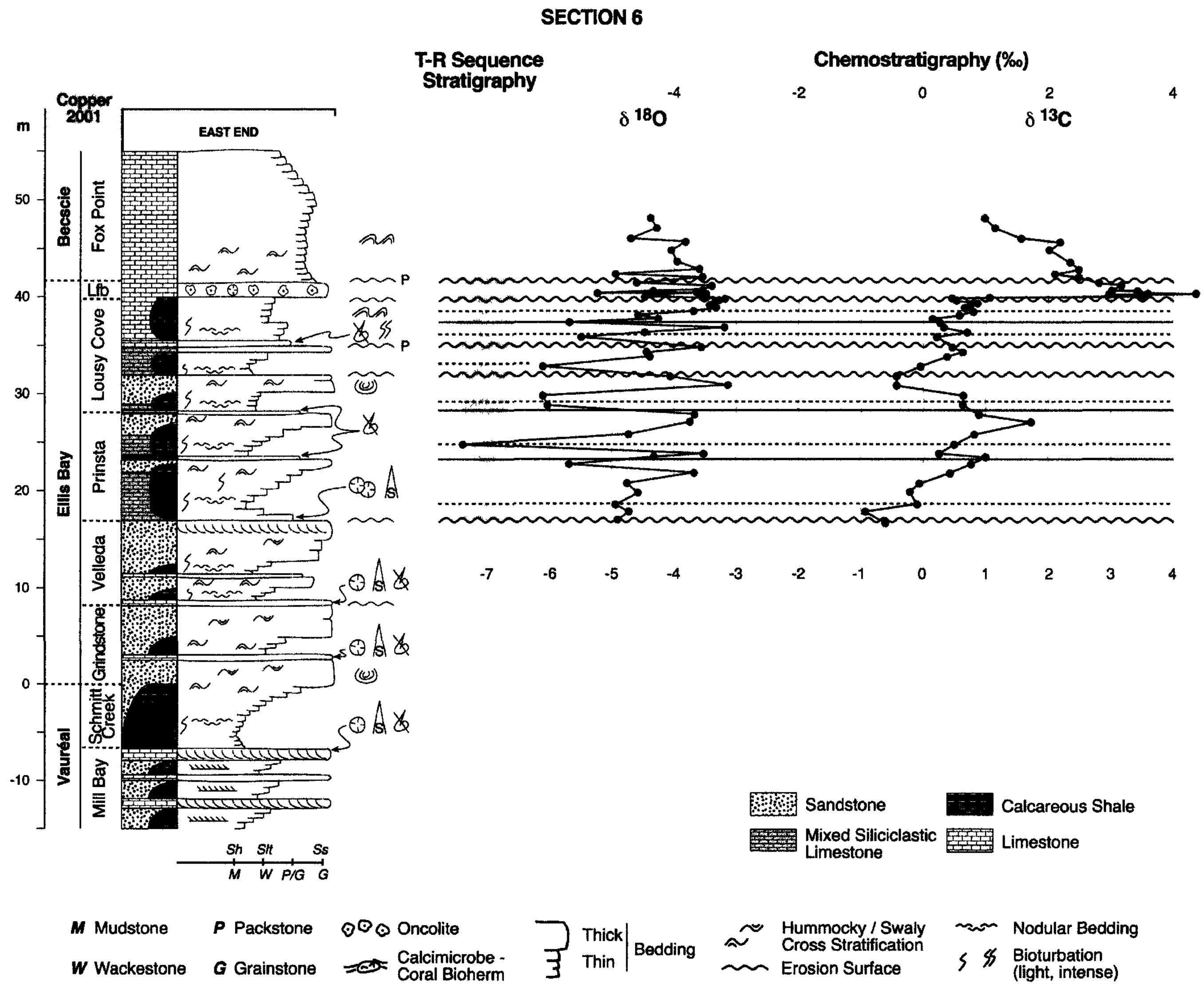

SECTION 6
T-R Sequence Stratigraphy
Chemostratigraphy (‰)
δ 18O
δ 13C
Copper 2001
m
EAST END
Becscie
Ellis Bay
Vauréal
Fox Point
Lfb
Lousy Cove
Prinsta
Velleda
Grindstone
Schmitt Creek
Mill Bay
Sh Slt Ss
M W P/G G
Sandstone
Calcareous Shale
Mixed Siliciclastic Limestone
Limestone
M Mudstone
W Wackestone
P Packstone
G Grainstone
Oncolite
Calcimicrobe - Coral Bioherm
Thick
Thin
Bedding
Hummocky / Swaly Cross Stratification
Erosion Surface
Nodular Bedding
Bioturbation (light, intense)

return to background values of between 0 and 1 ‰. A second $\delta^{13}C$ peak is present, which reaches 4 ‰ near the base of the Laframboise Member. A major offset is present between the $\delta^{13}C$ values just below the Laframboise to the peak values just above its base. Above the Ellis Bay, $\delta^{13}C$ values gradually return to a background of 0 to 1 ‰ in the lower Becscie Formation. The return to background values after the late Hirnantian $\delta^{13}C$ excursion appears higher above the base of the Becscie Formation at the east side of the island.

The $\delta^{18}O$ data from Lousy Cove is somewhat different than the data from the west end. Overall the values for $\delta^{18}O$ observed on the east end are lower, having a mean of -4.2 ‰ and a standard deviation of 0.7 ‰. One value at approximately 25 meters is below -7 ‰, which is at or near the same level as the anomalously low measurements of $\delta^{18}O$ seen in sections 4 and 5. The $\delta^{18}O$ data from section 6 also seems to have a very sporadic and oscillatory nature, which could be due to this section being thinner and containing at least five unconformities. It is also possible that the $\delta^{18}O$ measurements may have been more affected by diagenesis, as sediments at eastern sections could have been periodically exposed to the influence of isotopically lighter meteoric waters.

Discussion : Regional correlation

In summary, two positive $\delta^{13}C$ excursions are regionally present in all sections visited in this study. The first excursion generally peaks at a value close to 2 ‰ and the second one at approximately 4 ‰, with little variation in magnitude between localities. Where visible, the first $\delta^{13}C$ peak occurs immediately above the Vaureal-Ellis Bay contact in TR-1. The peak of the second $\delta^{13}C$ excursion always occurs within the Laframboise

Member (TR-5). Both of these $\delta^{13}C$ excursions can be traced across the Anticosti Basin from Section 1A at the west end to Section 6 at the east end (Figure 17). However, the difference in sedimentation between the western sections, 1A, 1B and 2, and the eastern sections, 3 to 6, is significant. In the four eastern sections, the two $\delta^{13}C$ excursions are separated by about 15 to 20 meters of strata. In section 2 the excursions are separated by approximately 65 meters and on the west end by close to 85 meters of strata.

In terms of $\delta^{18}O$, the values typically range between -2 and -5 ‰, although considerable variation exists between $\delta^{18}O$ values from different localities. Some sections appear to contain more enriched values near the top of the section, but this is mostly within the variation of the measurements as a whole. The more easterly sections produced some anomalously low values of $\delta^{18}O$, in the neighbourhood of -7 ‰. With this data in mind, it is possible that $\delta^{18}O_{carb}$ does not represent a genuine proxy for the state of the ocean, as it is sensitive to diagenetic alteration. For this reason, the rest of this report will focus solely on the analysis of $\delta^{13}C$ data for the O-S boundary and implications that can be drawn from it.

Global Correlation

Carbon isotope analysis has been performed on Hirnantian sections in many other areas of the world including Scotland, China, Nevada, Arctic Canada and Estonia (Figure 18). All of these sections, like Anticosti Island, record a positive $\delta^{13}C$ excursion in the mid to late Hirnantian, sometimes referred to as the Hirnantian Isotope Carbon Excursion (HICE) [8,35,67]. Some authors have claimed the HICE to be a globally synchronous signal and a useful correlative tool between sections [5]. However, due to

Figure 17. Correlation of $\delta^{13}C$ and $\delta^{18}O$ records across the Anticosti Basin. A datum is established at the base of the Laframboise Member (201.5 meters). Another time-correlation is shown representing the Vaureal-Ellis Bay contact, which records a chitinozoan turnover that is correlatable across the island supported by sequence stratigraphy [4].

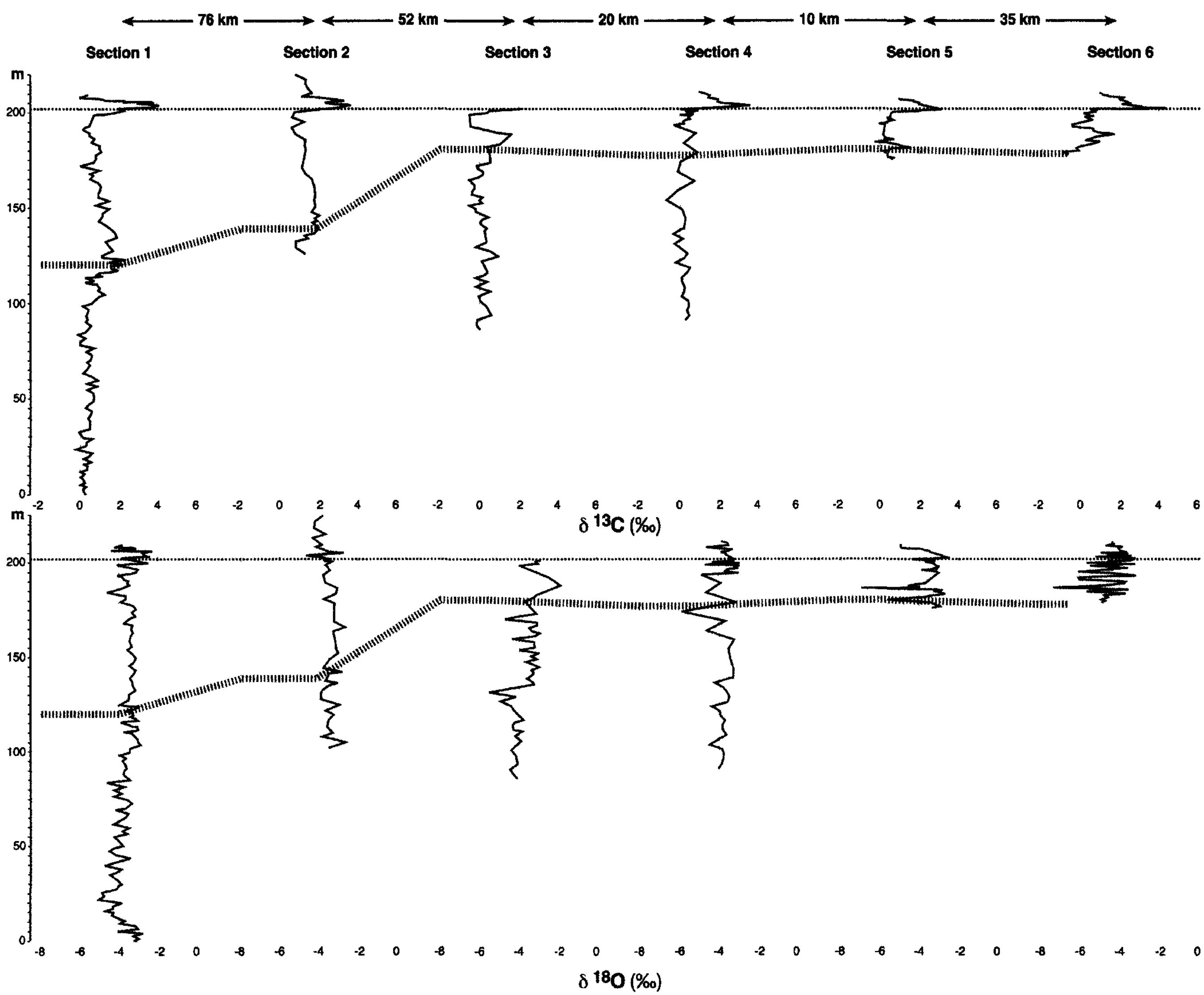

76 km
52 km
20 km
10 km
35 km
Section 1
Section 2
Section 3
Section 4
Section 5
Section 6
m
δ 13C (‰)
δ 18O (‰)

Figure 18. $\delta^{13}C$ data and biostratigraphy for various Hirnantian sections around the world [4]. The South China, Dob's Linn and Vinini Creek deep water sections are correlated by the graptolite biozones shown on the left. Shallow water sections at Anticosti Island (Section 2) and Estonia are correlated by the chitinozoan biozones displayed on the right. Vinini Creek contains abundant graptolites, conodonts and chitinozoans [68] and allows correlation between deep water and shallow water successions until halfway through the *N. persculptus* graptolite zone.

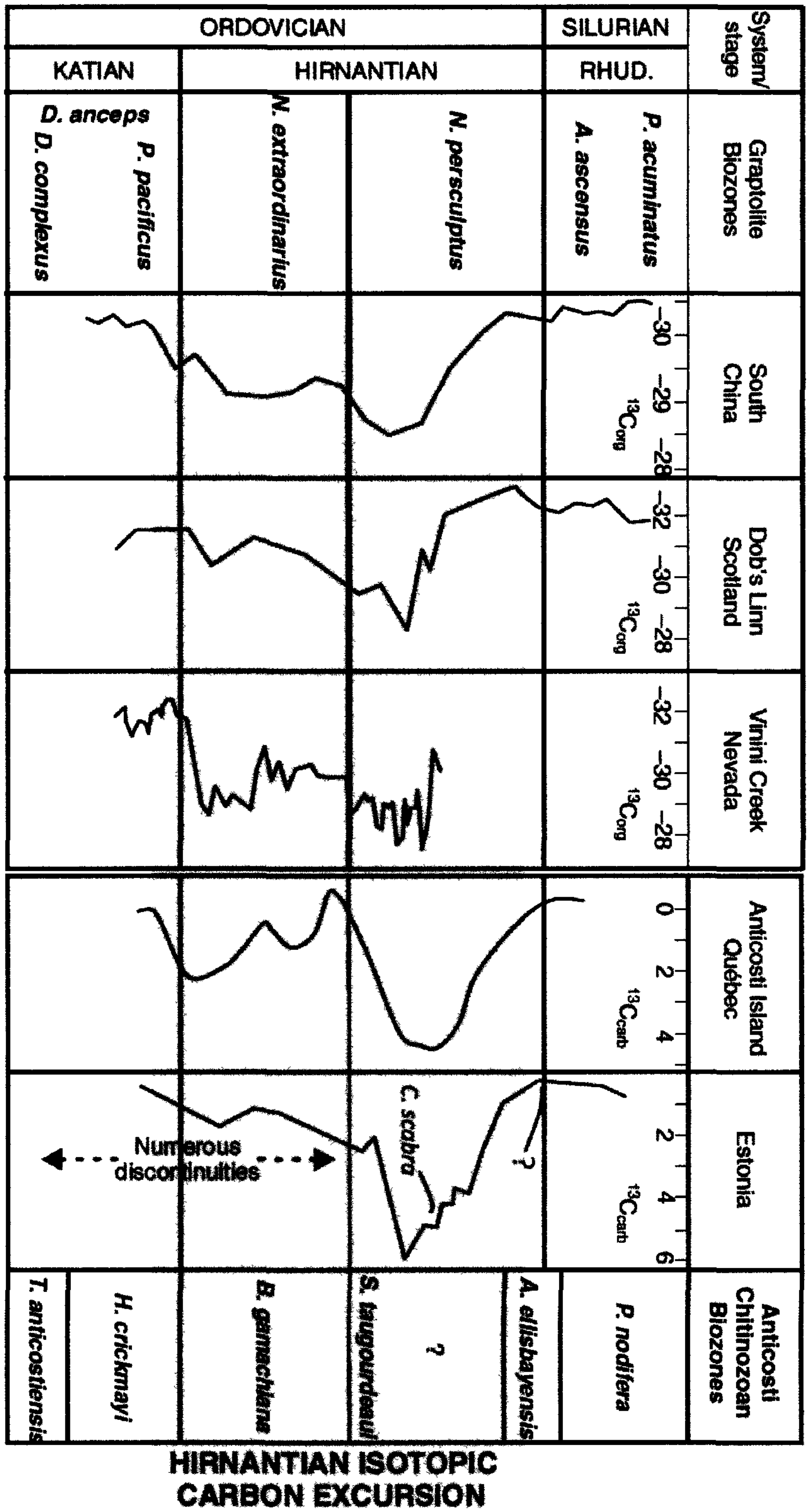

ORDOVICIAN
SILURIAN
System/ stage
KATIAN
HIRNANTIAN
RHUD.
Graptolite Biozones
D. anceps
D. complexus
P. pacificus
N. extraordinarius
N. persculptus
A. ascensus
P. acuminatus
South China
Dob's Linn Scotland
Vinini Creek Nevada
Anticosti Island Québec
Estonia
-30 -29 -28
-32 -30 -28
-32 -30 -28
0 2 4
2 4 6
13Corg
13Ccarb
C. scabra
?
Numerous discontinuities
Anticosti Chitinozoan Biozones
T. anticostiensis
H. crickmayi
B. gamachiana
S. taugourdeaui
?
A. ellisbayensis
P. nodifera
HIRNANTIAN ISOTOPIC CARBON EXCURSION

the limitations imposed by each region's biostratigraphic resolution, it is difficult to determine whether it truly represents a coeval signal in Hirnantian strata across the globe.

The GSSP for the O-S boundary is located at Dob's Linn in Scotland. This site contains about 75 meters of graptolite rich basinal shales ranging in age from the Caradoc to the Early Aeronian [67]. The sequence at Dob's Linn is tectonically complex and has been folded, faulted and metamorphosed to over 300°C [69]. Due to the fact that it represents only one facies (deep marine) and contains essentially one type of fossil (graptolites with rare chitinozoans), some authors have questioned its designation as the GSSP for the base of the Silurian [69]. Regardless of this, in 1997 Underwood and his colleagues carried out chemostratigraphic studies on the organic material at the Dob's Linn section (Figure 19). Here a large $\delta^{13}C_{org}$ excursion is observed in the *N.extraordinarius* graptolite biozone. The Hirnantian values for $\delta^{13}C_{org}$ are significantly above the earlier values, and by the Silurian, they returned to pre-Hirnantian levels. Despite the fact that the chemostratigraphy at Dob's Linn used organic carbon and our chemostratigraphic data was produced from micrite, it exhibits a remarkably similar $\delta^{13}C$ trend for the latest Ordovician and earliest Silurian strata of Anticosti Island (Figure 18).

Another graptolitic rich deep marine section for the O-S boundary exists on the Yangtze platform in Southern China. One particular locality in the Wangjiawan area now serves as the GSSP for the base of the Hirnantian, and was illustrated in 2006 by Chen et al. [38]. This section (Figure 20) comprises three formations, containing mostly black shales and cherts, and is considered to be relatively unaltered. There is one fossiliferous limestone layer in the Wangjiawan section, which is thought to represent a mid-Hirnantian lowstand. The whole section is highly condensed, as it contains roughly 10

Figure 19. $\delta^{13}C_{org}$ data for the O-S boundary section at Dob's Linn in Scotland [67]. Shaded areas indicate the occurrence of black shale. Non-shaded areas indicate the predominance of bioturbated mudstone. A large (~4 ‰) $\delta^{13}C_{org}$ excursion begins in the later part of the *N. extraordinarius* graptolite biozone (Band A) and ends in the terminal portion of *N. extraordinarius* (Band C). Since 1997, graptolite biostratigraphy at Dob's Linn has been revisited by Melchin and Williams [70] and Melchin et al. [71], where *N. persculptus* was described occurring 1.6 meters below the base of the *N. persculptus* biozone defined in [67]. This places the peak of the $\delta^{13}C$ excursion within the *N. persculptus* biozone [72], contemporary with the Laframboise Member on Anticosti Island [4].

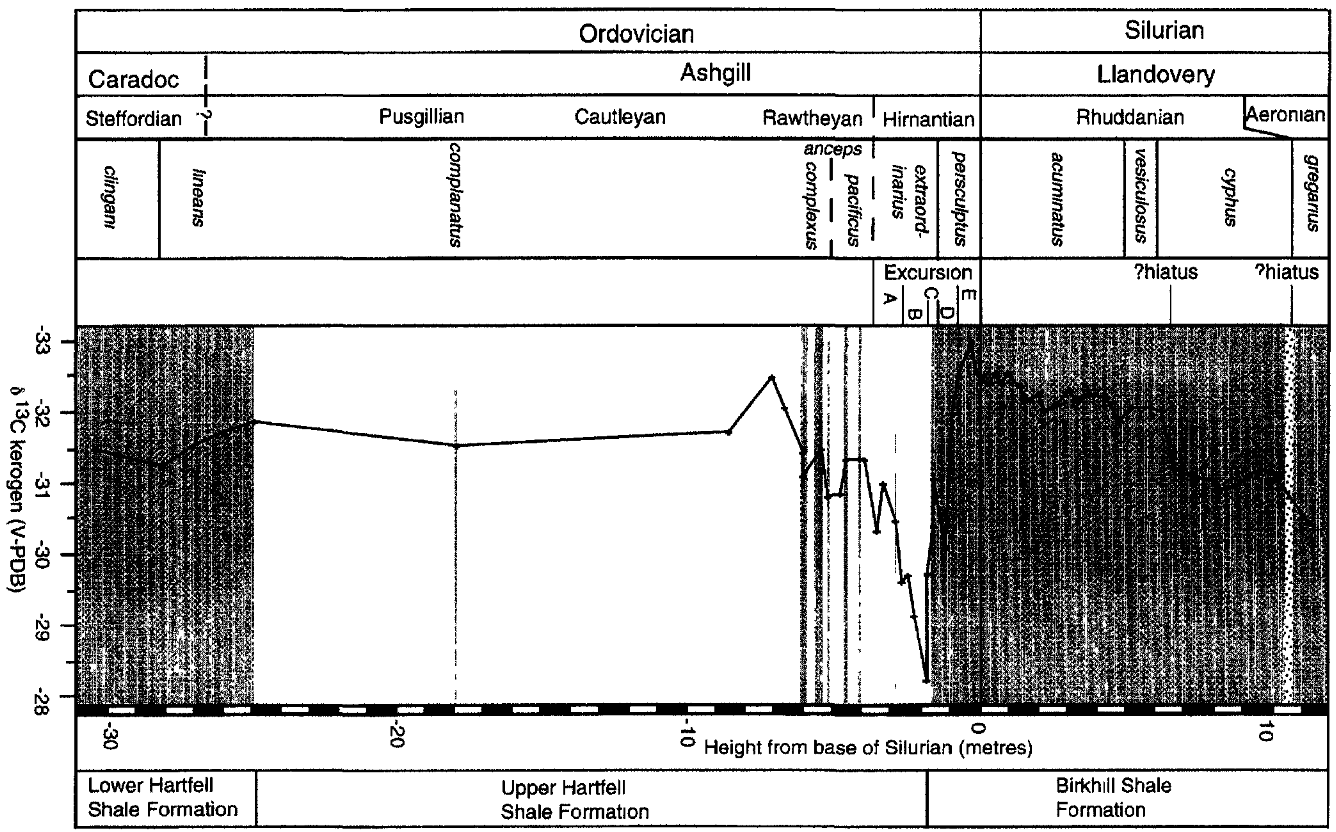

Ordovician
Silurian
Caradoc
Ashgill
Llandovery
Steffordian
?
Pusgillian
Cautleyan
Rawtheyan
Hirnantian
Rhuddanian
Aeronian
clingani
lineans
complanatus
anceps
complexus
pacificus
extraord-inarius
persculptus
acuminatus
vesiculosus
cyphus
gregarius
Excursion
A
B
C
D
E
?hiatus
?hiatus
δ 13C kerogen (V-PDB)
-33
-32
-31
-30
-29
-28
-30
-20
-10
0
10
Height from base of Silurian (metres)
Lower Hartfell Shale Formation
Upper Hartfell Shale Formation
Birkhill Shale Formation

Figure 20. $\delta^{13}C_{org}$ data for the Wangjiawan section in China [73]. Radiometric dates [74] define the Hirnantian between 445.6 Ma and 443.7 Ma. The large $\delta^{13}C_{org}$ excursion occurs just above the base of the *N. persculptus* zone.

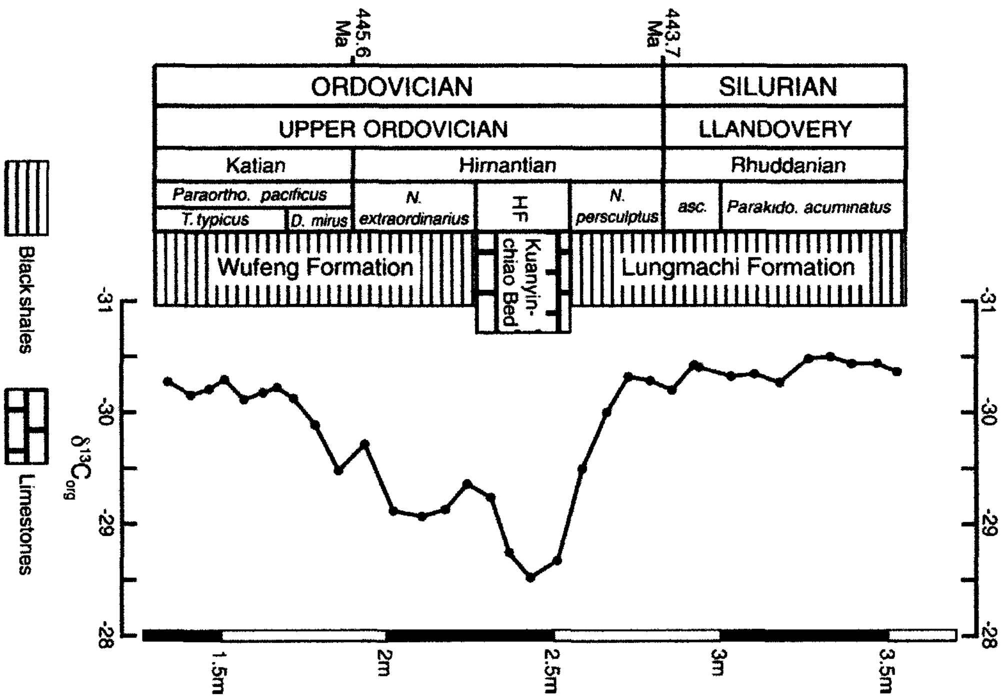
445.6 Ma
443.7 Ma
ORDOVICIAN
SILURIAN
UPPER ORDOVICIAN
LLANDOVERY
Katian
Hirnantian
Rhuddanian
Paraortho. pacificus
T. typicus
D. mirus
N. extraordinarius
HF
N. persculptus
asc.
Parakido. acuminatus
Wufeng Formation
Kuanyin-chiao Bed
Lungmachi Formation
Black shales
Limestones
$\delta^{13}C_{org}$
-31
-30
-29
-28
1.5m
2m
2.5m
3m
3.5m

million years of sedimentation from the Katian to the Rhuddanian squeezed into less than 3 meters of strata. Like the Dob's Linn section, analysis of $\delta^{13}C_{org}$ was carried out on the Wangjiawan shales. A $\delta^{13}C_{org}$ excursion begins in the *Paraorthograptus paciticus* graptolite zone and reaches a peak near the base of the *N. extraordinarius* zone, approximately 1 ‰ higher than earlier background values. Another $\delta^{13}C_{org}$ excursion of slightly greater magnitude peaks near the end of the *N. extraordinarius* zone. This is followed by a larger excursion in the *N. persculptus* biozone, peaking at approximately 2 ‰ above background. The trends in the $\delta^{13}C_{org}$ record in China bear resemblance to the $\delta^{13}C$ curves observed in the Anticosti sections (Figure 18).

Stable isotope analysis was also performed on a few O-S boundary sections in Nevada. A 2009 publication by Laporte et al. [75] describes data from a few sections in Nevada, including one section at Vinini Creek that contains approximately 30 meters of strata ranging from the Katian to the Hirnantian (Figure 21). Another more extensive outer shelf section in Nevada, Copenhagen Canyon, has also been sampled for geochemical proxies (Figure 22) starting with the work of Kump et al. [10]. Both of these sections are comprised of marine deposits from platform to basin facies, containing biostratigraphic data from graptolites, conodonts and chitinozoans. At Vinini Creek, a $\delta^{13}C$ excursion is present beginning at the base of the *N. extraordinarius* zone, reaching values of 2 ‰ above the pre-Hirnantian background in both organic carbon and bulk carbonate samples. A second larger $\delta^{13}C$ peak is observed in the *N. persculptus* zone, reaching values of 3 ‰ for $\delta^{13}C_{org}$ and values of 4 ‰ for $\delta^{13}C_{carb}$ above the pre-Hirnantian background, comparable to the Ellis Bay Formation on Anticosti Island (Figure 18). The main peaks of $\delta^{13}C_{org}$ and $\delta^{13}C_{carb}$ appear at slightly different positions.

Figure 21. $\delta^{13}C_{org}$ and $\delta^{13}C_{carb}$ data for the Vinini Creek site in Nevada [75]. Maximum $\delta^{13}C_{carb}$ values are observed just above the base of the *N. persculptus* zone.

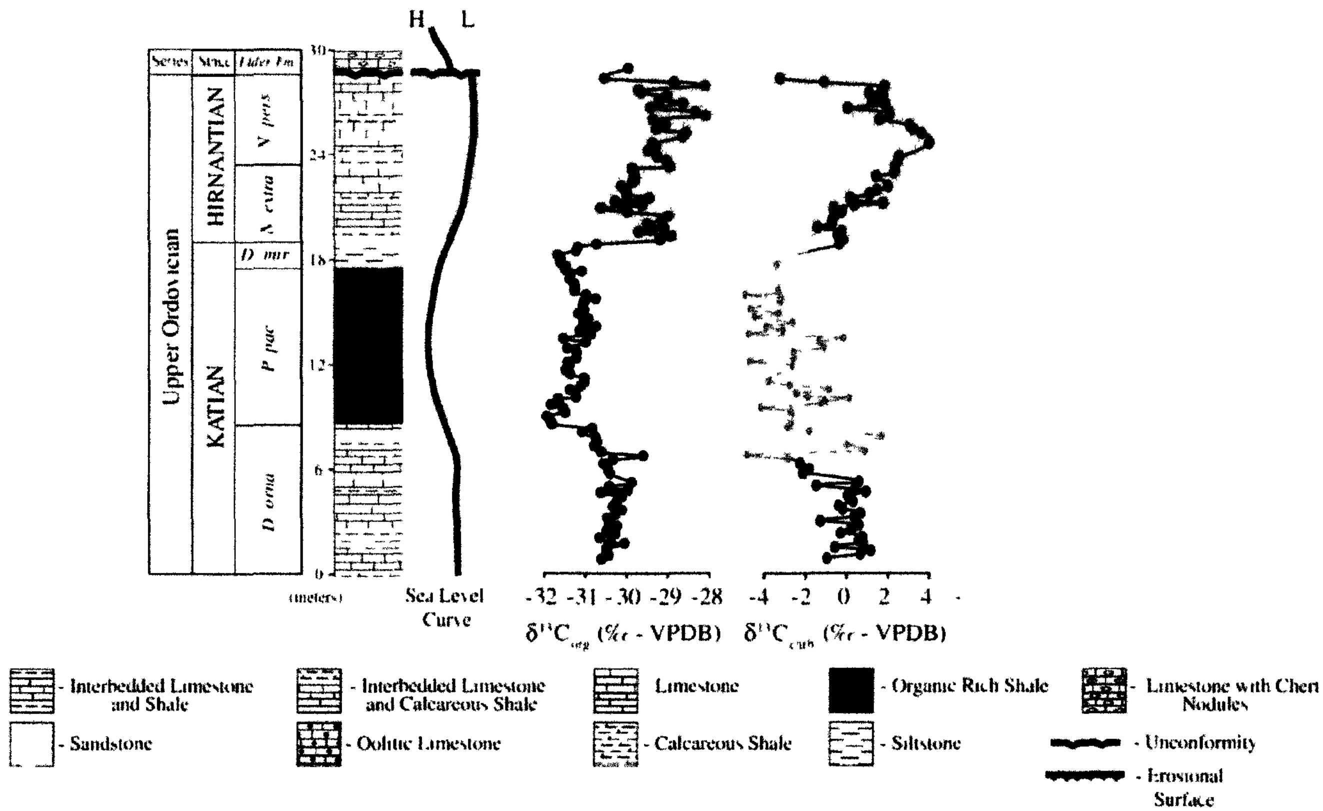
H
L
Series
Stage
Lithology / Fm
Upper Ordovician
HIRNANTIAN
KATIAN
N. pers
N. extra
D. mir
P. pac
D. orna
30
24
18
12
6
0
(meters)
Sea Level Curve
-32 -31 -30 -29 -28
$\delta^{13}C_{org}$ (‰ - VPDB)
-4 -2 0 2 4
$\delta^{13}C_{carb}$ (‰ - VPDB)
- Interbedded Limestone and Shale
- Interbedded Limestone and Calcareous Shale
Limestone
- Organic Rich Shale
- Limestone with Chert Nodules
- Sandstone
- Oolitic Limestone
- Calcareous Shale
- Siltstone
- Unconformity
- Erosional Surface

Figure 22. $\delta^{13}C$ and $\delta^{18}O$ data for the Copenhagen Canyon site in Nevada [10]. The interval between 35 and 78 m does not contain biostratigraphically diagnostic fauna, but based on correlations with adjacent areas it is thought to be contemporary with conodont zone 13 [76]. This suggests a beginning for the $\delta^{13}C$ excursion near the base of the *N. extraordinarius* zone, and a return to background values above or at the base of *N. persculptus* zone.

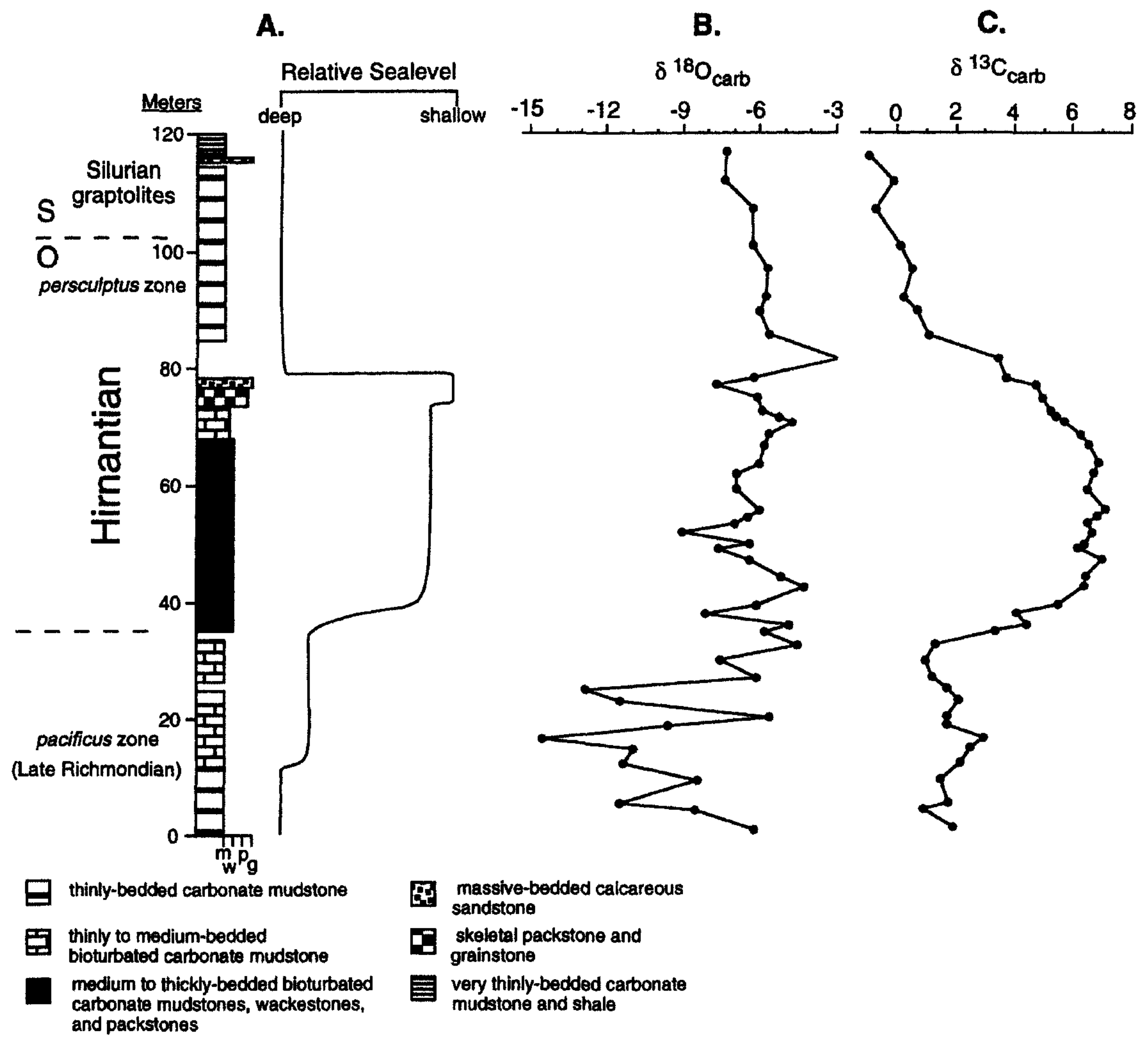
A.
B.
C.
Relative Sealevel
deep
shallow
δ 18O carb
δ 13C carb
-15 -12 -9 -6 -3
0 2 4 6 8
Meters
120
100
80
60
40
20
0
Silurian graptolites
S
O
persculptus zone
Hirnantian
pacificus zone
(Late Richmondian)
m w p g
thinly-bedded carbonate mudstone
thinly to medium-bedded bioturbated carbonate mudstone
medium to thickly-bedded bioturbated carbonate mudstones, wackestones, and packstones
massive-bedded calcareous sandstone
skeletal packstone and grainstone
very thinly-bedded carbonate mudstone and shale

The Vinini Creek section ends with an unconformity in the *N. persculptus* zone, immediately following a sharp return to background values. At the Copenhagen Canyon site, a single broad $\delta^{13}C$ excursion peaks at 7 ‰ above the pre-Hirnantian background. It is difficult to describe the excursion at this site in detail as it is poorly constained by biostratigraphy.

In 2006, Melchin and Holmden [8] performed carbon isotope analysis on three sections around Cornwallis Island in the Canadian Arctic Islands. These sections represent a distal ramp environment within an embayment of the early Palaeozoic Franklinian Basin. The Hirnantian sediments are condensed into less than 5 meters of strata and are composed of a mix of graptolitic shales, micritic limestones and dolostones. For these sediments (Figure 23), $\delta^{13}C_{org}$ is considered more reliable than the inorganic carbon, as the sediments have been significantly dolomitized. As in other O-S boundary sections, a positive $\delta^{13}C_{org}$ excursion is observed, beginning before the *N. extraordinarius* zone and ending early in the *N. persculptus* zone. The excursion is also divided into two peaks, with considerable variation in magnitude and shape between sites. This locality is anomalous among O-S boundary sections as the $\delta^{13}C_{org}$ peak in the *N. extraordinarius* zone reaches higher values than the peak in the *N. persculptus* zone. Also peculiar is how the later peak occurs well before the O-S boundary. It may be possible that part of the $\delta^{13}C_{org}$ signature is missing in the Cornwallis Island sections, although no unconformities are reported from the more distal sections.

Chemostratigraphic profiles have been produced for shallow water limestone at O-S boundary sections in Estonia [35]. These sections are marked with different regional stage names. The Pirgu stage is approximately equivalent with the Katian stage and the

Figure 23. $\delta^{13}C_{org}$ data for Cornwallis Island in Arctic Canada [8].

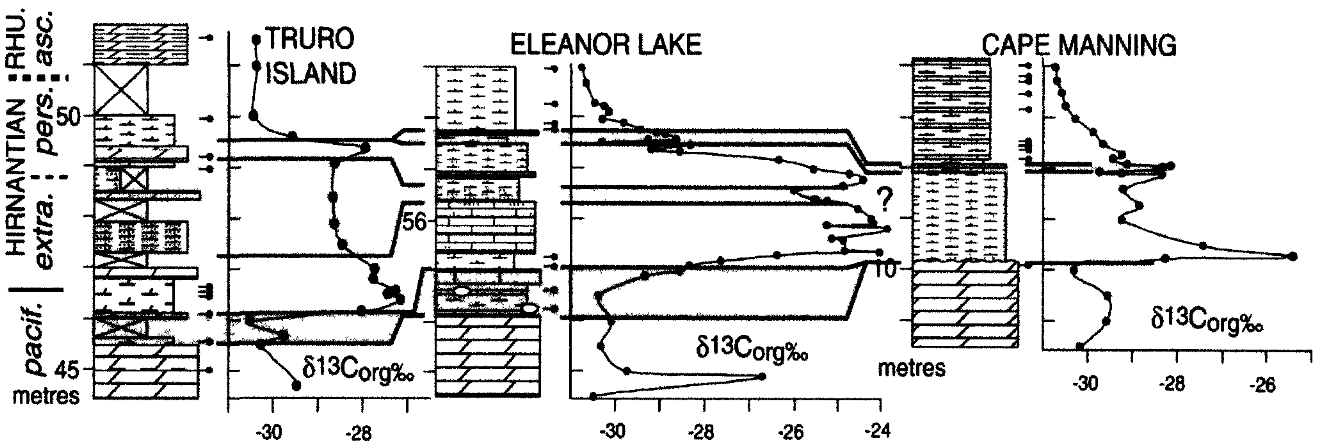

TRURO ISLAND
ELEANOR LAKE
CAPE MANNING
HIRNANTIAN
RHU.
pacif.
extra.
pers.
asc.
50
45
metres
56
10
metres
?
δ13Corg‰
δ13Corg‰
δ13Corg‰
-30
-28
-30
-28
-26
-24
-30
-28
-26

overlying Porkuni closely parallels the Hirnantian stage. This is followed by the Juuru stage that represents the earliest Silurian. Carbon isotope analysis was performed on one of these stratigraphic sections from a drill core at Ruhnu (Figure 24). Here we see a $\delta^{13}C$ excursion peaking at a value above 5 ‰ in the Porkuni, followed by a decline in values to about 1 ‰ after the Porkuni-Juuru contact, where they appear relatively stable. The Estonian sections are the most similar in appearance to the O-S boundary strata on Anticosti as they both represent shallow water environments and contain similar faunas and facies. However, only one $\delta^{13}C$ peak is observed in the Ruhnu section, rather than the two peaks observed in the Ellis Bay Formation. This may be because the Estonian sections contain several unconformities at or near the Porkuni-Pirgu stage boundary that make correlations between these sections and the rest of the O-S boundary sections in the world difficult.

All of these O-S boundary sections from across the world display at least one major positive $\delta^{13}C$ excursion, obtaining values of at least 4 ‰ above background, or 2 ‰ in the case of organic carbon, in the early part of the *N. persculptus* biozone where well-constrained biostratigraphy exists. Hirnantian sites occur on different paleocontinents and different paleobasins, and represent a range of environments from shallow water carbonate platform to deep basin. However, they are limited in paleolatitude to the tropics. The southernmost of these sections in Nevada exhibits higher $\delta^{13}C$ values for the excursion, although there is no clear trend indicating that the magnitude of the excursion is related to latitude. There also appears to be little dependence on water depth or facies to the magnitude of the excursion. It is not entirely clear whether the late Hirnantian positive $\delta^{13}C$ excursion observed on Anticosti Island

Figure 24. $\delta^{13}C$ and $\delta^{18}O$ isotope data for the Ruhnu section in Estonia [5]. Circles represent whole rock carbonates (micrite) and squares represent shells of brachiopods. The horizontal line at 601 meters denotes the O-S boundary. The dividing line at 619.1 meters is the Pirgu-Porkuni contact, which represents a significant unconformity. The Porkuni approximately represents the later part of the Hirnantian, based on chitinozoan biostratigraphy [4]. Note that $\delta^{13}C$ values in brachiopods are up to 2 ‰ higher than bulk carbonates in the Porkuni. In contrast, $\delta^{13}C$ values in brachiopods appear uniformly lower than $\delta^{13}C$ values in bulk carbonates in the Juuru.

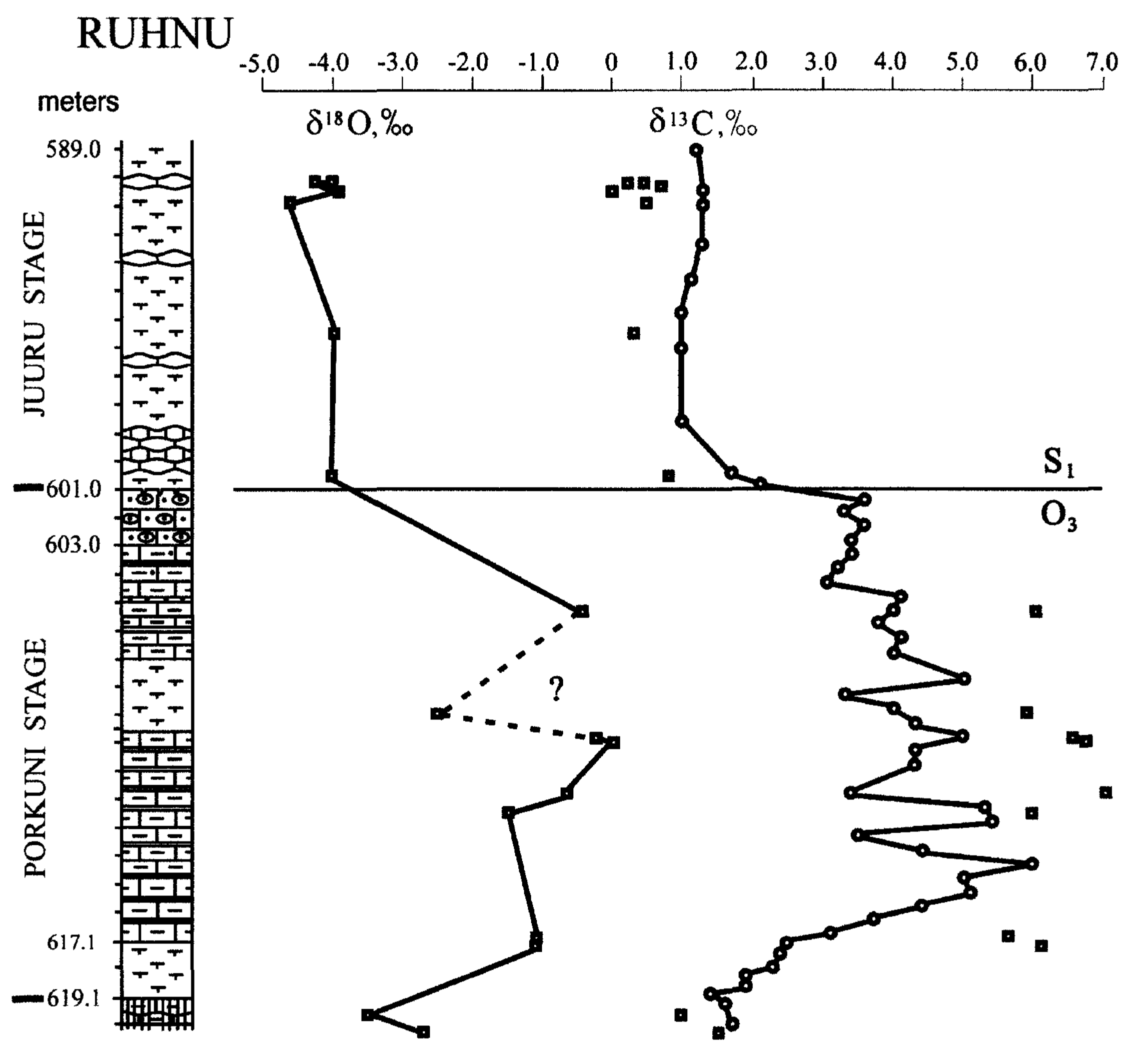
RUHNU
meters
589.0
601.0
603.0
617.1
619.1
JUURU STAGE
PORKUNI STAGE
-5.0
-4.0
-3.0
-2.0
-1.0
0
1.0
2.0
3.0
4.0
5.0
6.0
7.0
δ18O,‰
δ13C,‰
S1
O3
?

represents a coeval signature across the world, as the constraints imposed by graptolite and chitinozoan biostratigraphy do not allow correlation beyond the level of the *N. persculptus* biozone, which represents roughly half of the Hirnantian. If the HICE represents a global signal, it probably represent a major perturbation of the Late Ordovician global carbon cycle, the possible causes of which will explored in the next section. However, because $\delta^{13}C$ values are also prone to spatial variability, especially within restricted platforms and epeiric seas [77,78] it is possible that the $\delta^{13}C$ excursions observed in Hirnantian sections around the world are not entirely coeval and merely represent an asynchronous creation of restricted basins in different parts of the Hirnantian world.

Explanations for the HICE

The large positive shifts in carbon isotope values observed in Hirnantian sections are usually believed to represent major perturbations in the global carbon cycle [9,41]. Authors frequently attempt to explain these events through describing the changing distribution of light and heavy isotopes of carbon in the different global reservoirs of carbon: the atmosphere, the deep ocean, shallow water, carbonate rocks and organic matter. A favoured method of describing such changes is to use a box model for the global carbon cycle, like the one found in Appendix A. Box models are applicable for quantitatively testing the predictions of hypotheses attempting to explain the shifts in $\delta^{13}C$ that occurred at the O-S boundary.

Assuming that the HICE represents a truly global and coeval signal, there are three main types of theories that attempt to explain it in the context of the biotic and climatic events that occurred during the Hirnantian. The first to be proposed was the productivity hypothesis of Brenchley et al. [9]. In this hypothesis, productivity among marine phytoplankton increased due to a change in ocean circulation, leading to an increase in $\delta^{13}C$ values. This hypothesis states that high primary productivity also led to a drawdown of atmospheric CO_2, initiating the Hirnantian glaciation and eustatic drop. In contrast to this, Kump et al. [41] proposed the weathering hypothesis. In this hypothesis, the $\delta^{13}C$ excursions of the Hirnantian were the result of weathering of carbonate platforms that became exposed. A third hypothesis, involving a change in state of the ocean, was proposed in 2005 by Cramer and Saltzmann [50]. This hypothesis describes an episode of enhanced sequestration of isotopically light carbon during marine transgressions and highstands. Each of these hypotheses will be examined and discussed in detail in the following paragraphs.

The original productivity hypothesis proposed by Brenchley et al. involves a sequence of events. The first step is a change from a density-stratified ocean in the Katian stage to one with active thermohaline circulation in the Hirnantian, due to the movement of the Gondwana supercontinent toward the South Pole. The resulting downwelling of cold, polar currents [79], initiated thermohaline circulation in the oceans that led to upwelling at lower latitudes, and enhanced nutrient and toxin fluxes to the surface of the oceans. This stimulated oceanic primary productivity, generated widespread anoxia and extinction amongst the oligotrophic ecosystems that existed in the Late Ordovician. Eventually, the increase in productivity may have led to major perturbations in the carbon cycle, as measured in the stable isotope record of oceanic carbon, and subsequently to a decrease in atmospheric CO_2. The Hirnantian glaciation and eustatic drop are believed to have occurred primarily because of this hypothetical drawdown of CO_2, and therefore are predicted by this hypothesis to have occurred after the onset of the $\delta^{13}C$ excursion in the isotope record.

One of the predictions of the productivity hypothesis is that an increase in the production of organic matter during the TR-5 transgression would have led to a deposition of organic-rich black shale layers that were responsible for sequestration of the light carbon isotope from the global ocean. Deposition of black shales is known from various oceanic anoxic events, such as in Jurassic and Cretaceous strata [80], but as the first observation, Hirnantian sediments are quite low in organic carbon [8]. In the sections studied on Anticosti Island black shale was completely absent, including the strata around the O-S boundary. Considering black shale is usually found in basinal facies rather than in shallow water facies, such as those on Anticosti Island, it may be postulated that the black shales were deposited elsewhere and subsequently lost, either due to subduction or erosion. Note that the latest Hirnantian strata of Anticosti Island contain at least two unconformities. To generate a 4 ‰ excursion in oceanic $\delta^{13}C$, the rate of organic carbon burial would have to increase by 15 times the modern equivalent (Appendix A). This is not a realistic proposition, but the fluxes could be more easily explained if the scenario were applied to localized basins within the Hirnantian that may not have been strictly coeval.

A popular alternative to the above scenario is the weathering hypothesis proposed by Kump et al. and modified by Melchin and Holmden [8] and others [11,81]. Most versions of this hypothesis relate the Hirnantian glaciation to a drawdown in atmospheric CO_2 that was initiated by an increase in silicate weathering. The Ordovician period was a time of active sea floor spreading and mountain building. This is thought to have contributed to an increase in silicate weathering, particularly in the case of the Taconic Orogeny [22]. A drawdown of atmospheric CO_2 then initiated continental glaciation on Gondwana and a sea level drop of up to 100 meters. This led to drainage and exposure of the epeiric seas and hence, to erosion of most of the world's carbonate platforms. Kump et al. believe it was this erosion of heavy carbon stored in carbonates that led to an increase in $\delta^{13}C$ in the ocean during the Hirnantian. Once a significant portion of the southern continent was covered in ice, the amount of silicate weathering declined, and eventually atmospheric CO_2 levels increased and global temperatures rose again. This explains the relatively short duration of the Hirnantian glaciation. In contrast to Brenchley et al., the weathering hypothesis suggests that the glaciation and sea level drop occurred before the onset of the main $\delta^{13}C$ excursion.

In contrast to Brenchley et al., the Kump et al. hypothesis does not predict the occurrence of black shale, but rather extensive weathering of carbonates, for which there is much evidence for in numerous unconformities that exist in the Ellis Bay Formation. With regards to the timing of events in the Hirnantian stage, the high-resolution $\delta^{13}C$ data presented in this study suggests that the sea level fell as a result of the Hirnantian glaciation, near the onset of the major 4 ‰ carbon isotope excursion. This is easily observed in Figure 10, as the main $\delta^{13}C$ excursion occurs during the lowstand containing the two unconformities on the west end of Anticosti Island. In this respect, our data is consistent with the ideas proposed by Brenchley et al. and Kump et al., as they both predict that the main $\delta^{13}C$ excursion should be closely associated with a rapid and significant drop in global sea level.

However, the weathering hypothesis proposed by Kump et al. is problematic because on Anticosti Island the sediments underlying the main $\delta^{13}C$ excursion are uniformly at background values of approximately 0 to 1 ‰. Carbonates from around the world of Early Ordovician and Cambrian age have similar values [44]. The Anticosti Basin represents a shallow water carbonate shelf residing in a foreland basin near the margin of the Late Ordovician epeiric sea of Laurentia. Erosion of these exposed carbonates could not have raised the $\delta^{13}C$ to 4 ‰. In fact, $\delta^{13}C$ values in carbonate rock very rarely exceed values of 3 ‰ for most of the geological record [45]. Sediments in carbonate platforms also contain organic matter, which tends to lower the overall $\delta^{13}C$ values of the weathering flux closer to -5 ‰. In summary, the weathering hypothesis fails to explain the magnitude of the Late Hirnantian carbon isotope excursion.

More recently, Cramer and Saltzmann proposed a hypothesis involving changes in the state of the ocean to explain the $\delta^{13}C$ excursion that occurred at the end of the Hirnantian, and several times in the Silurian period [82]. A central theme of this theory is the transition from clear seas where deep ocean upwelling is common, to turbid seas where estuarine circulation dominates. Jeppsson and Calner [83] and Munnecke et al. [84] propose two states for early Palaeozoic systems, with abrupt transitions between P states (arid) and S states (wet) resulting in faunal turnovers, particularly among conodonts. Changes in climate and sea level act as a driver for these transitions. Switching circulation from upwelling to downwelling is proposed to affect surface $\delta^{13}C$ values because it affects the $\delta^{13}C$ gradient from shallow to deep water. This is because increased photosynthetic activity in the surface layers of the ocean enhances $\delta^{13}C$ in shallow water relative to deeper waters where oxidation of organic matter lowers $\delta^{13}C$

values. Oceanic upwelling allows some of the water with lower values of $\delta^{13}C$ to return to the surface, whereas estuarine circulation and downwelling prevents this exchange. Cramer and Saltzmann indicate that the downwelling state occurs during lowstand and gradually switches to upwelling at mid–transgression. Highstand and anti-estuarine circulation also provide clearer water that enhances production by carbonate factories, hence increasing the $\delta^{13}C$ gradient. Note that this hypothesis can be applicable to both global and regional (basinal) scales.

The Cramer and Saltzmann hypothesis, similar to Brenchley et al., cannot account for the lack of black shales at or near the large $\delta^{13}C$ excursion at the O-S boundary. It also predicts an increase in shallow water $\delta^{13}C$ values during early highstand due to diminution of the light carbon flux from the deep ocean because of the commencement of estuarine circulation [82]. This suggests a possible correlation between the highstand phases of TR cycles and local maximums in the $\delta^{13}C$ record. The most complete record of TR cycles in the Ellis Bay Formation comes from Section 1A (Figure 10), which indicates no correlation.

Overall, none of the hypotheses outlined can explain all of the observations regarding stable isotopes preserved in Hirnantian sediments and the timing of events at the O-S boundary. All three groups of theories have difficulty explaining the magnitude and positive nature of the late Hirnantian $\delta^{13}C$ excursion. Many of the basic observations expected from these hypotheses, such as the occurrence organic-rich shale beds and increased values of $\delta^{13}C$ for shallow water, are apparently absent in the Ellis Bay Formation. However, if viewed as being a regional event within the Anticosti Basin, the Cramer and Saltzmann hypothesis appears plausible. According to the global carbon cycle model in Appendix A, a $\delta^{13}C$ excursion of 4 ‰ is possible on a regional scale if exchanges with the open ocean become restricted, and upwelling of light carbon from the deep ocean is prevented. However, on a global scale it is not likely that changes in ocean state, replacing anti-estuarine circulation with estuarine circulation would occur in synchronicity across the globe. For this reason, if the HICE represents a global event, it is not likely that the Cramer and Saltzmann hypothesis can explain the HICE. See Appendix A for further discussion.

Asynchronicity among HICE peaks

Although the Hirantian carbon isotope excursions present in the Ellis Bay Formation represent changes in $\delta^{13}C$ values that occurred across a shallow water carbonate ramp, it is not entirely clear whether these signals indicate a global change in oceanic $\delta^{13}C$ or if the changes were regionally confined to within the Anticosti Basin. Most Hirnantian $\delta^{13}C$ records from elsewhere contain excursions with similar magnitudes to Anticosti Island, but some such as Copenhagen Canyon, Eleanor Lake and Ruhnu display higher values and a broader plateau-like shape. Perhaps it is possible that elements of the $\delta^{13}C$ record at these sites are regional signals superimposed on an underlying global signal for the Hirnantian. This could explain some of the variation from basin to basin, but considering the fact that Copenhagen Canyon, which displays the highest $\delta^{13}C$ values, represents an outer shelf environment, it is not justifiable.

Since the duration of the late Hirnantian excursion on Anticosti is estimated between 0.1 and 0.5 Ma compared to approximately 1 Ma for the duration of the *N. persculptus* zone, it is possible that the $\delta^{13}C$ changes observed in different basins occurred at different times in the Hirnantian. This is conceivable considering the decline in sea level that occurred during the Hirnantian glaciation could have led to many pericontinental shelves being restricted from the open ocean, but not in synchronicity. This scenario would mean that the HICE doesn't necessarily represent a global and correlatable signal, but independent, asynchronous events occurring in different regions as a response to changes in climate.

The HICE as a stratigraphic tool

Brenchley et al. [5] defined the HICE observed in Estonia as a chronostratigraphic "ruler" that could be utilized for high-resolution correlations between different sites in Estonia, and for global correlations. This was proposed on the basis of patterns observed between chitinozoan biozones and the shape of $\delta^{13}C$ profiles for a set of cores in Estonia. The results of the current study on Anticosti Island also suggest that correlations using carbon isotopes are possible within a basin, particularly with the support of high-resolution biostratigraphy and sequence stratigraphy. Using the HICE as a correlative tool on a global scale may also be possible, although with a lower resolution. Since most Hirnantian sections around the world contain at least one positive $\delta^{13}C$ excursion that stands out against the background, the Hirnantian may represent a period of time that favoured the development of many, but not necessarily coeval, $\delta^{13}C$-enriched basins. In this case it may be possible for the HICE to identify correlations between Ordovician and Silurian strata within the *N. persculptus* biozone.

Conclusion

In the course of the present study, six Upper Ordovician sections on Anticosti Island, representing a low paleolatitude, shallow water carbonate ramp succession were examined and analyzed for isotope study and integrated within a framework of biostratigraphy and sequence stratigraphy for the Ellis Bay Formation. Fine-grained micrite was collected from these sections and stable isotope composition of carbon and oxygen was measured. A series of high-resolution isotope profiles from proximal inner ramp to distal basin margin environments, spanning the O-S boundary, was produced. In all of the isotope profiles two prominent positive $\delta^{13}C$ excursions were observed, one reaching 2 ‰ near the Vaureal-Ellis Bay formation contact and the other peaking at approximately 4 ‰ within the Laframboise Member of the Ellis Bay Formation. Within the constraints of the present stratigraphic resolution, these changes in the carbon isotope ratio can be correlated across the Anticosti Basin. The $\delta^{13}C$ records obtained from the Ellis Bay Formation appear similar to a number of other $\delta^{13}C$ records of Hirnantian sections from around the world.

This study was successful in further refining the framework for the timing of environmental and biotic events of the O-S boundary. The onset of the 4 ‰ $\delta^{13}C$ excursion closely parallels the late Hirnantian regression and the following return to background values matches with the post-glacial transgression in all the sites studied in the upper Ellis Bay Formation. The data obtained in this study supports the notion that the large-scale changes in sea level and $\delta^{13}C$ at the end Ordovician occurred in parallel, and were perhaps interdependent. This study was not able to demonstrate whether the early and late Hirnantian $\delta^{13}C$ excursions coincided closely with the faunal turnovers that occurred during the Hirnantian, but it is suspected. Three hypotheses proposing explanations for the events at the O-S boundary were reviewed in the context of the high-resolution carbon isotope data obtained in this study, but it was found that many of their predictions were not confirmed for the Anticosti Basin.

The resolution of the $\delta^{13}C$ record across the O-S boundary on Anticosti Island was improved dramatically in this study. However, two of the sections, Vaureal River and Natiscotec River, were sampled more sparsely due to logistical concerns and future study could be conducted on them to enhance their resolution. Another area of possible future study would be to re-examine the $\delta^{18}O$ signatures around the O-S boundary on Anticosti Island using alternative proxies such as brachiopod and conodont fossils. Although, $\delta^{18}O_{carb}$ is often believed to be altered and not show an accurate representation of the ancient ocean, the $\delta^{18}O_{carb}$ observed in eastern sections (Figure 20) in our study may in fact be a resolvable signal. This is of interest because depleted values of $\delta^{18}O$ in sections 4,5 and 6 seem to occur in conjunction with maximum flooding surfaces, in direct contradiction with the notion that depleted $\delta^{18}O$ values should represent periods of meteoric influence during times of subaerial exposure.

References

[1] Ghienne, J.F., 2002. Late Ordovician sedimentary environments, glacial cycles, and post-glacial transgression in the Taoudeni Basin, West Africa. Palaeogeography, Palaeoclimatology, Palaeoecology, v.189(3-4), p.117-145.

[2] Sheehan, P.M., 2001. The Late Ordovician Mass Extinction. Annual Review of Earth and Planetary Sciences, v.29, p.331-364.

[3] Desrochers, A., Farley, C., Achab, A., Asselin, E., Riva, J.F., 2010. A far-field record of the end Ordovician glaciation: The Ellis Bay Formation, Anticosti Island, Eastern Canada. Paleogeography, Paleoclimatology, Paleoecology, In press.

[4] Achab, A., Asselinm E., Desrochers, A., Riva, J.F., Farley, C., 2010. Chitinozoan Biostratigraphy of a new Upper Ordovician Stratigraphic Framework for Anticosti Island, Canada. GSA Bulletin, In press.

[5] Brenchley, P.J., Carden, G.A., Hints, L., Kaljo, D., Marshall, J.D., Martma, T., Meidla, T., Nolvak, J., 2003. High-resolution stable isotope stratigraphy of Upper Ordovician sequences: Constraints on the timing of bioevents and environmental changes associated with mass extinctions and glaciation. GSA Bulletin, v. 115(1), p.89-104.

[6] Kaljo, D., Hints, L., Martma, T., Nolvak, J., 2001. Carbon isotope stratigraphy in the latest Ordovician of Estonia. Chemical Geology, v.175(1-2), p.49-59.

[7] Young, S.A., Saltzman, M.R., Bergstrom, S.M., 2005. Upper Ordovician (Mohawkian) carbon isotope (δ13C) stratigraphy in eastern and central North America: Regional expression of a pertubation of the global carbon cycle. Palaeogeography, Palaeoclimatology, Palaeoecology, v.222(1-2), p.53-76.

[8] Melchin, M.J., Holmden, C., 2006. Carbon isotpe chemostratigraphy in Arctic Canada: Sea-level forcing of carbonate platform weathering and implications for Hirnantian global correlation. Palaeogeography, Palaeoclimatology, Palaeoecology, v.234(2-4), p.186-200.

[9] Brenchley, P.J., Marshall, J.D., Carden, G.A.F., Robertson, D.B.R., Long, D.G.F., Meidla, T., Hints, L., Anderson, T.F., 1994. Bathymetric and isotopic evidence for a short-lived Late Ordovician glaciation in a greenhouse period. Geology, v.22(4), p.295-298.

[10] Kump, L.R., Arthur, M.A., Patzkowsky, M.E., Gibbs, M.T., Pinkus, D.S., Sheehan, P.M., 1999. A weathering hypothesis for glaciation at high atmospheric pCO2 during the Late Ordovician. Palaeogeography, Palaeoclimatology, Palaeoecology, v.152(1-2), p.173-187.

[11] Young, S.A., Saltzman, M.R., Ausich, W.I., Desrochers, A., Kaljo, D., 2010. Did changes in atmospheric CO_2 coincide with latest Ordovician glacial-interglacial cycles? Palaeogeography, Palaeoclimatology, Palaeoecology, In press.

[12] Copper, P., 2001. Reefs during the multiple crises towards the Ordovician-Silurian boundary: Anticosti Island, eastern Canada, and worldwide. Canadian Journal of Earth Sciences, v.38(2), p.153-171.

[13] Haq, B.U., Schutter, S.R., 2008. A chronology of Palaeozoic sea-level changes. Science, v.322, p.64-68.

[14] Jablonski, D., Chaloner, W.G., 1994. Extinctions in the fossil record. Philosophical Transactions: Biological Sciences, The Royal Society, v.344(1307), p.11-17.

[15] Hallam, A., 1992. Phanerozoic Sea Level Changes. Earth Science Reviews, v.48, p.217-250.

[16] Trotter, J.A., Williams, I.S., Barnes, C.R., Lécuyer, C., Nicoll, R.S., 2008. In situ conodont thermometry: Did cooling oceans trigger the Great Ordovician Biodiversification Event? Geochimica et Cosmochimica Acta, v.72(12), p.A957.

[17] Redecker, D., Kodner, R., Graham, L.E., 2000. Glomalean fungi from the Ordovician. Science, v.289(5486), p.1920-1921.

[18] Servais, T., Harper, D.A.T., Munnecke, A., Owen, A.W., Sheehan, P.M., 2009. Understanding the Great Ordovician Biodiversification Event (GOBE): Influences of Paleogeography, Paleocilmate, or Paleoecology. GSA Today, v.19(4), p.4-10.

[19] Brenchley, P.J., Marshall, J.D., Underwood, C.J., 2001. Do all mass extinctions represent and ecological crisis? Evidence from the Late Ordovician. Geological Journal, v.36, p.329-340.

[20] Achab, A., Paris, F., 2007. The Ordovician chitinozoan biodiversification and its leading factors. Palaeogeography, Palaeoclimatology, Palaeoecology, v.245(1-2), p.5-19.

[21] McLaughlin, P.I., Brett, C.E., 2007. Signatures of Sea-Level Rise on the Carbonate Margin of a Late Ordovician Foreland Basin: A Case Study from the Cincinnati Arch, USA. Palaios, v.22, p.245-267.

[22] Mac Niocaill, C., Van der Pluijm, B.A., Van der Voo, R., 1997. Ordovician paleogeography and the evolution of the Iapetus Ocean, Geology, v.25(2), p.159-162.

[23] Saltzman, M.R., Young, S.A., 2005. Long-lived glaciation in the Late Ordovician? Isotopic and sequence-stratigraphic evidence from western Laurentia. Geology, v.33(2), p.109-112.

[24] Sheehan, P.M., 1973, The relation of Late Ordovician glaciation to the Ordovician-Silurian changeover in North American brachiopod faunas. Lethaia, v.6(2), p.147-154.

[25] Hambrey, M.J., 1985. The late Ordovician-Early Silurian glacial peiod. Paleogeography, Paleoclimatology, Paleoecology, v.51, p.273-289.

[26] Frakes, L.A., Francis, J.E., Syktus, J.I., 1992. Climate modes of the Phanerozoic. Cambridge University Press.

[27] Sheehan, P., 1988. Late Ordovician events and the terminal Ordovician extinction. New Mexico Bureau of Mines and Mineral Resources, v.44, p.405-415.

[28] Loi, A., Ghienne, J.F., Dabard, M.P., Paris, F., Botquelen, A., Christ, N., Elaouad-Debbaj, Z., Gorini, A., Vidal, M., Videt, B., Destombes, J., 2010. The Late Ordovician glacio-eustatic record from a high-latitude storm-dominated shelf succession : the Bou Ingarf section (Anti-Atlas, Southern Morocco). Palaeogeography, Palaeoclimatology, Palaeoecology, in press.

[29] Armstrong, H.A., 2007, On the cause of the Ordovician glaciation, in Deep-Time Perspectives of Climate Change: Marrying the Signal from Computer Models and Biological Proxies. The Micropalaeontological Society, Special Publications. The Geological Society, London, p.101-121.

[30] Long, D.G.F., 1993. Oxygen and carbon isotopes and event stratigraphy near the Ordovician-Silurian boundary, Anticosti Island Quebec. Palaeogeography, Palaeoclimatology, Palaeoecology, v.104(1-4), p.49-59.

[31] Kaljo, D., Hints, L., Martma, T., Nolvak, J., Oraspold, A., 2004. Late Ordovician carbon isotope trend in Estonia, its significance in stratigraphy and environmental analysis. Palaeogeography, Palaeoclimatology, Palaeoecology, v.210, p.165-185.

[32] Sutcliffe, O.E., Harper, D.A.T., Salem, A.A., Whittington, R.J., Craig, J., 2001. The development of an atypical Hirnantia-brachiopod Fauna and the onset of glaciation in the late Ordovician of Gondwana. Transactions of the Royal Society of Edinburgh: Earth Sciences, v.92, p.1-14.

[33] Harper, D.A.T., Rong, J.-Y., Chen, X., 2002. The latest Ordovician Hirnantia Fauna (Brachiopoda) in time and space. Lethaia, v.35(3), p.231-249.

[34] Jin, J., Copper, P., 2008. Response of brachiopod communities to environmental change during the Late Ordovician mass extinction interval, Anticosti Island, Eastern Canada. Fossils and Strata, v.54, p.41-51.

[35] Kaljo, D., Hints, L., Mannik, P., Nolvak, J., 2008. The succession of Hirnantian events based on data from Baltica: brachiopods, chitinozoans, conodonts, and carbon isotopes. Estonian Journal of Earth Sciences, v.57(4), p.197-218.

[36] Copper, P., 2006. Faunal Change across the Ordovician-Silurian Mass Extinction Boundary on Anticosti Island, E Canada. Geological Society of America Abstracts with Programs, v.38(7), p.403.

[37] McCracken, A.D., Barnes, C.R., 1981. Conodont biostratigraphy and paleoecology of the Ellis Bay Formation, Anticosti Island, Quebec, with special reference to Late Ordovician-Early Silurian chronostratigraphy and the systematic boundary. Geological Survey of Canada Bulletin, v.329(2), p.51-134.

[38] Chen, X., Rong, J.-Y., Fan, J.-X., Zhan, R.-B., Mitchell, C.E., Harper, D.A.T., Melchin, M.J., Peng, P., Finney, S.C., Wang, X.-F., 2006. The global boundary Stratotype section and point (GSSP) for the base of the Hirnantian Stage (the uppermost of the Ordovician System. Episodes, v.29, p.183-196.

[39] Melchin, M.J., 2008. Restudy of some Ordovician-Silurian boundary graptolites from Anticosti Island, Canada, and their biostratigraphic significance. Lethaia, v.41, p.55-62.

[40] Soufiane, A., Achab, A., 2000b. Upper Ordovician and Lower Silurian chitinozoans from central Nevada and Arctic Canada. Review of Palaeobotany and Palynology, v.113, p.165-187.

[41] Delabroye, A., 2010. Dynamiques du phytoplankton a travers la limite Ordovicien-Silurien aux faibles paleolatitudes (Laurentia : Ile d'Anticosti, Quebec, Canada ; Baltica : Valga, Estonie) : complements aux donnees des hautes latitudes glaciaires du Gondwana. Ph.D thesis, Universite Lille 1.

[42] Desrochers, A., Gauthier, E.L., 2006. Carte géologique de l'île d'Anticosti (1 : 250 000). Ministère des ressources naturelles de la faune et des parcs, Québec.

[43] Farley, C., 2008. Sediment Dynamics and Stratigraphic Architecture of a mixed carbonate-siliciclastic ramp: the Upper Ordovician (Hirnantian), Ellis Bay Formation, Anticosti Island, Quebec, Canada. Master thesis of the University of Ottawa (unpublished), 80 p.

[44] Veizer, J., Ala, D., Azmy, K., Bruckschen, P., Buhl, D., Bruhn, F., Carden, G.A.F., Diener, A., Ebneth, S., Godderis, Y., Jasper, T., Korte, C., Pawellek, F., Podlaha, O.G., Strauss, H., 1999. $^{87}Sr/^{86}Sr$, $\delta^{13}C$ and $\delta^{18}O$ evolution of Phanerozoic seawater. Chemical Geology, v.161(1-3), p.59-88.

[45] Prokoph, A., Shields, G.A., Veizer, J., 2008. Compilation and time-series analysis of a marine carbonate $\delta^{18}O$, $\delta^{13}C$, $^{87}Sr/^{86}Sr$ and $\delta^{34}S$ database through Earth history. Earth Science Reviews, v.87(3-4), p.113-133.

[46] Zachos, J., Pagani, M., Sloan, L., Thomas, E., Billups, K., 2001. Trends, rhythms, and abberations in global climate 65 Ma to present. Science, v.292(5517), p.686-693.

[47] Shackleton, N.J., 1987. Oxygen isotopes, ice volume and sea level. Quaternary Science Reviews, v.6(3-4), p.183-190.

[48] Shackleton, N.J., Opdyke, N.D., 1973. Oxygen isotope and paleomagnetic stratigraphy of Equatorial Pacific core V28-238: Oxygen isotope temperatures and ice volumes on a 10^5 year and 10^6 year scale. Quaternary Research, v.3(1), p.39-55.

[49] Bowers, T.S., Taylor, H.P., 1985. An Integrated Chemical and Stable-Isotope Model of the Origin of Midocean Ridge Hot Spring Systems. Journal of Geophysical Research, v.90(14), p.12583-12606.

[50] Epstein, S., Ruchsbaum, R., Lowenstam, H.A., Urey, H.C., 1953. Revised Carbonate-Water Isotopic Temperature Scale. GSA Bulletin, v.64(11), p.1315-1326.

[51] Kump, L.R., Arthur, M.A., 1999. Interpreting carbon-isotope excursions: carbonates and organic matter. Chemical Geology, v.161(1-3), p.181-198.

[52] Park, R., Epstein, S., 1960. Carbon isotope fractionation during photosynthesis. Geochimica et Cosmochimica Acta, v.21, 110-126.

[53] Mackenzie, F.T., Lerman, A., 2006. Carbon in the geobiosphere: earth's outer shell. Topics in Geobiology, v.25, Springer, 402 p.

[54] Clark, I.D., Fritz, P., 1997. Environmental Isotopes in Hydrogeology. Lewis Publishers, New York, 328 p.

[55] Cramer, B.D., Saltzman, M.R., 2005. Sequestration of ^{12}C in the deep ocean during the early Wenlock (Silurian) positive carbon isotope excursion. Palaeogeography, Palaeoclimatology, Palaeoecology, v.219, p.333-349.

[56] Sandberg, P.A., 1983. An oscillating trend in Phanerozoic nonskeletal carbonate mineralogy. Nature, v.305, pp.19-22.

[57] McIlreath, I., Morrow, D., 1990. Diagenesis. Geologoical Association of Canada, Reprint Series 4, 338 p.

[58] Weissert, H., Joachimski, M.M., Sarnthein, M., 2008. Chemostratigraphy. Newsletters on Stratigraphy, v.42(3), p.145-179.

[59] Cusack, M., Perez-Huerta, A., Chung, P., Parkinson, D., Dauphin, Y., Cuif, J.P., 2008. Oxygen isotope equilibrium in brachiopod shell fibres in the context of biological control. Mineralogical Magazine, v.72(1), p.239-242.

[60] Shields, G.A., Carden, G.A., Veizer, J., Meidla, T., Rong, J.-Y., Li, R.-Y., 2003. Sr, C, and O isotope geochemistry of Ordovician brachiopods: a major isotopic event around the Middle-Late Ordovician transition. Geochimica et Cosmochimica, v.67, pp.2005-2025.

[61] Azmy, K., Veizer, J., Bassett, M.G., Copper, P., 1998. Oxygen and carbon isotopic composition of Silurian brachiopods: implications for coeval seawater and glaciations. GSA Bulletin, v.110, pp.1499-1512.

[62] Nowlan, G.S., Barnes, C.R., 1987. Thermal maturation of Palaeozoic strata in eastern Canada from conodont colour alteration index (CAI) data with implications for burial history, tectonic evolution, hotspot tracks and mineral and hydrocarbon exploration. Geological Survey of Canada Bulletin, v.367.

[63] Bertrand, R., 1990. Maturation thermique et histoire de l'enfouissement et de la génération des hydrocarbures du bassin de l'archipel de Mingan et de l'Île d'Anticosti. Canadian Journal of Earth Sciences, v.27, p.731-741.

[64] Munnecke, A., Westphal, H., Reijmer, J.J.G., Samtleben, C., 1997. Microspar development during early marine burial diagenesis: a comparison of Pliocene carbonates from the Bahams with Silurian limestones from Gotland (Sweden). Sedimentology, v.44(6), p.977-990.

[65] Bickert, T., Patzold, J., Samtleben, C., Munnecke, A., 1997. Paleoenvironmental changes in the Silurian indicated by stable isotopes in brachiopod shells from Gotland, Sweden. Geochimica et Cosmochimica Acta, v.61(13), p.2717-2730.

[66] Petryk, A.A., 1981. Stratigraphy, sedimentology and palaeogeography of the Upper Ordovician – Lower Silurian of Anticosti Island, Quebec. in Lesperance, P.J., ed., Subcommission on Silurian Stratigraphy, Ordovician-Silurian Boundary Working Group. Field Meeting, Anticosti-Gaspe 1981, v.2, p.11-39.

[67] Underwood, C.J., Crowley, S.F., Marshall, J.D., Brenchley, P.J., 1997. High-Resolution carbon isotope stratigraphy of the basal Silurian Stratotype (Dob's Linn, Scotland) and its global correlation. Journal of the Geological Society, London, v.154, p.709-718.

[68] Finney, S.C., Berry, W.B.N., Cooper, J.D., Ripperdan, R.L., Sweet, W.C., Jacobson, S.R., Soufiane, A., Achab, A., Noble, P.J., 1999. Late Ordovician mass extinctions: A new perspective from stratigraphic sections in central Nevada. Geology, v.27(3), p.215-218.

[69] Lesperance, P.J., Barnes, C.R., Berry, W.B.N., Boucot, A.J., En-Zhi, M., 1987. The Ordovician-Silurian boundary stratotype: consequences of its approval by the IUGS. Lethaia, v.20, p.217-222.

[70] Melchin, M.J., Williams, S.H., 2000. A restudy of the akidograptine graptolites from Dob's Linn and proposed redefined zonation of the Silurian stratotypes in Palaeontology Down Under 2000, Abstracts, Geological Society of Australia, v.63.

[71] Melchin, M.J., Holmden, C., Williams, S.H., 2003. Correlation of graptolite zones, chitinozoan biozones, and carbon isotope curves through the Hirnantian in Ordovician from the Andes – Proceedings of the 9th International Symposium on the Ordovician System, eds. Albanesi, G.L., Beresi, M.S., Peralta, S.H., INSUGEO, Serie Correlación Geológica, p.101-104.

[72] Verniers, J., Vandenbroucke, T.R.A., 2006. Chitinozoan biostratigraphy in the Dob's Linn Ordovician-Silurian GSSP, Southern Uplands, Scotland. Geologiska Foereningan, v.128, p.195-202.

[73] Fan, J., Peng, P., Melchin, M.J., 2009. Carbon isotopes and event stratigraphy near the Ordovician-Silurian boundary, Yichang, South China. Palaeogeography, Palaeoclimatology, Palaeoecology, v.276(1-4), 160-169.

[74] Cooper, R.A., Sadler, P.M., 2004. Ordovician system in A Geological Time Scale, eds. Gradstein, F.M., Ogg, J.G., Smith, A.G., Cambridge University Press, Cambridge, p.165-187.

[75] Laporte, D.F., Holmden, C., Patterson, W.P., Loxton, J.D., Melchin, M., Mitchell, C.E., Finney, S.C., Sheets, H.D., 2009. Local and global perspectives on carbon and nitrogen cycling during the Hirnantian glaciation. Palaeogeography, Palaeoclimatology, Palaeoecology, v.276(1-4), p.182-195.

[76] Ross, R.J. Jr., Nolan, T.B., Harris, A.G., 1979. The Upper Ordovician and Silurian Hanson Creek Formation of central Nevada in Shorter Contributions to Stratigraphy and Structural Geology, U.S. Geological Survey Professional Papers, P.1126, A-J, C1-C22.

[77] Panchuk, K.M., Holmden, C., Kump, L.R., 2005. Sensitivity of the epeiric sea carbon isotope record to local-scale carbon cycle processes: Tales from the Mohawkian Sea. Palaeogeography, Palaeoclimatology, Palaeoecology, v.228(3-4), p.320-337.

[78] Holmden, C., Creaser, R.A., Muehlenbachs, K., Leslie, S.A., Bergstrom, S.M., 1998. Isotopic evidence for geochemical decoupling between ancient epeiric seas and bordering oceans: Implications for secular curves. Geology, v.26(6), p.567-570.

[79] Brenchley, P.J., Carden, G.A.F., Marshall, J.D., 1995. Environmental Changes Associated with the "First Strike" of the Late Ordovician Mass Extinction. Modern Geology, v.20, p.69-82.

[80] Meyer, K.M., Kump, L.R., 2008. Oceanic Euxinia in Earth History: Causes and Consequences. Annual Review of Earth and Planetary Sciences, v.36, p.251-288.

[81] Immenhauser, A., Holmden, C., 2008. Interpreting the Carbon-isotope record of ancient shallow epeiric seas: lessons from the recent in Dynamics of Epeiric Seas, Holmden and Pratt (eds.), Geological Association of Canada Special Publication, v.48, p.137-174.

[82] Cramer, B., Saltzman, M.R., 2005. Fluctuations in epeiric sea carbonate production during Silurian positive carbon isotope excursions: A review of proposed paleoceanographic models. Palaeogeography, Palaeoclimatology, Palaeoecology, v.245(1-2), p.37-45.

[83] Jeppsson, L., Calner, M., 2003. The Silurian Mulde Event and a scenario for secundo-secundo events. Transactions of the Royal Society of Edinburgh: Earth Sciences, v.93, p.135-154.

[84] Munnecke, A., Samtleben, C., Bickert, T., 2003. The Ireviken Event in the lower Silurian of Gotland, Sweden-relation to similar Palaeozoic and Proterozoic events. Palaeogeography, Palaeoclimatology, Palaeoecology, v.195, p.99-124.

Appendix A. Box Model for the Late Ordovician Global Carbon Cycle

Presented here is a model designed to simulate the Global Carbon Cycle for the Late Ordovician world. It is based mostly on the work of Mackenzie and Lerman [51], who through a review of hundreds of scientific studies concerning the past and present carbon cycling, composed an overview of the global carbon cycle, in which carbon reservoirs and fluxes are quantified on a global scale. Characteristics of the Ordovician-Silurian carbon cycle were estimated using Mackenzie and Lerman's model and considerations such as higher sea level, increased Ordovician pCO_2 values (~4000 ppm) and the absence of vascular land plants. This model can be used to test some of the theoretical aspects of the hypotheses concerning the $\delta^{13}C$ excursions that occurred near the O-S Boundary. The estimated quantities of the reservoirs and the fluxes of the Ordovician-Silurian global carbon cycle are shown in the following tables.

Reservoir	abbr.	Gt C (today)	Gt C (O-S)	$\delta^{13}C$ (‰)
Lithosphere	l	150,000,000	69,802,795	-6
Carbonates	c	70,000,000	150,000,000	0
Fossil Fuels	f	20,000	10,000	-28
Reactive Sediments	r	3,000	18,000	0
Deep Ocean	d	38,000	220,000	0
Surface Ocean	s	1,000	6,000	+3
Phytomass	p	500	5	-28
Soil		2500	0	
Atmosphere	a	800	9,000	-6

Flux	abbr.	Gt/yr (today)	Gt/yr (O-S)
Terrestrial primary production	a → a	63.1	0
Marine primary production	a → a	50.5	80
Volatilization from soil	a → a	62.5	0
CO_2 dissolution & evasion	a → a	96	1050
$CaCO_3$ production & dissolution	s → s	0.5	0.5
CO_2 uptake by plants & humus	a → p	0.6	0
CO_2 used in weathering	a → l	0.26	0.13
River input from silicates	l → s	0.25	0.13
River input from carbonates	c → s	0.13	0.06
River input from organic matter	c → s	0.31	0
Ocean-atmosphere exchange	s → a	0.48	0
$CaCO_3$ storage in sediments	s → c	0.38	0.38
Organic C storage in sediments	s → c	0.1	0.1
Upwelling	d → s	2.15	12.5
Volcanism & metamorphism	l → a	0.12	0.18
Hydrothermal	l → a	0.1	0.15
Uplift	l → a	0.4	0.4

Note that in the Late Ordovician world, organic carbon was produced exclusively in the Surface Ocean Reservoir.

In this simplified model, the relationships between various reservoirs, fluxes and isotope values of carbon are described by the conservation of mass

$\Delta M_x/\Delta t$	$=$	$\Sigma F_{i\text{-}x}$ –	$\Sigma F_{x\text{-}i}$
		flux in	flux out

and a similar equation involving the enrichment of organic carbon.

$\Delta(M_x{*}\delta_x)/\Delta t$	$=$	$\Sigma F_{i\text{-}x} * \delta_i - \Sigma F_{x\text{-}I} * \delta_x$ +	$\Sigma F_{i\text{-}x}^{\circ} * (\delta_i{+}\varepsilon) - \Sigma F_{x\text{-}i}^{\circ} * (\delta_x{+}\varepsilon)$
		inorganic carbon	organic carbon

Using the product rule and the two equations above we arrive at the equation of isotope continuity.

$$\Delta\delta_x/\Delta t = [\Sigma F_{i\text{-}x} * (\delta_i\text{-}\delta_x) + \Sigma F_{i\text{-}x}^{\circ} * (\delta_i{+}\varepsilon) - \Sigma F_{x\text{-}i}^{\circ} * (\delta_x{+}\varepsilon)] / M_x$$

Where: M_x represents the mass of C in a reservoir.
$F_{i\text{-}x}$ is the flux of C from reservoir i into reservoir x
$F_{x\text{-}i}^{\circ}$ is the flux of organic C from reservoir x to reservoir i
δ_x is the isotopic value of a carbon reservoir
ε is the depletion factor for organic carbon

$M_s = 6000$ Gt	$\varepsilon = -28$ ‰
$F_{l\text{-}s} = 0.13$ Gt/yr	$\delta_a = -6$ ‰
$F_{c\text{-}s} = 0.06$ Gt/yr	$\delta_l = -6$ ‰
$F_{d\text{-}s} = 12.5$ Gt/yr	$\delta_c = 0$ ‰
$F_{s\text{-}a} = 0$ Gt/yr	$\delta_c^{\circ} = -28$ ‰
$F_{s\text{-}c} = 0.38$ Gt/yr	$\delta_d = 0$ ‰
$F_{s\text{-}c}^{\circ} = 0.1$ Gt/yr	$\delta_s = +3$ ‰

In the case of the global productivity hypothesis, a change in the rate of burial of organic carbon, $F_{s\text{-}c}^{\circ}$, brought the $\delta^{13}C$ of the surface ocean from 0 to 4 ‰, in the timespan of approximately 100,000 to 500,000 years.

$$\Delta\delta_s * M_s /\Delta t = F_{l\text{-}s} * (\delta_l\text{-}\delta_s) + F_{c\text{-}s} * (\delta_c\text{-}\delta_s) + F_{d\text{-}s} * (\delta_d\text{-}\delta_s) - F_{s\text{-}c}^{\circ} * (\delta_s{+}\varepsilon)$$

+4 ‰ * 6000 Gt/Δt = 0.13 Gt/yr * (-6 ‰-3 ‰) + 0.06 Gt/yr * (0 ‰-3 ‰) + 12.5 Gt/yr * (0 ‰-3 ‰) – $F_{s\text{-}c}^{\circ}$ * (3 ‰-28 ‰)

24,000 ‰Gt /Δt = (-39 ‰Gt/yr + 25 ‰ * $F_{s\text{-}c}^{\circ}$)

For the lower limit, Δt = 100,000 yr, $F_{s\text{-}c}^{\circ}$ = 1.564 Gt/yr
For the upper limit, Δt = 500,000 yr, $F_{s\text{-}c}^{\circ}$ = 1.556 Gt/yr

Therefore, to produce a $\delta^{13}C$ increase of 4 ‰ in the surface ocean, the carbon burial rate has to increase to approximately 1.56 Gt/yr, 15 times the present day rate of carbon burial in the oceans (0.1 Gt/yr).

To test Cramer and Saltzman's hypothesis for ocean state changes, the value for $F_{d\text{-}s}$, which represents upwelling of inorganic carbon from the deep ocean to the surface ocean will change from 12.5 Gt/yr to 0, which assumes stratified oceans with no active thermohaline circulation. This is difficult to achieve on a global scale but can be easily achieved on regional (basinal) scales.

$+4\ ‰ * 6000\ \mathrm{Gt}/\Delta t = 0.13\ \mathrm{Gt/yr} * (-6\ ‰ - 3\ ‰) + 0.06\ \mathrm{Gt/yr} * (0\ ‰ - 3\ ‰) + 0\ \mathrm{Gt/yr} * (0\ ‰ - 3\ ‰) - F_{s\text{-}c}^{\circ} * (3\ ‰ - 28\ ‰)$

$$24{,}000\ ‰\mathrm{Gt}/\Delta t \quad = \quad (-1.35\ ‰\mathrm{Gt/yr} + 25\ ‰ * F_{s\text{-}c}^{\circ})$$

$\Delta t = 100{,}000$ yr, $\quad F_{s\text{-}c}^{\circ} = 0.064$ Gt/yr
$\Delta t = 500{,}000$ yr, $\quad F_{s\text{-}c}^{\circ} = 0.056$ Gt/yr

Therefore, a $\delta^{13}C$ increase of 4 ‰ in the surface ocean is possible with modern day burial rates of organic carbon if upwelling of water from the deep ocean were to cease completely.

Appendix B. Results of Isotope Study on micrite from the Ellis Bay Formation

Stable isotope measurements made from micrite samples are compiled here. Some samples were analyzed more than once: "QCD" indicates a Quality Control Duplicate, which is used to test the accuracy of the mass spectrometer, "repeat" denotes a sample that was analyzed again due to it being an anomalous measurement, or having encountered a problem in the process of measurement.

Section 1A, West End (Baie St. Claire - Laframboise section) GPS Location

The base of this section is in the Homard Member of the Vaureal Formation, it spans the entire Ellis Bay Formation, and terminates in the lowermost member of the Becscie Formation, the Fox Point.

Sample #	Height (m)	Description	$\delta^{13}C$ (‰)	$\delta^{18}O$ (‰)	Latitude	Longitude
B-M-01	0	mudstone/packstone	0.3	-3.22		
B-M-02	1.33	wackestone/packstone	0.24	-2.98		
B-M-03	2.66	wackestone/packstone	0.18	-3.15		
B-M-03 QCD	2.66	wackestone/packstone	0.16	-3.35		
B-M-04	4	wackestone/packstone	0.32	-2.74		
B-M-05	5.33	wackestone/packstone	0.05	-4.05		
B-M-06	6.66	mudstone/packstone	0.26	-3		
B-M-07	8	wackestone	0.2	-3.11		
B-M-08	9.33	wackestone	0.07	-3.92		
B-M-09	10.66	packstone	0.26	-3.68		
B-M-10	12	mudstone/wackestone	0.08	-4.07		
B-M-11	13.33	wackestone/packstone	0.4	-4.34		
B-M-12	14.66	mudstone/packstone	0.41	-4.25		
B-M-13	16	mudstone/wackestone	0.23	-4.66		
B-M-13 QCD	16	mudstone/wackestone	0.26	-4.64		
B-M-14	17.33	mudstone	0.59	-4.27		
B-M-15	18.66	mudstone/wackestone	0.22	-4.32		
B-M-16	20	mudstone/wackestone	0.49	-3.83		
B-M-17	21.8	wackestone	0.66	-5.01		
B-M-18	23.6	mudstone/wackestone	-0.18	-4.74		
B-M-19	25.4	wackestone	0.32	-4.83		
B-M-20	27.3	wackestone/packstone	0.35	-4.13		
B-M-21	29.1	wackestone/packstone	0.63	-4.02		
B-M-22	29.9	packstone	0.18	-3.88		
B-M-23	32.7	packstone	-0.03	-4.13		
B-M-24	34.6	wackestone	0.51	-4.45		
B-M-24 QCD	34.6	wackestone	0.48	-4.47		
B-M-25	36.4	wackestone	0.49	-4.13		
B-M-26	38.2	mudstone/wackestone	0.52	-3.87		
B-M-27	40	wackestone	0.43	-4.74		
B-M-28	41.8	wackestone	1.53	-1.68		
B-M-28 repeat	41.8	wackestone	1.75	-1.47		
B-M-29	43.6	mudstone/wackestone	0.6	-3.42		
B-M-30	45.4	mudstone/wackestone	0.3	-4.12		
B-M-31	47.3	mudstone/wackestone	0.46	-4.48		
B-M-32	49.1	wackestone	0.7	-4.26		

B-M-33	49.9	wackestone/packstone	0.7	-3.64
B-M-33 QCD	49.9	wackestone/packstone	0.72	-3.96
B-M-34	52.7	mudstone/wackestone	0.68	-4.05
B-M-35	54.6	packstone	0.36	-4.23
B-M-36	56.4	mudstone/packstone	0.85	-3.58
B-M-37	58.2	wackestone	0.39	-3.83
B-M-38	60	wackestone/packstone	0.88	-3.48
B-M-39	61.8	mudstone/wackestone	0.58	-4.34
B-M-40	63.6	wackestone	0.15	-3.94
B-M-41	65.4	wackestone	0.37	-3.65
B-M-42	67.3	mudstone/wackestone	0.48	-3.53
B-M-43	69.1	wackestone/packstone	0.38	-4.18
B-M-43 QCD	69.1	wackestone/packstone	0.36	-4.18
B-M-44	69.9	mudstone/wackestone	0.52	-3.65
B-M-45	72.7	mudstone/packstone	0.62	-3.36
B-M-46	74.6	mudstone/packstone	0.32	-3.57
B-M-47	76.4	wackestone/packstone	0.71	-4.26
B-M-48	78.2	wackestone/packstone	0.01	-3.85
B-M-49	80	mudstone/wackestone	-0.01	-4.23
B-M-50	81.66	wackestone/packstone	0.28	-3.72
B-M-51	83.33	mudstone/wackestone (stylolitic)	-0.07	-4.62
B-M-52	85	mudstone/wackestone	0.29	-3.43
B-M-53	86.66	mudstone	0.44	-3.68
B-M-53 QCD	86.66	mudstone	0.43	-3.65
B-M-54	88.33	mudstone	0.57	-3.76
B-M-55	90	mudstone	0.3	-3.71
B-M-56	91.66	mudstone/wackestone	0.36	-3.62
B-M-57	93.33	mudstone/wackestone	0.33	-3.69
B-M-58	95	wackestone	0.4	-3.82
B-M-59	96.66	wackestone	0.45	-3.66
B-M-60	98.33	wackestone	0.16	-3.97
B-M-61	100	mudstone (stylolitic)	0.55	-3.45
B-M-62	101.66	mudstone	0.78	-3.46
B-M-63	103.33	mudstone/wackestone	0.97	-2.89
B-M-63 QCD	103.33	mudstone/wackestone	1	-2.9
B-M-64	105	wackestone/packstone	1.22	-3.02
B-M-65	106.66	mudstone/wackestone	0.93	-3.08
L-M-01	100	packstone (brachiopod)	0.8	-3.46
L-M-02	102.5	wackestone/packstone	0.71	-3.26
L-M-03	105	wackestone	1.06	-4.58
L-M-04	107.5	packstone	1.01	-3.21
L-M-05	110	packstone	0.84	-3.36
L-M-06	110.6	packstone	0.44	-3.76
L-M-07	111.1	packstone (brachiopod)	0.25	-3.13
L-M-08	111.7	wackestone/packstone	0.76	-3.04
L-M-08 QCD	111.7	wackestone/packstone	0.74	-2.99
L-M-09	112.2	packstone	0.61	-3.22
L-M-10	112.8	wackestone/packstone	0.98	-3.04

L-M-11	113.3	wackestone	0.26	-3.43	
L-M-12	113.9	packstone	0.66	-3.33	N49° 49.263' W064° 26.641'
L-M-13	114.4	packstone	1.16	-3.48	
L-M-14	115	packstone/grainstone	0.85	-3.89	
L-M-15	115.83	packstone	0.98	-3.67	
L-M-16	116.66	packstone	1.61	-3.04	
L-M-17	117.5	grainstone (peloidal)	1.94	-3.13	
L-M-18	118.33	packstone	1.59	-3.44	
L-M-18 QCD	118.33	packstone	1.61	-3.42	
L-M-19	119.16	packstone	1.6	-3.24	
L-M-20	120	packstone	0.28	-3.25	
L-M-21	120.83	wackestone	2.26	-3.26	
L-M-22	121.66	wackestone	1.47	-3.66	
L-M-23	122.5	wackestone	2.36	-3.18	N49° 50.156' W064° 27.060'
L-M-24	123.33	mudstone	2.35	-3.02	
L-M-25	124.16	packstone	1.17	-3.55	
L-M-26	125	packstone	1.1	-3.96	
L-M-27	127.5	wackestone/packstone	1.69	-3.49	
L-M-28	130	packstone	1.44	-3.5	
L-M-28 QCD	130	packstone	1.51	-3.48	
L-M-29	132.5	wackestone/packstone	1.32	-3.14	
L-M-30	134.6	wackestone	1.9	-3.28	
L-M-31	136.7	mudstone/wackestone	1.78	-3.32	
L-M-32	138.8	mudstone/wackestone	1.56	-3.43	
L-M-33	140.9	wackestone	1.29	-3.26	
L-M-34	143	wackestone	0.98	-3.15	
L-M-35	145.1	wackestone	1.15	-3.48	
L-M-36	147.2	wackestone	1.19	-3.25	
L-M-37	149.3	mudstone/wackestone	1.47	-3.15	
L-M-38	151.4	wackestone	0.81	-3.28	
L-M-38 QCD	151.4	wackestone	0.85	-3.29	
L-M-39	153.5	mudstone	1.46	-3.36	
L-M-39 repeat	153.5	mudstone	1.54	-3.75	
L-M-40	155.6	mudstone/wackestone	0.95	-3.34	
L-M-41	157.4	mudstone	0.95	-3.46	
L-M-42	159.2	wackestone	1.04	-3.45	
L-M-43	161	wackestone/packstone	1.08	-3.4	
L-M-44	162.8	wackestone	0.9	-3.28	
L-M-45	164.6	wackestone/packstone	0.54	-3.38	
L-M-46	166.4	wackestone/packstone	0.66	-3.31	
L-M-47	168.2	packstone	0.5	-3.73	
L-M-48	170	wackestone	0.99	-3.51	
L-M-49	171.8	wackestone	0.02	-3.18	
L-M-50	173.6	mudstone/wackestone	0.72	-3.32	
L-M-50 QCD	173.6	mudstone/wackestone	0.72	-3.34	
L-M-51	175.4	mudstone/wackestone	0.82	-3.14	
L-M-52	177.2	wackestone	0.84	-3.26	
L-M-53	179	wackestone	1.11	-3.9	

L-M-54	180.8	wackestone	1.04	-3.65
L-M-55	182.6	wackestone	1.02	-3.62
L-M-56	184.4	wackestone	0.62	-4.58
L-M-57	186.2	packstone	0.74	-3.88
L-M-58	188	packstone	0.49	-3.47
L-M-59	188.9	wackestone/packstone	0.47	-3.61
L-M-59 QCD	188.9	wackestone/packstone	0.55	-3.53
L-M-60	189.8	wackestone/packstone	0.29	-3.52
L-M-61	190.7	wackestone/packstone	0.2	-3.71
L-M-62	191.6	wackestone/packstone	0.26	-3.83
L-M-63	192.4	packstone (brachiopod)	0.47	-3.81
L-M-64	193.3	packstone	0.52	-4.06
L-M-65	194.2	packstone	0.69	-3.4
L-M-66	195.1	packstone	0.94	-3.1
L-M-67	196	wackestone/packstone	1.99	-3.03
L-M-68	197.5	mudstone	1.95	-3.71
L-M-69	199	mudstone/wackestone	1.93	-3.69
L-M-70	201	wackestone	1.92	-3.92
L-M-70 QCD	201	wackestone	1.92	-3.9
PL-4i	197.5	grainstone (peloidal)	1.80	-2.75
PL-5i	198	grainstone (peloidal)	1.84	-3.12
PL-6i	198.5	grainstone (peloidal)	2.20	-3.53
PL-7i	199	grainstone (peloidal)	2.27	-3.42
PL-7i QCD	199.5	grainstone (peloidal)	2.11	-3.54
PL-8i	200	grainstone (peloidal)	2.05	-3.87
PL-9i	200.5	grainstone (peloidal)	2.69	-3.46
PL-10i	200.9	grainstone (peloidal)	3.56	-2.73
PL-11i	201.1	grainstone (peloidal)	3.85	-2.38
PL-12i	201.5	grainstone (oncolitic)	4.04	-2.74
PL-13i	201.8	grainstone (oncolitic)	3.78	-2.88
PL-14i	202.1	grainstone (oncolitic)	3.48	-2.69
PL-15i	202.8	grainstone (oncolitic)	2.95	-2.96
PL-16i	203.2	packstone	3.85	-2.75
PL-16i QCD	203.5	packstone	3.81	-2.64
PL-17Bi	203.8	packstone	3.60	-2.85
PL-18i	204.1	packstone	3.63	-2.28
PL-19Ai	204.3	packstone	2.18	-4.39
PL-20i	204.5	packstone	2.31	-4.36
PL-21i	204.8	packstone	1.49	-3.64
PL-21i QCD	205.1	wackestone	1.13	-3.17
PL-22i	205.3	wackestone	1.16	-3.15
PL-23i	205.6	wackestone	1.18	-3.08
PL-24i	205.9	wackestone	0.58	-3.99
PL-25i	206.2	wackestone	0.56	-3.34
PL-26i	206.5	wackestone	0.00	-4.24
PL-27i	207.5	wackestone	0.42	-3.80
PL-28i	208.5	wackestone	0.34	-3.69

Section 1B, Ellis Bay GPS Location

Section 1B begins in the upper portion of the Ellis Bay and ends in the lower Becscie.

Sample #	Height (m)		$\delta^{13}C$ (‰)	$\delta^{18}O$ (‰)	Latitude	Longitude
E-M-01	0	wackestone	0.46	-3.31		
E-M-02	0.5	wackestone	0.44	-3.58		
E-M-03	1	wackestone	0.31	-3.61		
E-M-04	1.5	wackestone	0.33	-3.65		
E-M-05	2	wackestone	0.07	-3.47		
E-M-06	2.5	wackestone	0.96	-3.55		
E-M-07	3	wackestone	0.73	-3.45		
E-M-08	3.5	wackestone	0.14	-3.62		
E-M-09	4	wackestone	0.62	-3.45		
E-M-10	4.5	wackestone	0.6	-3.38		
E-M-11	5	wackestone	0.63	-3.61		
E-M-12	5.5	wackestone	0.66	-3.22		
E-M-13	6	wackestone	0.7	-3.58		
E-M-13 QCD	6	wackestone	0.68	-3.38		
E-M-14	6.5	wackestone/packstone	1.07	-2.92		
E-M-15	7	wackestone	1.84	-2.8		
E-M-16	7.5	wackestone	1.92	-2.16		
E-M-17	8	wackestone (laminated)	2	-2.44		
E-M-18	8.5	mudstone	1.88	-3.41		
E-M-19	9	wackestone/packstone	2.48	-3.97		
E-M-20	9.5	mudstone	2.14	-3.40		
E-M-21	9.8	wackestone/packstone	2.69	-3.38		
E-M-22	10.1	wackestone (rugosa)	2.82	-2.95		
E-M-23	10.4	mudstone/wackestone	3.04	-2.96		
E-M-24	10.7	wackestone (nodular)	3.39	-2.32		
E-M-25	11	mudstone/wackestone	3.19	-2.34		
E-M-26	11.3	mudstone/wackestone	1.72	-2.15		
E-M-26 QCD	11.3	mudstone/wackestone	1.74	-2.32		
E-M-27	11.6	mudstone	0.84	-3.08		
E-M-28	11.9	mudstone	1.04	-3.38		
E-M-29	12.2	mudstone (stylolitic)	0.57	-2.72		
E-M-30	12.5	mudstone/wackestone	0.8	-2.19		
E-M-30 QCD	12.5	wackestone	0.8	-2.07		
E-M-31	12.8	wackestone	0.61	-5.13		
E-M-32	13.1	mudstone	0.24	-4		
E-M-33	14.5	mudstone/wackestone	0.34	-2.91		
E-M-34	15.5	mudstone/wackestone	0.21	-3.1		
E-M-35	16.5	mudstone	0.14	-3.68		
E-M-36	17.5	mudstone	0.25	-3.24		
E-M-37	18.5	mudstone	0.09	-3.1		
E-M-38	19.5	mudstone/wackestone	0.04	-2.32		
E-M-39	20.5	wackestone	0.06	-4.06		
E-M-40	21.5	mudstone/wackestone	0.07	-3.31		
E-M-41	22.5	mudstone/wackestone	0.21	-3.09		

E-M-42	23.5	mudstone/wackestone	-0.08	-4.07
E-M-43	24.5	mudstone/wackestone	0.14	-3.52
E-M-44	25.5	mudstone	0.11	-3.63
E-M-44 QCD	25.5	mudstone	0.1	-3.5
E-M-45	26.5	mudstone	0.12	-3.25
E-M-46	27.5	mudstone	0.18	-3.04
E-M-47	28.5	mudstone/wackestone	-0.28	-4.44

Section 2, NACP drill core — GPS Location

This section begins in the uppermost Vaureal and is terminates in the basal Becscie. The $\delta^{13}C$ profile in Figure 12 begins with NACP-9, and excludes the last two samples.

Sample #	Height (m)		$\delta^{13}C$ (‰)	$\delta^{18}O$ (‰)	Latitude	Longitude
NACP-1	0		0.47	-3.51	N49° 62.073'	W063° 43.791'
NACP-2	3		0.82	-2.59		
NACP-3	6		0.63	-3.82		
NACP-4	8		0.12	-3.28		
NACP-5	11		-0.38	-3.58		
NACP-6	15		0.75	-3.5		
NACP-7	18		0.83	-3.23		
NACP-8	20		0.47	-3.68		
NACP-9	23	wackestone/packstone	0.66	-2.93		
NACP-10	26	mudstone	-0.15	-3.89		
NACP-11	29	wackestone	-0.32	-3.91		
NACP-12	31	wackestone	0.99	-3.85		
NACP-13	33	wackestone/packstone	0.73	-3.59		
NACP-14	34	wackestone/packstone	1.64	-3.37		
NACP-15	35	wackestone	1.87	-3.03		
NACP-16	36	wackestone	1.78	-3.68		
NACP-17	39	wackestone	1.25	-3.52		
NACP-18	40	wackestone/packstone	1.84	-3.53		
NACP-19	41	wackestone/packstone	1.67	-2.77		
NACP-20	43	mudstone	1.99	-3.77		
NACP-21	45	mudstone	1.11	-3.66		
NACP-22	48	mudstone	1.64	-3.43		
NACP-23	51	wackestone/packstone	1.57	-2.99		
NACP-24	53	wackestone/packstone	1.59	-3.1		
NACP-25	56	wackestone/packstone	1.57	-3.13		
NACP-26	63	wackestone/packstone	1.15	-3.26		
NACP-27	65	mudstone	0.82	-2.64		
NACP-28	68	wackestone	0.38	-3.22		
NACP-31	78	wackestone	0.78	-3.18		
NACP-32	80	mudstone	0.64	-3.76		
NACP-33	83	mudstone	0.74	-3.11		
NACP-34	86	mudstone	-0.18	-3.04		
NACP-35	89	wackestone	-0.74	-3.68		
NACP-36	93	wackestone	0.78	-3.78		
NACP-37	95.5	wackestone/packstone	-0.82	-3.42		
NACP-38	98	packstone/grainstone	-0.36	-3.6		

NACP-39	98.5	wackestone/packstone	1.35	-3.66
NACP-40	100	wackestone/packstone	2.15	-3.35
NACP-41	100.5	wackestone/packstone	3.81	-3.74
NACP-42	101.5	wackestone/packstone	4.18	-3.36
NACP-43	102	wackestone/packstone	4.65	-3.82
NACP-44	102.5	wackestone/packstone	3.43	-3.68
NACP-45	103	wackestone/packstone	2.48	-4.1
NACP-46	103.25	wackestone/packstone	4.03	-4.48
NACP-47	103.5	wackestone/packstone	3.76	-4.68
NACP-48	105	wackestone/packstone	0.25	-2.71
NACP-49	105.5	wackestone/packstone	1.35	-3.46
NACP-51	108	wackestone/packstone	1.21	-4.14
NACP-52	109.25	wackestone/packstone	0.97	-3.84
NACP-53	113	wackestone/packstone	0.63	-4.33
NACP-54	115	wackestone/packstone	0.74	-3.66
NACP-55	118	wackestone/packstone	-0.26	-4.27
NACP-56	122		0.36	-4.2
NACP-57	125		-0.02	-3.78

Section 3, Vaureal River — GPS Location

This section begins in the lowe Vaureal and ends just below the base of the Laframboise Member.

Sample #	Height (m)		$\delta^{13}C$ (‰)	$\delta^{18}O$ (‰)	Latitude	Longitude
VC-M-01	0	mudstone/packstone	0.01	-4.05	N49° 33.855'	W062° 41.608'
VC-M-02	2.5	mudstone/packstone	-0.18	-4.22		
VC-M-03	5	mudstone/packstone	-0.13	-4.48		
VC-M-03 QCD	5	mudstone/packstone	-0.11	-4.3		
VC-M-04	7.5	mudstone/packstone	0.57	-4.02		
VC-M-05	10	packstone	-1.88	-5.29		
VC-M-05 repeat	10	packstone	-0.21	-4.35		
VC-M-06	12.5	mudstone/wackestone	0.32	-4.12		
VC-M-07	15	mudstone/packstone	0.01	-4.31		
VC-M-08	17.5	mudstone/wackestone	-0.06	-4.12		
VC-M-09	20	mudstone/wackestone	0.53	-3.86		
VC-M-10	22.5	mudstone/wackestone	-0.17	-4.13		
VC-M-11	25	mudstone/wackestone	0.35	-3.78		
VC-M-12	27.5	wackestone/packstone	-0.21	-4.25		
VC-M-13	30	mudstone/wackestone	0.19	-3.71		
VC-M-13 QCD	30	mudstone/wackestone	0.08	-4.46		
VC-M-13 repeat	30	mudstone/wackestone	0.68	-3.82		
VC-M-14	32.5	mudstone/wackestone	0.17	-4.22		
VC-M-15	35	mudstone/wackestone	0.18	-4.23		
VC-M-16	37.5	mudstone/wackestone	0.36	-3.71		
VC-M-18	40	mudstone/wackestone	0.12	-4.18		
VC-M-19	42.5	mudstone/packstone	0.93	-4.34		
VC-M-20	45	mudstone/wackestone	0.54	-4.84		
VC-M-21	47.5	mudstone	-0.2	-4.09		
VC-M-22	50	mudstone	0.31	-5.39	N49° 33.619'	W062° 41.608'
V-M-01	54	mudstone/wackestone (stylolitic)	0.29	-3.22		

V-M-02	55.5	mudstone/packstone	0.23	-3.3	
V-M-03	57	mudstone/packstone	0.32	-3.67	
V-M-03 QCD	57	mudstone/packstone	0.35	-3.5	
V-M-04	58.5	mudstone/wackestone	0.14	-3.34	
V-M-05	60	mudstone/wackestone	0.05	-3.23	
V-M-06	61.5	mudstone	0.1	-3.32	
V-M-07	63	wackestone	0.43	-2.99	
V-M-08	64.5	mudstone/packstone	0.12	-3.21	
V-M-09	66	mudstone/wackestone	-0.2	-3.6	
V-M-10	67.5	wackestone	-0.2	-3.08	
V-M-11	69	wackestone	-0.49	-3.36	
V-M-12	70.5	wackestone	0.14	-3.07	
V-M-12 QCD	70.5	wackestone	0.1	-2.86	
V-M-13	72	wackestone	-0.01	-3.92	
V-M-14	73.5	wackestone/packstone	0.16	-3.19	
V-M-15	75	wackestone	-0.38	-3.2	
V-M-16	76.5	grainstone (skeletal)	-0.36	-3.2	
V-M-17	78	grainstone (peloidal)	-0.26	-4.27	
V-M-18	79.5	wackestone	-0.25	-3.18	
V-M-19	81	mudstone/wackestone	-0.41	-2.94	
V-M-20	82.5	wackestone/packstone	-0.5	-3.34	
V-M-21	84	wackestone/packstone	-0.14	-3.24	
V-M-21 repeat	84	wackestone/packstone	0	-3.64	
V-M-22/23a	85.5	wackestone/packstone	0.01	-4.04	
V-M-22/23a QCD	85.5	wackestone/packstone	-0.12	-2.92	
V-M-22/23a repeat	85.5	wackestone/packstone	0.26	-3.15	
V-M-22/23b	87	wackestone/packstone	0.15	-2.64	
V-M-22/23b repeat	87	wackestone/packstone	0.47	-2.86	
V-M-24	88.5	mudstone/wackestone	-0.09	-4.62	
V-M-25	90	packstone	-0.13	-4.04	
V-M-26	91.5	mudstone/wackestone	0.55	-3.11	
V-M-27	98	mudstone/packstone	0.48	-3.67	
V-M-28	100	wackestone/packstone	0.34	-3.27	
V-M-29	101.5	wackestone/packstone	1.02	-3.09	
V-M-30	106.5	mudstone/packstone	1.58	-1.93	
V-M-31	107.5	mudstone/packstone	0.8	-2.05	
V-M-32	110.5	mudstone/packstone	-0.38	-2.51	N49° 31.818' W062° 43.275'
V-M-32 QCD	110.5	mudstone/packstone	-0.5	-2.45	
V-M-33	117	wackestone/packstone	-0.5	-3.93	
V-M-34	118	mudstone/packstone	0.39	-3.03	
V-M-35	119	wackestone/packstone	0.49	-3.13	
V-M-36	120	mudstone/packstone	2.11	-2.91	
V-M-37	122	wackestone/packstone	0.01	-5.2	
V-M-37 repeat	122	wackestone/packstone	0.48	-5.41	

Section 4, Natiscotec River

This section begins in the Vaureal and ends in the basal Becscie.

Sample #	Height (m)		$\delta^{13}C$ (‰)	$\delta^{18}O$ (‰)	GPS Location Latitude	Longitude
N-M-01	0	mudstone/wackestone	0.3	-4.07	N49° 29.525'	W062° 28.758'
N-M-02	2.5	wackestone/packstone	0.49	-3.9		
N-M-03	5	packstone (laminated)	0.38	-3.82		
N-M-04	7.5	wackestone	0.47	-3.8		
N-M-05	10	mudstone/wackestone	0.45	-3.87		
N-M-06	12.5	wackestone	0.12	-4.5		
N-M-07	15	wackestone	0.25	-4.08		
N-M-08	17.5	wackestone	0.25	-3.66		
N-M-09a	20	wackestone	0.19	-3.81		
N-M-09a QCD	20	wackestone	0.1	-3.88		
N-M-10a	22.5	wackestone	0.15	-3.88		
N-M-11a	25	mudstone/wackestone	0.42	-3.76		
N-M-20	27.5	mudstone/wackestone	0.52	-3.95		
N-M-21	30	wackestone	-0.17	-4		
N-M-22	32.5	packstone	0.26	-4.38		
N-M-23	35	wackestone	0.4	-3.62		
N-M-24	37.5	mudstone	0.08	-3.53		
N-M-25	40	mudstone/wackestone	-0.22	-3.65		
N-M-26	42.5	packstone	0.17	-3.83		
N-M-27	45	wackestone/packstone	-0.27	-4.28		
N-M-27 QCD	45	wackestone/packstone	-0.29	-4.24		
N-M-28	47.5	wackestone	0.11	-3.46		
N-M-40	101.5	grainstone	-0.26	-4.91		
N-M-41	102.5	mudstone/packstone	0.24	-3.08		
N-M-42	103.5	packstone	0.19	-3.74		
N-M-43	104.5	wackestone/packstone	0.36	-3.64		
N-M-44	105	wackestone	0.55	-3.09		
N-M-45	105.5	wackestone/packstone	0.48	-3.32		
N-M-46	106	wackestone	0.53	-3.14		
N-M-47	106.5	mudstone/wackestone	0.56	-3.03		
N-M-48	107	packstone	0.06	-4.77		
N-M-48 QCD	107	packstone	0.06	-4.71		
N-M-49	107.5	wackestone/packstone	0.72	-3.04		
N-M-50	108	mudstone/packstone	0.55	-3.04		
N-M-51	108.5	mudstone/packstone	0.38	-4.38		
N-M-52a	108.9	mudstone/wackestone	0.36	-3.27		
N-M-52b	109	mudstone/wackestone	0.95	-3.53		
N-M-53	109.5	packstone	0.74	-3.52		
N-M-54	110	mudstone/packstone	0.12	-3.32		
N-M-55	112	packstone	3.5	-3.66		
N-M-56	112.5	packstone	2.94	-3.72		
N-M-57	113	mudstone/wackestone	2.17	-3.71		
N-M-58	113.5	packstone	2.02	-3.88		
N-M-58 QCD	113.5	packstone	2.04	-3.97		

N-M-59	114	packstone	1.9	-3.6		
N-M-60	115	mudstone/wackestone (stylolitic)	1.92	-3.37		
N-M-61	116	packstone	1.45	-4.67		
N-M-62	117	mudstone/wackestone	1.5	-3.58		
N-M-63	118	wackestone	1.24	-3.64		
N-M-64	119	wackestone	0.98	-3.9	N49° 28.119'	W062° 31.170'
N-M-(01)	47.5	wackestone	0.23	-3.33	N49° 29.114'	W062° 30.626'
N-M-(02)	52.5	packstone	0.32	-3.33		
N-M-(03)	57.5	wackestone	0.14	-3.49		
N-M-(04)	62.5	packstone	-0.73	-3.62		
N-M-(04) QCD	62.5	packstone	-0.53	-3.49		
N-M-(05)	67.5	packstone	-0.07	-3.3		
N-M-(06)	72.5	grainstone	0.76	-4.65		
N-M-(07)	77.5	grainstone	-0.07	-3.73		
N-M-(08)	82.5	grainstone	-0.05	-5.8		
N-M-(08) repeat	82.5	grainstone	0.19	-5.97		
N-M-(09)b	87.5	packstone	0.92	-3.22		
N-M-(10)b	92.5	packstone	0.24	-4.67		
N-M-(11)	97.5	grainstone	0.81	-3.97		

Section 5, Salmon River — GPS Location

This section begins in the upper portion of the Vaureal and ends in the basal Becscie.

Sample #	Height (m)		$\delta^{13}C$ (‰)	$\delta^{18}O$ (‰)	Latitude	Longitude
S-M-01	39.5	packstone	1.79	-4.34		
S-M-02	39.8	packstone	2.54	-3.82		
S-M-03	40.1	mudstone/wackestone	2.84	-2.84		
S-M-04	40.4	mudstone/wackestone	3.56	-3.01		
S-M-05	40.7	mudstone/wackestone	3.38	-2.89		
S-M-05 QCD	40.7	mudstone/wackestone	3.32	-2.84		
S-M-06	41	mudstone/packstone	3.4	-3.74		
S-M-07	41.3	mudstone/wackestone	3.65	-4.17		
S-M-08	41.6	mudstone/wackestone	4.07	-3.4		
S-M-09	41.9	mudstone/packstone	3.95	-4.04		
S-M-10	42.2	mudstone/packstone	4.07	-4.23		
S-M-11	42.5	wackestone/packstone	4.62	-2.75		
S-M-12	42.8	wackestone	3.95	-3.35		
S-M-13	43.1	mudstone/wackestone	3.43	-3.81		
S-M-14	43.4	mudstone/wackestone	3.88	-3.54		
S-M-15	43.7	wackestone	3.9	-3.7		
S-M-15 QCD	43.7	wackestone	3.93	-3.93		
S-M-16	44	mudstone/wackestone	3.95	-3.32		
S-M-17	44.3	mudstone/packstone	4.17	-2.8		
S-M-18	44.6	wackestone	4.25	-3.78		
S-M-19	44.9	mudstone/packstone	3.63	-4.74		
S-M-20	45.2	wackestone	4.35	-2.84		
S-M-21	45.5	mudstone/wackestone	4.22	-4.8		
S-M-22	45.8	wackestone	4.68	-4.23		
S-M-23	46.1	mudstone/packstone	4.19	-3.81		

S-M-24	46.4	mudstone (rugosa/bryozoan)	4.62	-4.28
S-M-25	46.7	mudstone/packstone	4.28	-3.62
S-M-26	39	mudstone/wackestone	0.71	-3.37
S-M-26 QCD	39	mudstone/wackestone	0.73	-3.39
S-M-27	38.5	wackestone/packstone	0.66	-3.29
S-M-28	38	wackestone	0.61	-3.09
S-M-29	37.5	mudstone/wackestone	0.74	-3.14
S-M-30	37	wackestone/packstone	0.74	-4.45
S-M-31	36.5	mudstone	0.68	-3.26
S-M-32	36	mudstone/wackestone	1.19	-3.62
S-M-33	20	wackestone/packstone	1.56	-3.53
S-M-34	20.5	wackestone	1.45	-3.07
S-M-35	21	packstone	1.07	-2.69
S-M-35 QCD	21	packstone	1.12	-2.66
S-M-36	21.5	wackestone	1.02	-2.84
S-M-37	22	wackestone/packstone (stylolitic)	0.82	-2.97
S-M-38	22.5	packstone	0.53	-3.22
S-M-38 repeat	22.5	packstone	0.58	-3.33
S-M-39	23	packstone	-0.27	-2.8
S-M-40	23.5	wackestone/packstone (brachiopod)	0.48	-3.13
S-M-41	38.9	wackestone	0.9	-3.84
S-M-42	38.5	mudstone/packstone	0.66	-3.15
S-M-43	38	wackestone/packstone	0.6	-3.7
S-M-44	37	wackestone/packstone	0.54	-3.23
S-M-45	36	wackestone/packstone (laminated)	0.54	-3.15
S-M-45 QCD	36	wackestone/packstone (laminated)	0.55	-3.18
S-M-46	35.5	wackestone/packstone	0.36	-3.01
S-M-47	35	wackestone/packstone	0.63	-3.03
S-M-48	34.5	mudstone/packstone	0.7	-3.25
S-M-49	34	wackestone/packstone	0.45	-3.06
S-M-50	33.5	packstone/grainstone	0.42	-3.88
S-M-51	33	wackestone/packstone	0.41	-3.33
S-M-52	32.5	wackestone/packstone	-0.02	-3.09
S-M-53	32	wackestone/packstone	0.28	-3
S-M-54	24	grainstone	0.04	-6.72
S-M-54 repeat	24	grainstone	0.37	-7.08
S-M-55	24.5	grainstone	0.76	-3.95
S-M-55 QCD	24.5	grainstone	0.76	-3.93
S-M-56	25	grainstone	0.26	-4.13
S-M-57	25.5	packstone/grainstone	0.26	-4.53
S-M-58	26.5	packstone	0.19	-3.69
S-M-59	39.1	packstone	2.1	-4.36
S-M-60	39.4	packstone	1.83	-4.23
S-M-61	39.7	packstone/grainstone (oncolitic)	2.84	-3.18
S-M-62	40	packstone	3.25	-2.43
S-M-63	13.9	wackestone/packstone	0.6	-3.34
S-M-64	14.5	mudstone/packstone	0.71	-2.97
S-M-65	14.9	mudstone/packstone	0.39	-3.01

S-M-65 QCD	14.9	grainstone	0.44	-3.1		
S-M-66	16.5	packstone/grainstone	0.41	-3.34		
S-M-67	18	grainstone	0.1	-5.39		
S-M-67 repeat	18	grainstone	0.27	-5.81		
S-M-68	18.5	grainstone	0.29	-4.79		
S-M-68 repeat	18.5	grainstone	0.59	-4.97		
S-M-69	19.9	packstone/grainstone	0.62	-3.36		
S-M-70	42.5	mudstone/packstone	2.07	-3.27		
S-M-71	43	wackestone/packstone	2.08	-3.43		
S-M-72	43.5	packstone	2.01	-3.48		
S-M-73	44	wackestone	1.77	-3.72		
S-M-74	44.5	wackestone/packstone	1.78	-3.84		
S-M-75	45	packstone	1.04	-4.94		
S-M-75 QCD	45	packstone	1.15	-4.72		
S-M-76	45.5	grainstone	0.99	-4.9	N49° 24.340'	W062° 21.298'

Section 6, Lousy Cove — GPS Location

This section begins at the base of the Ellis Bay Formation and terminates in the lower portion of the Becscie Formation. The section contains several unconformities.

Sample #	Height (m)		$\delta^{13}C$ (‰)	$\delta^{18}O$ (‰)	Latitude	Longitude
LC-M-01	0	packstone	-0.6	-4.91	N49° 19.968'	W061° 53.198'
LC-M-02	1	packstone (stylolitic)	-0.92	-4.72		
LC-M-03	1.75	packstone	-0.11	-4.94		
LC-M-03 repeat	1.75	packstone	0.05	-5.2		
LC-M-04	3	packstone	-0.2	-4.57		
LC-M-05	4	packstone	-0.07	-4.76		
LC-M-06	5	packstone	0.43	-3.67		
LC-M-07	6	packstone	0.77	-5.67		
LC-M-08a	6.75	wackestone/packstone	0.99	-4.31		
LC-M-08b	7	packstone (brachiopod)	0.25	-3.52		
LC-M-09	8	packstone	0.26	-8.07		
LC-M-09 repeat	8	packstone	0.71	-6.68		
LC-M-10	9	wackestone/packstone	0.82	-4.72		
LC-M-11	10.25	mudstone/packstone	1.73	-3.76		
LC-M-11 QCD	10.25	mudstone/packstone	1.72	-3.71		
LC-M-12	11	mudstone	0.89	-3.68		
LC-M-13	12	mudstone/wackestone	0.64	-6.01		
LC-M-14	13	wackestone/packstone	0.64	-6.09		
LC-M-15	14	mudstone/packstone	-0.43	-3.13		
LC-M-16	15	mudstone/wackestone	-0.42	-4.04		
LC-M-17	16	wackestone/packstone	-0.02	-5.95		
LC-M-17 QCD	16	wackestone/packstone	-0.05	-6.22		
LC-M-18	17	packstone	0.38	-4.39		
LC-M-19	18	wackestone/packstone	0.47	-3.55		
LC-M-20	19	mudstone	0.1	-5.96	N49° 19.121'	W061° 31.201'
LC-M-21	20	mudstone	0.33	-3.18		
LC-M-22	21	mudstone	0.6	-3.16		
LC-M-23	22	mudstone	0.67	-3.32		

LC-M-24	22.75	mudstone/wackestone	0.52	-3.29
PR-01	17.5	packstone	0.62	-4.43
PR-02	19	mudstone	0.33	-4.99
PR-03	19.5	mudstone	0.71	-4.46
PR-04	20.5	mudstone	0.26	-5.67
PR-05	21	mudstone	-0.31	-5.35
PR-06	21.3	mudstone	0.595	-4.56
PR-07	21.6	mudstone	0.8	-3.67
PR-08	22.2	mudstone	0.76	-3.4
PR-09	22.5	wackestone	0.87	-3.33
PR-10	23	wackestone	0.46	-3.16
PR-11	23.1	wackestone	1.06	-3.53
PR-12	23.2	grainstone	3.52	-4.46
PR-13	23.3	grainstone	2.98	-4.34
PR-14	23.4	grainstone	4.37	-3.47
PR-15	23.5	grainstone	3.59	-5.21
PR-16	23.6	grainstone	2.99	-3.64
PR-17	23.7	grainstone	3.45	-4.34
PR-18	23.8	grainstone	3.04	-3.53
PR-19	24.2	grainstone	3.19	-3.38
PR-20	24.5	grainstone	2.82	-4.58
PR-21	25.2	packstone	2.48	-3.53
PR-22	25.5	packstone	2.13	-4.93
PR-23	26	packstone	2.5	-3.58
PR-24	26.7	packstone	2.37	-3.93
PR-25	28	packstone	2.03	-4.04
PR-26	28.8	packstone	2.2	-3.8
PR-27	29.2	packstone	1.56	-4.69
PR-28	30.2	packstone	1.17	-4.27
PR-29	31.2	packstone	1.0	-4.37

Appendix C. Isotopic analysis of partially dolomitized samples

The following samples were suspected to be partially dolomitized. They were analyzed twice using two different methods: the online method where $CaCO_3$ powder from the samples was reacted with H_3PO_4 in exetainers and placed directly into a Thermo Finnigan Delta XP mass spectrometer, and the offline method where the mixture reacted at 25°C for a three hour period before being placed into the mass spectrometer.

Sample #	$\delta^{13}C$ (‰)			$\delta^{18}O$ (‰)		
	Offline	Online	Difference	Offline	Online	Difference
E-M-18 dol	2.03	1.88	0.15	-5.04	-3.41	-1.63
E-M-19 cc	2.28	2.48	-0.20	-5.40	-3.97	-1.43
E-M-20 cc	1.56	2.14	-0.58	-5.40	-3.40	-2.00
E-M-22 cc	2.78	2.82	-0.04	-4.56	-2.95	-1.61
E-M-31 cc	0.12	0.61	-0.49	-5.80	-5.13	-0.67
Mean :			-0.23			-1.47
Variance :			0.09			0.24
St. Error :			0.14			0.22
T-value :			1.70			6.67
P-value :			0.16			0.00

In this analysis it was found that the $\delta^{13}C$ measurements of the dolomitic samples using the offline method were not significantly different than the measurements made online with the same samples. However, the $\delta^{18}O$ measurements of the dolomitic samples using the offline method were consistently lower than the measurements made online. The plots on the next page illustrate the measured values of $\delta^{13}C$ and $\delta^{18}O$ for the online and offline methods. The second plot displays the difference in values obtained from the online and offline methods for each sample.

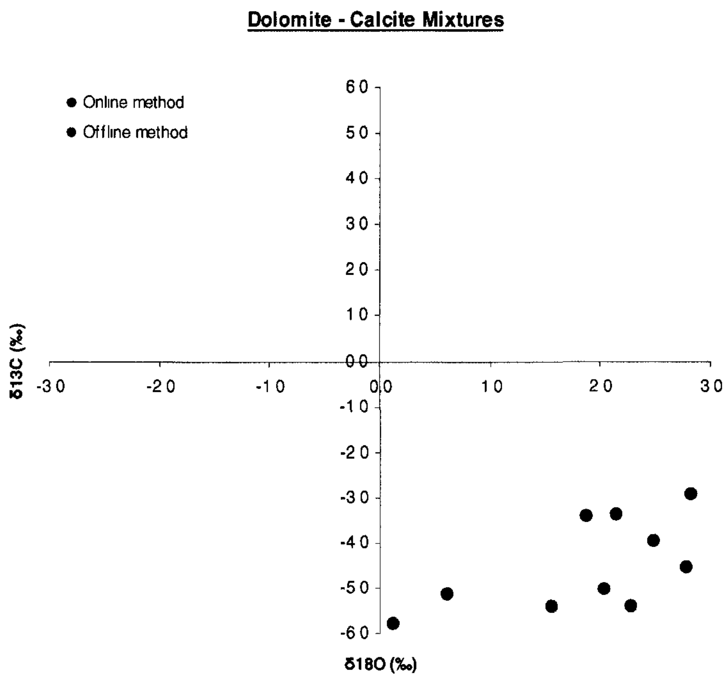
Dolomite - Calcite Mixtures
Online method
Offline method
δ13C (‰)
δ18O (‰)

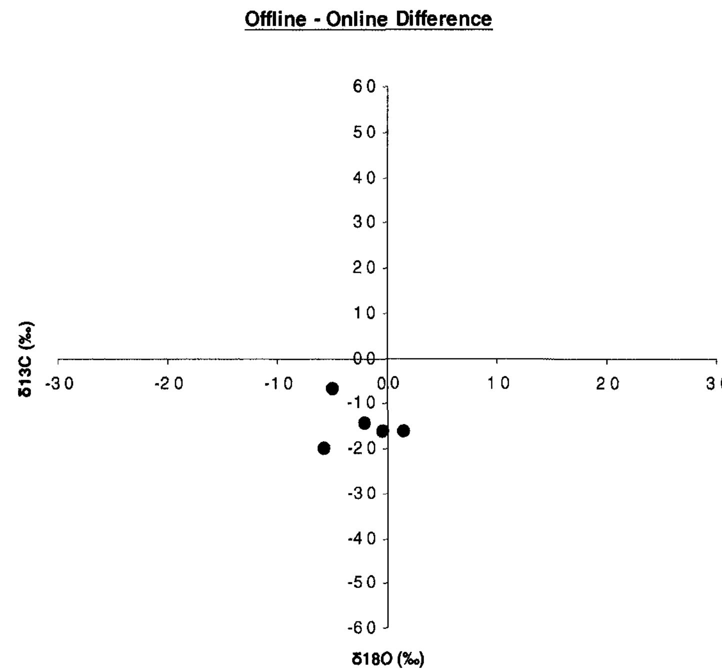
Offline - Online Difference
δ13C (‰)
δ18O (‰)

Appendix D. Isotopic analysis of paired micrite and brachiopod shells

$CaCO_3$ powder was collected from the following samples in different locations to compare the $\delta^{13}C$ and $\delta^{18}O$ values of micrite and brachiopod shells to test the reliability of micrite as a primary isotopic signature.

Sample #	$\delta^{13}C$ (‰)				Brach. - Mic.
	Micrite	Brachiopod	Rugosa	Cement	Difference
B-B-01	-0.26	-0.46			-0.20
V-B-01	-0.22	0.29			0.51
V-B-02	0.47	1.34	0.58		0.87
E-B-01	1.06	1.30			0.24
E-B-02a	0.80	1.54		0.94	0.74
E-B-02b	0.80	1.58			0.78
E-B-03	0.68	0.46			-0.22
Mean :					0.39
Variance :					0.21
St. Error :					0.17
T-value :					2.24
P-value :					0.07

Sample #	$\delta^{18}O$ (‰)				Brach. - Mic.
	Micrite	Brachiopod	Rugosa	Cement	Difference
B-B-01	-3.15	-2.61			0.54
V-B-01	-2.29	-2.19			0.10
V-B-02	-2.70	-1.76	-2.37		0.94
E-B-01	-2.13	-2.21		-4.11	-0.08
E-B-02a	-2.11	-2.29			-0.18
E-B-02b	-3.60	-1.99			1.61
E-B-03	-3.52	-1.42			2.10
Mean :					0.72
Variance :					0.77
St. Error :					0.33
T-value :					2.17
P-value :					0.07

In this analysis it was found that the $\delta^{13}C$ measurements of the micrite were not significantly different from the values obtained for brachiopod shells (p = 6.6 %). The $\delta^{18}O$ measurements of the micrite were also found to be not significantly different from the values obtained for brachiopod shells (p = 7.3 %). The following plots illustrate the measured values of $\delta^{13}C$ and $\delta^{18}O$ for the brachiopod and micrite samples. The second plot displays the difference in values obtained from the brachiopod and the micrite of the same sample.

Brachiopods and Micrites

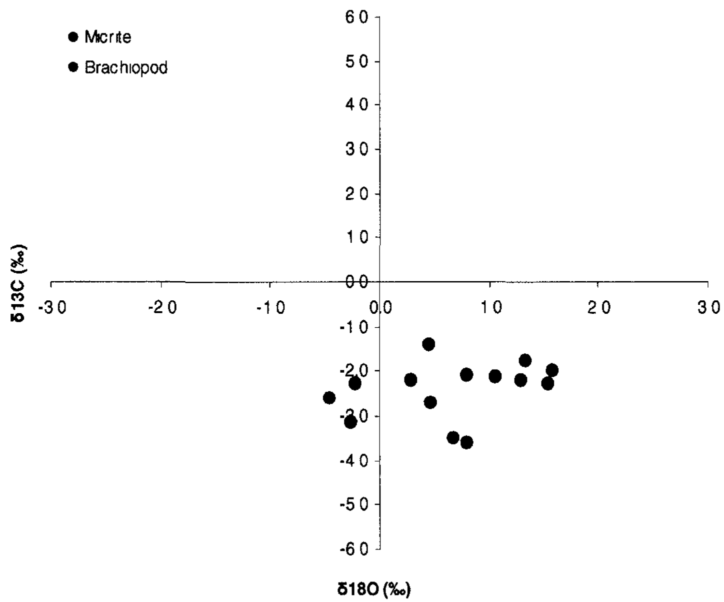

Brachiopod - Micrite Difference